学位論文

# Cosmological constraints on short-wavelength primordial perturbations

# （短波長原始ゆらぎに対する宇宙論的制限）

平成 27 年 12 月博士（理学）申請

東京大学大学院理学系研究科
物理学専攻

中間 智弘

# Abstract

Primordial perturbations of a huge range of wavelengths are generated in the early universe, and largest wavelengths of these are indirectly observed as anisotropy of the intensity of photons, or they provide the seeds of the structures of the universe we see today. The nature of primordial perturbations on large wavelengths has been well determined, while that of primordial perturbations of shorter wavelengths is less understood. Primordial perturbations of shorter wavelength cause a wealth of phenomenology, through which their properties can be constrained.

For instance, if some region strongly deviates from other places, that region collapses to a black hole in the early universe. That is, black holes could have been formed even in the early universe, well before structures such as stars are formed. So far there is no conclusive observational evidence for the substantial formation of such black holes in the past, which fact itself provides valuable information about the nature of primordial perturbations, and hence about mechanisms of generation of primordial perturbations.

Another example of phenomenology related to primordial perturbations of short wavelengths is dissipation of them due to diffusion processes, and this diffusion leads to energy release into the universe, which was originally stored in sound waves. This energy release causes the slight increase in the global temperature of the universe, or distortions in the energy spectrum of photons in the universe.

In this dissertation, investigation of primordial perturbations of short wavelengths is discussed through these kinds of phenomenology.

# Acknowledgements

First and foremost I would like to extend my sincerest gratitude and appreciation to my supervisor, professor Jun'ichi Yokoyama, for his continuous support and encouragement in various ways. To give just one example, he gave me an opportunity to be involved in my first, international research project, which was to lay the foundation of this dissertation, and also to travel abroad for the collaboration a couple of times as a master student. These were good experiences in many ways in retrospect. I also greatly appreciate Dr. Teruaki Suyama for helpful discussions, from which I have learned a great deal. The collaborations with him have always been fruitful and indeed they constitute a large portion of this dissertation. I would like to thank collaborators, Drs. Alexander Polnarev, Tomohiro Harada, Kazunori Kohri, Chul-Moon Yoo and Yasutaka Koga for helpful discussions. I have learned a lot from the collaborations with them as well. In addition, I am grateful to all the members of Research Center for the Early Universe (RESCEU) and the University of Tokyo Theoretical Astrophysics (UTAP) for many useful discussions and friendships. A special thanks is also extended to the administrative staff of RESCEU, Sayuri Nagano and Mieko Minamisawa, for providing comfortable research environments. I also thank the Japan Society for the Promotion of Science (JSPS) for the research fellowship I received for the last three years of my Ph.D. course. Finally, I would like to express my sincere gratitude to my family for continuous support in every way.

# Contents

# Chapter 1

# Introduction

Primordial perturbations of a huge range of wavelengths are generated quantum mechanically in the early universe (see [1–4] for earliest works of generation of irregularities in the framework of primordial inflation). Largest wavelengths of them are observed as anisotropy of the cosmic microwave background (CMB), having been observed by satellite missions COBE [5], WMAP [6] and Planck [7], or they provide the seeds of the large-scale structures (LSSs) of the universe we see today. The nature of primordial perturbations on large wavelengths has been well determined (see [8] in 2015 for the latest results obtained by the Planck collaboration), while that of primordial perturbations of shorter wavelengths is less understood. Though simplest models of inflation predict almost scale-invariant power spectrum (see e.g. [1–4, 9–11]), different models of the early universe predict different properties of short-wavelength perturbations, e.g. larger power on small scales (see e.g. [12] and references therein), and so investigation of primordial power on small scales can also provide helpful information about the early universe, which is complementary to what can be leaned from observations of CMB or LSS.

Primordial perturbations of shorter wavelengths cause a wealth of phenomenology, through which their properties can be constrained. For instance, if some region strongly deviates from other places in the universe, that region collapses to a black hole (called a primordial black hole, PBH) [13–15]. That is, black holes could have been generated even in the early universe, well before structures such as stars are formed. So far there is no conclusive observational evidence for substantial formation of such black holes in the past (see [12] for a holistic summary of observational upper bounds on PBHs), which fact itself provides valuable information about the nature of primordial perturbations (see e.g. [16, 17]), and hence about mechanisms of generation of primordial perturbations.

Another example of phenomenology related to primordial perturbations of short wavelengths is dissipation of them due to diffusion processes (diffusion or Silk damping [18,19]), and this diffusion leads to energy release into the universe, which was originally stored in sound waves (see one of the earliest works [20]). This energy release causes the slight increase in the global temperature of the universe, or deviations of the energy spectrum of photons in the universe from a Planck spectrum (called CMB distortions), depending on when the dissipation happens, namely, depending on comoving scales of perturbations. See a recent review [21] and references therein.

If primordial power on small scales is larger than the prediction of the almost scale-invariant fluctuations, compact dark matter (hereafter abbreviated as DM) halos may be formed in the early universe ($z \sim 1000$) [22]. Annihilation of DM may be highly efficient in

these mini-halos, and hence they may be detected on earth. In other words, observations of gamma-rays or neutrinos can be used to constrain these mini-halos, which can then be translated into constraints on primordial power on small scales. See [23] for a discussion about constraints on primordial power obtained by gamma-rays from these mini-halos.

In this dissertation, investigation of primordial perturbations of short wavelengths is discussed through these kinds of phenomenology. This dissertation is organized as follows.

Chapter 2 is dedicated to brief reviews of relevant topics; PBHs, CMB spectral distortion and compact DM mini-halos are reviewed.

Supermassive black holes (SMBHs) of $10^9 \sim 10^{10} M_\odot$ have been observed at high redshifts [24–37], and there has been no established explanation about how such gigantic black holes could have been formed by such early times. In Chapter 3, the possibility of PBHs as the seeds of these SMBHs observed at high redshifts is discussed. If primordial perturbations follow a Gaussian distribution or one similar to it, PBHs larger than $10^4 \sim 10^5 M_\odot$ are excluded due to constraints on CMB spectral distortion [38,39]. This is because in order for the probability of PBH formation being sufficiently large to explain SMBHs, the amplitude of primordial perturbations of wavelengths corresponding to the scales of the seeds of SMBHs has to be very large, which causes CMB spectral distortion to a level that is inconsistent with observational upper bounds on CMB spectral distortion obtained by COBE/FIRAS. We discuss models which predict highly non-Gaussian perturbations to evade CMB distortion constraints, and in these models PBHs can be produced whose mass is as large as necessary to account for the observed SMBHs at high redshifts and whose abundance is also adjustable to match observations. This Chapter is based on a work in preparation [40] and on a part of [39].

In Chapter 4, *acoustic reheating* is discussed, which is a slight increase in the global temperature of the universe, resulting from dissipation of primordial perturbations after Big Bang Nucleosynthesis (BBN). This acoustic reheating causes a slight decrease in the baryon-to-photon ratio $\eta$. The values of $\eta$ at BBN and the photon decoupling have been independently determined from observations of the abundance of the light elements in the universe [41] and CMB anisotropy [42], which means if $\eta$ decreases too much, it contradicts with these observations. From this consideration, upper bounds on primordial perturbations are obtained which dissipate after BBN but before the moment after which dissipation of perturbations causes CMB spectral distortion, noting perturbations of wavelengths which cause substantial CMB distortion have already been tightly constrained. This Chapter is based on [43].

Cosmological perturbations can be decomposed into scalar, vector, and tensor components, and Chapters 2-4 are devoted to discussions of investigation of short-wavelength primordial *scalar* perturbations. In Chapter 5, investigation of primordial short-wavelength *tensor* perturbations is discussed. It is known that scalar, vector and tensor perturbations evolve independently in linear theory, but they are coupled at the second-order level. For instance, scalar perturbations are generated from second-order tensor perturbations. If the amplitude of these induced scalar perturbations is extremely large, these perturbations collapse to form PBHs. Since there has been no conclusive evidence for the existence of PBHs, overproduction of PBHs is forbidden to be consistent with observations. This consideration leads to upper bounds on induced scalar perturbations, which can be translated into upper bounds on the amplitude of primordial *tensor* perturbations on small scales. This Chapter is based on [44] and a work in preparation [45].

# Chapter 2

# Probing primordial power on small-scales: review

In this Chapter an overview is provided about the topic of investigation of primordial power on small scales. As is explained in §2.1, primordial perturbations of various wavelengths are generated in the early universe. Those of large wavelengths ($\mathcal{O}$(Mpc) − $\mathcal{O}$(Gpc)) have been well investigated by observations of CMB and LSS, but those of shorter wavelengths are less understood. Since different models of the early universe predict different properties of primordial perturbations of various wavelengths, investigation of primordial power on small scales also provides useful information. There are several methods to be used for this, which include primordial black holes (§2.2), CMB spectral distortion (§2.3) and compact DM mini-halos (§2.4).

## 2.1 Primordial perturbations of various wavelengths generated in the early universe

The theory of inflation provides solutions to the horizon problem, flatness problem and unwanted relics problem, and it was proposed by Starobinsky in 1979 [46] and in 1980 [47], by Sato (1981) [48], and by Guth (1981) [49]. This theory also provides a mechanism of generation of primordial perturbations through quantum fluctuation, which serve as the seeds of the structures in the universe we observe today. During inflation, perturbations[†1] are generated quantum mechanically at each moment on scales less than the Hubble radius. Then, the wavelength of these perturbations is stretched exponentially outside the Hubble radius due to the exponential expansion of the universe, when these perturbations are thought to "classicalize" (see e.g. [50] and references therein). This process of generation inside the Hubble radius and subsequent stretching happen continuously during inflation, and so a huge range of wavelengths of perturbations are generated. Primordial perturbations generated during inflation are quite often represented in terms of

[†1] As is mentioned in the Introduction, perturbations to the metric can be decomposed into scalar, vector and tensor perturbations. In the early universe, all of these are generated due to quantum fluctuation, and what matters to the structures of the universe is basically scalar perturbation. This dissertation discusses investigation of short-wavelength primordial scalar perturbations in Chapters 2,3,4 and tensor perturbations in Chapter 5.

the so-called "curvature perturbation", and this quantity is conserved on super-horizon scales (see e.g. [51] and references therein). Then this curvature perturbation is converted into perturbations of various components of the universe, e.g. perturbations in radiation energy density or perturbations in DM energy density. After the exponential expansion phase of inflation, the universe enters into decelerated expansion phases, during which perturbations reenter the horizon. That is, the physical scales of perturbations become once more smaller than the Hubble radius, and the longer the wavelength is, the later this reentry happens. After the reentry, perturbations of different components with different wavelengths and amplitudes evolve differently, leading to a wealth of phenomenology, a few of which are discussed in this dissertation.

The largest scale which can be observed today roughly corresponds to the current Hubble or horizon scale, which is $\sim$Gpc[†2], and perturbations of these scales reenter the horizon relatively recently, and so they maintain primordial nature of perturbations more than shorter-wavelength perturbations. Perturbations of these scales are observed as the anisotropy of CMB (see e.g. [8] by the Planck collaboration (2015)), which has revealed that the amplitude of anisotropy is $\mathcal{O}(10^{-5})$, which is comparable to the amplitude of the curvature perturbation generated during inflation on these scales. Primordial perturbations in principle exist on all the scales below this scale ($\sim$Gpc)[†3].

Simplest inflationary models predict almost-scale-invariant power spectrum [1–4,9–11], i.e. the amplitude of the primordial curvature perturbation (in modern parlance) is almost the same on any scales, which was hypothesized by Harrison (1970) [54], by Peebles (1970) [55] and by Zel'dovich (1972) [56] (Harrison-Zel'dovich-Peebles spectrum). As mentioned above, this has been confirmed on largest observable scales (Mpc-Gpc) by observations of CMB anisotropy or LSSs of the universe, and the amplitude of primordial perturbations on these large scales has been inferred to be $\sim 10^{-5}$. However, the power spectrum of primordial perturbations on smaller scales is less understood, and we only

[†2]When scales of perturbations are referred to, they indicate comoving length scales, or current length scales. That is, the physical scale at time $t$, $l_{\rm phys}(t)$, is related to its comoving scale $l_{\rm com}$ by $l_{\rm phys}(t)a(t_0)/a(t) = l_{\rm com}$, where $a$ is the scale factor and $t_0$ is the age of the universe.

[†3]Sometimes the Hubble radius at the end of inflation, the comoving scale of which is $\sim$ Gpc $\times$ e$^{-60}$ $\sim$m if we assume the number of e-folds during inflation is sixty, is referred to as the shortest scale, below which perturbations are assumed to be absent. This may be because perturbations below this scale have never exited the Hubble radius, and so the classical nature of these perturbations is uncertain. Strictly speaking however, perturbations below this scale would also have been generated quantum mechanically during inflation. Note that the most plausible ways to probe extremely short scales of primordial perturbations are gravitational waves (GWs) and PBHs, as will be explained in the text. See [52] about PBH formation due to collapse of perturbations below this "shortest scale". The frequency range of GWs these perturbations cause (at the level of second-order perturbations) would be extremely high, and so probing these perturbations would be challenging (see also [53] for a discussion about possible implications of these extremely short-scale perturbations). With these in mind, in this dissertation the above-mentioned scale ($\sim$m) is referred to as the "shortest scale", and we focus on scales larger than this. There is another comment about small-scale perturbations. Though we currently observe perturbations on meter or smaller scales (e.g. human body), these do not directly reflect *primordial* perturbations of the same scales. Rather, these result from power transfer from large to small scale perturbations, which happens relatively recently when larger-scale perturbations become nonlinear to form the structures of the universe.

have relatively weak constraints on them. This situation is well illustrated in Fig.6 of Bringmann, Scott and Akrami (2012) [23]. The almost-scale-invariant power spectrum may continue all the way down to smallest scales ($\sim$ Gpc $\times$ e$^{-60}$ $\sim$ m, if the number of e-folds during inflation is assumed to be sixty), as is predicted by simplest models, but this may be a very strong extrapolation noting the almost-scale-invariant power spectrum has been confirmed only on largest scales mentioned above. The primordial power may be smaller or larger than the prediction of the almost-scale-invariant power spectrum.

So far, a number of inflationary models have been proposed, which are consistent with large-scale observations mentioned above, and some of these predict small-scale power larger than the prediction of the almost-scale-invariant power spectrum, with the fractional amplitude of $\mathcal{O}(10^{-5})$. One of the simplest models of inflation which can potentially lead to large power on small scales was discussed by Ivanov, Naselsky and Novikov (1994) [57]. They consider a phenomenological single inflation model with the inflaton potential having a relatively narrow plateau region somewhere in the middle. The power spectrum of scalar perturbations of this model can coincide with the standard almost scale-invariant power spectrum on large scales, but the power spectrum is enhanced on some small scale. The position of this enhancement is roughly determined by the position of the plateau region and the structures such as height and width are determined by the width of the plateau region in the inflaton potential. Another simple single-inflation model (chaotic new inflation) was analyzed by Yokoyama in 1998 [58], and by Saito, Yokoyama and Nagata (2008) [59]. They used the Coleman-Weinberg potential [60], which has two minima. If the initial value of the inflaton is large, the chaotic inflation occurs first, and, depending on the parameter choice, the field rolls up towards the origin through one of the minima, moves slowly there, and the new inflation begins towards one of the minima. At the end of the chaotic inflation, the slow-roll conditions are violated, and consequently the curvature perturbation is enhanced, at the scale corresponding to that moment. About other inflationary models predicting large power on small scales, see also [38, 61–74]. See also a recent review by Green (2014) [75] and references therein.

Since different models predict different properties of primordial perturbations on small scales, probing them is important to narrow down models of inflation. Completely determining the properties of primordial perturbations on small scales would be probably hopeless, but the question of to what extent mankind can probe primordial power on small scales itself would be an interesting question. There are several methods to probe small-scale primordial power, which include PBHs, CMB spectral distortion and compact DM mini-halos. In the next sections we will take a brief look at these topics.

## 2.2 Primordial black holes

### 2.2.1 Overview

Black holes (BHs) are thought to form at the end of collapse of stars, and the typical mass of these astrophysical BHs is the solar mass $\sim M_\odot$. However, BHs could have been also formed in the early universe, well before the standard structure formation of the universe has even begun, and these BHs are called primordial black holes (PBHs). PBHs were first discussed by Zel'dovich and Novikov in 1966 [13], by Hawing in 1970 [14], and by Carr and Hawking in 1974 [15]. There are several mechanisms which cause PBH

formation (see [76] and references therein), but the most conceivable mechanism would be direct collapse of large amplitude perturbations during radiation domination upon horizon reentry, which we will focus on in this dissertation. Let us consider a region on a super-horizon scale, which strongly deviates form the background universe by order unity, namely, the curvature perturbation smoothed over this region is order unity. This region evolves as a closed universe, and initially, this region expands, just as other parts of the universe do, but the expansion of this region becomes slower and slower than other parts. As time goes by, this region stops expansion at around the moment of the horizon crossing of this region, and begins to contract, and soon afterwards, this regions falls into its own Schwarzschild radius, namely, a PBH is formed. Since the formation of the BH horizon takes place shortly after the horizon crossing, the mass of PBHs can be roughly estimated by the horizon mass, or the total energy contained inside the horizon at the moment of the horizon crossing of this region:

$$M_{\rm PBH} \sim \rho_{\rm rad} \frac{4\pi}{3} \left(\frac{c}{H}\right)^3 \sim \frac{c^3 t}{G} \sim 2 \times 10^5 M_\odot \left(\frac{t}{1{\rm sec}}\right). \tag{2.1}$$

That is, the mass of PBHs can in principle take various values ("$10^{-5}g$ upwards" [14]), depending on when they are formed. Subsequent accretion of radiation after the formation before matter domination is negligible due to the rapid expansion and resultant dilution of radiation, as is shown by both analytical and numerical studies cited in the following subsections. Equivalently, the mass of PBHs is determined by the comoving wavenumber $k$ of perturbations collapsing to PBHs. Defining the horizon crossing by $k = aH$ and using $H = \sqrt{\Omega_r} H_0 a^{-2}$ to eliminate the scale factor, the above relation (2.1) can be rewritten as

$$M_{\rm PBH} \sim 2 \times 10^{13} M_\odot \left(\frac{k}{1{\rm Mpc}^{-1}}\right)^{-2}. \tag{2.2}$$

The formation of PBHs numerically simulated is reviewed in the Appendix A.

### 2.2.2 Analytical arguments of PBH formation condition

As previously mentioned, PBHs are formed when perturbation amplitude is order unity, which was noted in the earliest works mentioned above, but in order to calculate the probability of PBH formation more precisely, the condition for PBH formation needs to be determined more precisely. This endeavor was initiated by Carr in 1975 [77], in which the threshold of PBH formation in terms of the amplitude of the radiation density perturbation at the moment of the horizon crossing (in the uniform Hubble slicing) $\delta_r \simeq 1/3$ was obtained, which has long been used quite often in the literature when calculating PBH formation probability. This condition was obtained using a simplified model of PBH formation, and the Jeans analysis, in which the above condition is obtained by requiring the radius of the overdensity at the moment of the maximum expansion is larger than the Jeans scale, over which sound waves propagate over cosmological time scale. This indicates that the uncertainty of order unity is expected in the above threshold[†4].

Recently, Harada, Yoo and Kohri (2013) [80] has refined the arguments in [77], to obtain more precise PBH formation criteria, which are consistent with the threshold

[†4]To the knowledge of the author, spherical symmetry is assumed in all the works on PBH formation process. This may be partially justified by Bardeen, Bond, Kaiser and Szalay (1986)

values obtained in numerical simulations by Polnarev and Musco (2006) [81]. They adopt a three-zone model, in which the central overdense region is described by a closed Friedmann universe, and this overdense region is connected to an underdense layer, which is then matched to a surrounding flat Friedmann universe. Then they adopt the condition that

> "if and only if the sound wave crosses from the center to the surface outwardly or from the surface to the center inwardly before the maximum expansion, the pressure gradient force prevents the overdense region from becoming a black hole."

also noting that this

> "requirement is naturally equivalent to the formation criterion that the sound crossing time over the radius be longer than the free fall time from the maximum expansion to complete collapse."

### 2.2.3 Numerical simulations of PBH formation process

Here we review numerical works on PBH formation. See also the Appendix A, where PBH formation process is reviewed, based on [82, 83]. The process of PBH formation and its condition have been investigated in a number of subsequent numerical works, the earliest of which is probably Nadezhin et.al. (1978) [84]. They adopted a formulation similar to the one developed by Misner and Sharp (1964) [85] (hereafter MS formulation), and they used a time coordinate which is synchronized with the proper time of an observer in an FRW universe at infinity. In their formulation the BH singularity appears at the center after the BH horizon is formed, and so subsequent accretion of radiation cannot be followed to determine the eventual mass of PBHs.

Niemeyer and Jedamzik (1999) [86] circumvented this problem by combining the MS formulation and the one by Hernandez and Misner (1966) [87] (hereafter MSHM formulation), which was first developed by Baumgarte, Shapiro and Teukolsky [88] to simulate supernova collapse. See the Appendix A for more details.

One of the important and interesting aspects of PBH formation, investigated by Niemeyer and Jedamzik, is a scaling relation of the mass of PBHs near the threshold: $M_{\rm PBH} = KM_{\rm hor}(\delta - \delta_c)^\gamma$, where $K$ is a numerical coefficient of order unity, $M_{\rm hor}$ is the horizon mass at the moment of the horizon crossing of the perturbation collapsing to a PBH, $\delta$ is a parameter characterizing the amplitude of initial perturbation, for which the density perturbation is often used, $\delta_c$ is its threshold, above which the perturbation collapses to a PBH, and $\gamma$ is a positive non-dimensional parameter. Niemeyer and Jedamzik

[78]. First note that only statistically rare high-$\sigma$ peaks are relevant to PBH formation since the probability of PBH formation has to be extremely rare to be consistent with observations, as will be discussed later in more detail. In [78] these high-$\sigma$ peaks are shown to tend to be more spherically symmetric, at least under the assumption of Gaussian perturbations (see also Adler (1981) [79]). Also, PBHs are formed shortly after the horizon crossing, since the Schwarzschild radius of an overdensity is comparable to the Hubble radius, and so there may not be sufficient time for non-sphericity to play an important role in PBH formation, though detailed analysis on this matter would be merited and awaited.

were the first to investigate this scaling relation in the context of PBHs in [86][†5].

In their work, the initial conditions are provided at around the moment of the horizon crossing, and so Shibata and Sasaki (1999) [92] noted that the initial conditions in [86] are "inevitably contaminated by unrealistic decaying mode perturbations", and their criterion of PBH formation "cannot be directly related to the initial condition at the end of inflation". On the other hand, Shibata and Sasaki provide initial conditions when perturbations are on super-horizon scales, with the help of the gradient expansion approach, which is basically an expansion over the ratio of the Hubble radius to the length scale of perturbation, which is smaller than unity when perturbations are on super-horizon scales. They provide initial conditions adopting a class of initial perturbation profiles and obtain PBH formation condition for that class. They use the constant-mean-curvature slicing, which is expected to help avoid singularity without the need to switch slicings in the middle of numerical integration. They present a formulation which can be applied to general 3D cases, but they apply it to spherical symmetric cases.

Hawke and Stewart (2002) [93] report that the scaling relation of the mass of PBHs levels off at around $M_{\rm PBH} \sim 10^{-4} M_{\rm hor}$, which indicates that there exists a minimum mass of PBHs for each scale of primordial perturbation. But it would be worthwhile to mention that they provide initial conditions on sub-horizon scales.

Musco, Miller and Rezzolla (2005) [94] calculate the time evolution of initially super-horizon, growing nonlinear perturbations, and obtain threshold values consistent with those found by Shibata and Sasaki. Polnarev and Musco (2007) [81] develop a formalism to provide initial conditions for simulation of PBH formation, using what they call the quasi homogeneous solution. They introduce the squared ratio $\epsilon$ of the Hubble radius to the scale of perturbation, which is small when the perturbation is on super-horizon scales. They also introduce a curvature profile $K(r)$ describing the initial perturbation profile in the limit $\epsilon \to 0$. This function can be related to the curvature perturbation. They then expand solutions in terms of $\epsilon$, and obtained first order solution written in terms of $K(r)$. That is, the time evolution of nonlinear perturbations can be partially followed from $\epsilon \to 0$ to some finite $\epsilon$, which is sufficiently small so that the expansion is valid. This expansion looks similar to the gradient expansion mentioned above, and indeed the spirit is the same. They calculate the time evolution of initial curvature profiles $K(r)$, using their quasi-homogenious solution to solve for the time evolution while perturbations are on super-horizon scales, and then using numerical simulation whose initial conditions are prepared using the quasi-homogeneous solution at some moment in time when the perturbation is on a super-horizon scale. They consider two classes of profiles $K(r)$, one is Gaussian, and another class which includes those which are closer to a top-hat. They find that the PBH formation criterion in terms of the density perturbation

[†5]This scaling relation of the mass of PBHs is important also to calculate the mass spectrum of PBHs. Since this scaling relation means that the mass of PBHs can be smaller than the horizon mass, and as a result the mass spectrum becomes in principle broader than the assumption of the monochromatic mass function at the horizon mass. This issue is investigated by Niemeyer and Jedamzik (1997) [89] and by Yokoyama (1998) [90]. They find that a mass spectrum still has a sharp peak at around the horizon mass, which is probably because the scaling relation matters only when $\delta$ is extremely close to $\delta_c$ (see e.g. [91]), and the probability of such realizations is relatively small, even though the probability density function (PDF) of $\delta$ is usually monotonically decreasing.

smoothed over the overdense region and evaluated at the moment of the horizon crossing depends on the slope of $K(r)$. That is, the PBH formation condition can not be fully described by a single parameter describing the amplitude of the primordial perturbation, and at least more than one parameters are required, to describe the PBH formation condition more precisely. In Musco, Miller and Polnarev (2008) [95] and Musco and Miller (2013) [91] the critical nature of PBH formation is investigated much in detail, using the quasi homogenious solution describing growing perturbations. They do not find the level-off of the scaling relation of the mass of PBHs, reported by Hawke and Stewart, at least up to $(\delta - \delta_c, M_{\rm PBH}) \sim (10^{-10}, 10^{-3} M_{\rm hor})$.

The author and collaborators have also contributed to this endeavor of investigation of PBH formation process in [82,83,96,97]. Though these do not constitute a part of this dissertation, it would be worthwhile to take a brief look at these.

First, in [96], we generalized the quasi-homogeneous solution by [81] to include higher order corrections in terms of the expansion parameter $\epsilon$. We formally expand the solutions and the equations in terms of $\epsilon$, to obtain a system of recursive relations. By solving these, one can obtain arbitrarily higher order solutions in terms of $\epsilon$, which are expressed in terms of the curvature profile $K(r)$. The inclusion of higher-order corrections enables us to calculate the time evolution of initial perturbations, specified in $\epsilon \to 0$ limit in terms of $K(r)$, up to a moment which is much closer to the moment of the horizon crossing ($\epsilon = 1$) of the perturbation under consideration. In [96], up to seventh order solutions are obtained, to be contrasted with the first order solution presented in [81].

Since [81] has shown the importance of initial perturbations profiles in determining PBH formation, and also various kinds of profiles of perturbations must have been generated in the early universe, it is desirable to investigate PBH formation condition which is applicable to as many types of profiles as possible. Hence, armed with the higher order solutions mentioned above, in Nakama, Harada, Polnarev and Yokoyama [82], we numerically solve the evolution of spherically symmetric, strongly perturbed configurations to clarify the criteria of PBH formation using an extremely wide class of curvature profiles characterized by as many as five parameters, (in contrast to only two parameters used in previous papers) which specify the curvature profiles not only at the central region but also at the outer boundary of configurations. This includes initial perturbations profiles investigated in [81, 92], and also includes those which have not been investigated. It is shown that formation or non-formation of PBHs is determined essentially by only two master parameters one of which can be presented as an integral of curvature over initial configurations and the other is presented in terms of the position of the boundary and the edge of the core.

It turns out that the function introduced in [82] enables us to investigate a phenomenon we call the double formation of PBHs, investigated in Nakama (2014) [83]. Suppose there exists a highly perturbed region which will collapse to form a PBH after horizon crossing, and also that this region is superposed on a much larger region, which also collapses as it enters the horizon later. Then, the collapse of the central smaller region at the time of the horizon crossing should be followed by another collapse of the larger-scale perturbation at the time of the horizon crossing of this larger-scale perturbation. The smaller PBH, formed earlier, is involved in the second collapse leading to a larger PBH as the final state. It is expected that the first collapse is not significantly affected by the presence of the larger perturbation since it is still outside the horizon at the time of the crossing of the

smaller perturbation[†6]. [83] was aimed at reporting a first direct numerical confirmation of this phenomenon of double PBH formation[†7].

In the double formation of PBHs, from the smaller PBH perspective, one is simply swallowed by the larger PBH. But from the point of view of the larger PBH, the presence of the smaller-scale perturbation leading to the smaller PBH corresponds to the existence of a high-frequency mode (hereafter a HF mode), whose wavelength is much shorter than the perturbed region under consideration. In numerical simulations of the formation of PBHs, the presence of HF modes is not usually taken into account, implicitly assumed to be smoothed out. In reality, HF modes should also exist unless PBHs result from a spike in the primordial power spectrum with extremely small width, and thus affect the formation of PBHs to some extent so investigating this issue is also important to fully understand the dynamics of the PBH formation. This has also been numerically investigated for the first time in [83] and we find that HF-modes facilitate the formation of PBHs. These issues are briefly reviewed in the Appendix A, based on [83].

In Harada, Yoo, Nakama and Koga [97], the gradient expansion approach and quasi homogeneous solution were manifestly shown to be equivalent. Also, the relationship between the results obtained in the formulation by Shibata and Sasaki and by the MSHM formulation is obtained.

### 2.2.4 Abundance of PBHs generated by collapse of primordial perturbations

So far we have argued that PBHs form if the amplitude of primordial perturbations becomes order unity somewhere in the universe. Then, the question one might ask is, to what extent that was possible in the early universe? To address this question one needs statistical properties of primordial perturbations. Suppose that the almost-scale-invariant power spectrum is valid up to the shortest scales, and that the number of e-folds during

[†6]Related to this issue, in [98], it is argued that one should focus on the density contrast on comoving slices to correctly calculate PBH abundance, considering the existence of super-horizon modes of the curvature perturbation.

[†7]This phenomenon is an analogue of situations where a dark matter halo, formed at some time, becomes a part of a larger halo later, in the process of large-scale structure formation. These situations are taken into account in Press-Schechter formalism [99]. This issue in the context of PBH formation has also been noted in the literature as well, for example in [77]. But it may be interesting to note the difference between the halo and PBH case. In the case of dark matter halos, a given halo is *destined* to be involved in a larger halo and this process takes place continuously; a halo forms at some time and in the next instant this halo becomes a part of a slightly larger halo. This is because perturbations of the dark matter always grow and the formation of a halo is determined solely by whether the amplitude of the density perturbation, smoothed over each scale, exceeds the threshold value $\sim 1.68$ (for the spherical case), irrespective of the timing (in this case the notion of the horizon crossing does not play any role since the halo formation takes place well inside the horizon). For the case of PBHs, the double-(or potentially multiple-)formation does not always take place, and when it happens it happens basically discretely (the next PBH formation, involving another smaller PBH or PBHs inside, takes place after some finite time interval). This is because whether a perturbation collapses to form a PBH has already been determined by the time of the horizon crossing, and if it does not collapse, it disperses completely.

inflation is sixty and the universe is instantaneously reheated at the end of the inflation to be dominated by radiation. Let us consider the probability of PBH formation on small scales. If we assume Gaussianity of primordial perturbations, then the perturbation amplitude $\delta$ smoothed over some scale at the moment of the horizon crossing follows a Gaussian distribution $\sim e^{-\delta^2/2\sigma^2}$ (here we neglect the prefactor). Noting the perturbed region with $\delta \sim 1$ collapses to a PBH and setting $\sigma = 10^{-5}$, extrapolating the observationally determined value on large scales to small scales, the probability of PBH formation is roughly estimated by $\sim e^{-1/2(10^{-5})^2} \sim 10^{-10^{10}/2\log_{10} e}$, which seems hopelessly small for PBHs to be formed. However, the universe is vast, and so we have a huge number of dices to be rolled in the universe, which fact also needs to be taken into consideration before jumping to a conclusion when we discuss potential observational consequences of PBHs. Let us consider the shortest scale $e^{-60}\times$Gpc, for which we have the maximum number of dices. There are roughly $(e^{60})^3 = 10^{180\log_{10} e}$ boxes of this length in the current observable universe. This is still enormously smaller than the inverse of the probability above, and so there is no way for PBHs to leave observational traces, under the assumption of the almost-scale-invariant Gaussian perturbations. If PBHs leave meaningful observational traces, one needs either larger typical amplitude of small-scale primordial perturbations, realized in previously mentioned [57] for instance, or non-Gaussian statistics of primordial perturbations. In Chapter 3, a phenomenological inflationary model is discussed which can predict non-Gaussian perturbations, leading to adjustable probability of PBH formation, and so this model may, for instance, explain the supermassive black holes observed at high redshifts. Conclusive observational evidence for the existence of PBHs (both in the present and in the past) has not been found, discussed in the next subsection, and this non-existence of PBHs can be used to constrain properties of primordial perturbations, as is discussed in the subsection after the next one.

### 2.2.5 Observational constraints on PBHs

If the probability of PBH formation in the early universe is sufficiently large, they can leave a number of possible observational consequences. So far there has been no conclusive evidence found for the existence (both in the present and in the past) of PBHs, and so various observations have placed upper bounds on the abundance of PBHs on each mass scale. These observational upper bounds were updated and summarized in [12]. A few of observational constraints or implications are concisely described in the following.

If PBHs in the mass range $10^{-7}M_\odot \lesssim M_{\rm PBH} \lesssim 10M_\odot$ exist, they cause detectable gravitational microlensing, so they may explain (part of) Massive Compact Halo Objects (MACHOs) observed in microlensing experiments. Note that MACHOs behave as cold dark matter, and so they were a good candidate of dark matter, but the possibility of MACHOs explaining the entire dark matter has already been excluded by MACHO collaboration (1998) [100] and EROS collaboration (2006) [101].

As was shown by Hawking (1974) [102], BHs slowly lose their mass by emitting high energy particles (Hawking radiation). PBHs with initial mass less than $\sim 10^{15}g$ have completed evaporation by now, and high energy particles emitted in the past or in the present can also leave observational traces. For instance, PBHs with initial mass $\sim 10^{10}g$ complete evaporation at around the epoch of BBN, when the Hawking radiation from these PBHs is most intense, and high energy particles emitted then affect processes of BBN,

which affect the abundance of the light elements in the universe. That is, observations which determine the abundance of the light elements can be used to place upper bounds on the abundance of these small-mass PBHs.

PBHs have attracted attention partly because they may explain (part of or the entire) dark matter. Up until recently, there has been a "window" of mass scales of PBH dark matter, $10^{20}$g-$10^{26}$g [12], namely, PBHs in this mass range have been a viable candidate of dark matter. In other words, in this mass range, the tightest upper bounds on PBHs had been obtained by noting the abundance of PBHs can not exceed the current abundance of dark matter. However, more recently, progress has been made in the observational constraint of PBHs in this window. Several authors have claimed that the possibility of PBHs being all the dark matter has been excluded based on microlensing [103] and PBH capture by neutron stars [104, 105] and stars [106]. Therefore, the window for PBH dark matter has been narrowed substantially. However, this is not the whole story. Several authors have claimed that Hawking radiation stops when the mass of PBHs reaches the Planck mass, with so called "Planck mass relics" left, and these relics can also provide a viable candidate of dark matter [107] (see also [12] and references therein). It would be fair to say that the relative importance of Planck mass relics being dark matter has been increased since the aforementioned window has been diminishing, and so further exploration of this possibility is much awaited.

PBHs may also explain supermassive black holes (SMBHs). SMBHs of $10^9 - 10^{10} M_\odot$ at high redshifts $z \sim 9 - 10$ have been observed, but how such massive BHs have been formed is still unknown. It is more difficult for astrophysical processes to explain the most massive SMBHs found at highest redshifts observed, than the smaller SMBHs at lower redshifts, and so it would be more important and interesting to investigate the possibility of PBHs explaining those SMBHs at high redshifts. This issue will be explored in more detail in Chapter 3.

### 2.2.6 Upper bounds on primordial small-scale power from PBHs

Here we revisit this issue briefly using simplified arguments and estimations. For more detailed, rigorous discussions see e.g. Josan, Green, Malik (2009) [17] and Bugaev and Klimai (2008) [16] (see also Peiris and Easther (2008) [108] and references therein). We assume the amplitude of primordial perturbations is much larger than that on largest observable scales mentioned above, only at around some particular small scale. Let us consider density perturbations $\delta$ on comoving hypersurfaces smoothed over this scale when this scale reenters the horizon, denote the root-mean-square (RMS) amplitude of $\delta$ by $\sigma$, and assume that $\delta$ follows a Gaussian distribution. The question we address here is, how small $\sigma$ should be, in order not to overproduce PBHs to a level that is inconsistent with observations, a few of which are mentioned in the previous subsection. The probability of PBH formation is roughly given by the following:

$$\begin{aligned}\beta &= \int_{\delta_{\rm th}}^{\infty} \frac{d\delta}{\sqrt{2\pi\sigma^2}} \exp\left(-\frac{\delta^2}{2\sigma^2}\right) = \int_{\delta_{\rm th}}^{\infty} \frac{d\delta}{\sqrt{2\pi\sigma^2}} \frac{-\sigma^2}{\delta} \left\{\exp\left(-\frac{\delta^2}{2\sigma^2}\right)\right\}' \\ &= \frac{\sigma}{\sqrt{2\pi}\delta_{\rm th}} \exp\left(-\frac{\delta_{\rm th}^2}{2\sigma^2}\right) - \int_{\delta_{\rm th}}^{\infty} \frac{d\delta}{\sqrt{2\pi\sigma^2}} \frac{\sigma^2}{\delta^2} \exp\left(-\frac{\delta^2}{2\sigma^2}\right). \end{aligned} \tag{2.3}$$

Since the probability of PBH formation has be be extremely rare, $\sigma \ll \delta_{\rm th}$, and so the second term here is negligible. In addition, the prefactor of the first term can be neglected, to a first approximation. Then the above can be solved for $\delta_{\rm th}/\sigma$ as $\delta_{\rm th}/\sigma \sim \sqrt{-2\log\beta}$. This approximation can be easily improve by including the dropped prefactor, for which this first approximation can be plugged in, with the result being[†8]

$$\frac{\delta_{\rm th}}{\sigma} \simeq \sqrt{-2(\log\beta + \log\sqrt{-4\pi\log\beta})}. \tag{2.7}$$

This relation is plotted in Fig.2.1, which shows the dependence of $\delta_{\rm th}/\sigma$ on $\beta$ is quite week. As is shown in Carr et al. [12], observational upper bounds on $\beta$ are roughly $10^{-15} - 10^{-25}$, depending on the mass of PBHs or the scale of perturbations collapsing to PBHs, so in order not to overproduce PBHs, we require

$$\frac{\delta_{\rm th}}{\sigma} \gtrsim 10, \quad \sigma^2 \lesssim (0.1\delta_{\rm th})^2 \simeq 2\times 10^{-3}, \tag{2.8}$$

where we have used the threshold value $\delta_{\rm th} \simeq 0.4$, obtained in [80,81]. Note that $\sigma^2 \sim \mathcal{P}_{\mathcal{R}}$, the comoving curvature perturbation, which is often used in the literature. The above inequality shows that peaks in density field collapsing to PBHs have to be rarer than "ten-$\sigma$ peaks", which are extremely rare, in order not to overproduce PBHs. So we can constrain small-scale perturbations by PBHs, and this is basically the only way[†9] to probe primordial perturbation all the way down to shortest scales. This is because if perturbations on

[†8] This result can also be derived with the help of the Lambert's W function as follows. First, (2.3) can be rewritten as

$$\frac{1}{2\pi\beta^2} \simeq \frac{\delta_{\rm th}^2}{\sigma^2}\exp\left(\frac{\delta_{\rm th}^2}{\sigma^2}\right), \tag{2.4}$$

which leads to

$$\frac{\delta_{\rm th}^2}{\sigma^2} \simeq W_0\left(\frac{1}{2\pi\beta^2}\right), \tag{2.5}$$

with $W_0$ denoting a branch of the Lambert's W function definde by $z = W(z)e^{W(z)}$. The properties of this function are well understood, and for instance $W_0(x) = \log x - \log\log x + \mathcal{O}(1)$ for large $x$. This leads to

$$\begin{aligned} W_0\left(\frac{1}{2\pi\beta^2}\right) &\simeq -2\log\beta - \log 2\pi - \log\{-(2\log\beta + \log 2\pi)\} \\ &= -2\left(\log\beta + \log\sqrt{-4\pi\log\beta\,\{1 + (\log 2\pi)/2\log\beta\}}\right), \end{aligned} \tag{2.6}$$

the square root of which coincides with (2.7) aside from a tiny correction.

[†9]Strictly speaking there is another method to probe primordial perturbations on extremely small scales. As mentioned earlier, perturbations to the metric or the energy momentum tensor can be decomposed into scalar, vector and tensor components. In linear theory, they evolve independently, but they mix at the level of the second-order in perturbations. For instance, second-order scalar perturbations can generate tensor perturbations, which are sometimes called induced gravitational waves. This means that any upper bounds on high frequency cosmological GWs can be translated into upper bounds on primordial scalar perturbations, which issue is discussed by Assadullahi and Wands [109]. This also indicates that observational upper bounds on induced gravitational waves can be used to place upper bounds on the abundance of PBHs, as is discussed by Saito and Yokoyama in 2009 [110] and in 2010 [111].

these scales fail to collapse to PBHs, which lead to a wealth of phenomenology, they start propagation due to pressure, and also they are exponentially damped due to the diffusion damping, discussed later. This means the information about primordial perturbations on extremely small scales is lost[†10].

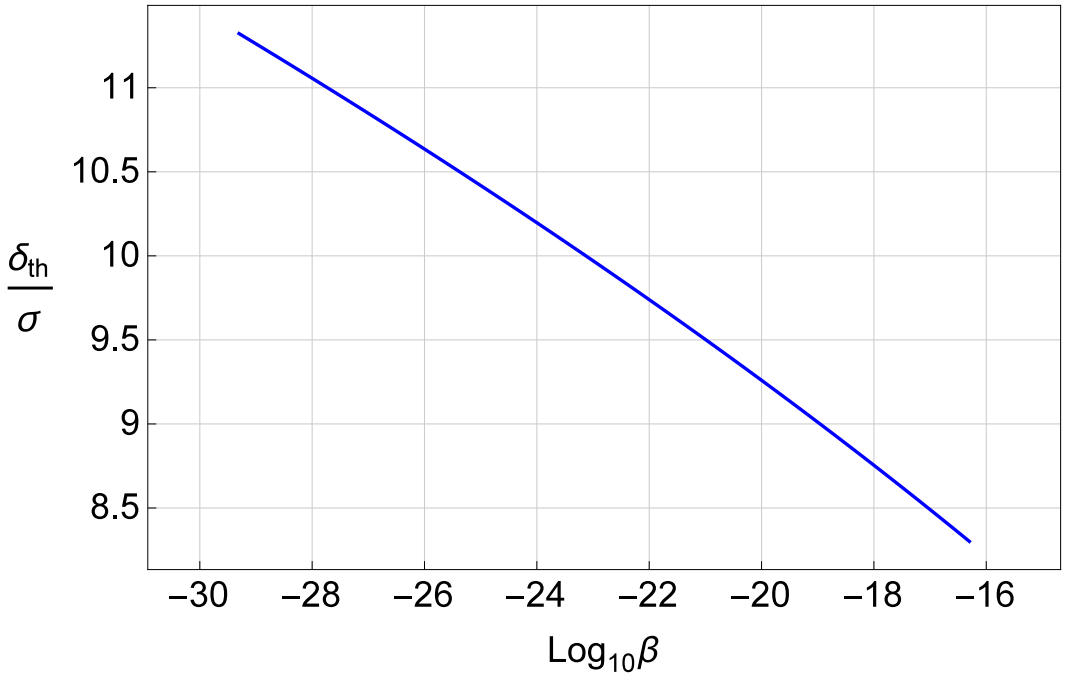


Figure 2.1: The plot of $\delta_{\rm th}/\sigma$ as a function of $\beta$ (eq.(2.7)).

## 2.3 CMB spectral distortion

Observations of CMB anisotropy have provided precious information about large-scale primordial perturbations (see e.g. [8]), or, equivalently, about the early universe when primordial perturbations are generated. There is another aspect of CMB, which is the energy spectrum, and this provides complementary information about primordial perturbations. Here we give an overview of CMB spectral distortion.

There are three important processes which determine the photon spectrum in the early universe: Compton scattering (CS) $e+\gamma \to e+\gamma$, bremsstrahlung (BS) $e+p \to e+p+\gamma$ and double Compton scattering (DS) (or radiative scattering) $e+\gamma \to e+\gamma+\gamma$. Note that CS only redistributes photon in frequency, without changing the number of photons, while BS and DS can change the number of photons. At sufficiently high redshifts, all of these three processes are efficient, or the typical time scales of these processes are much shorter than the cosmological time scale, and so the full thermodynamic equilibrium is

[†10]When they are damped due to diffusion damping, the energy stored in sound waves is released, but if this happens before the BBN, there is no way to probe such energy release. If it happens after the beginning of BBN, then it can be probed by acoustic reheating and CMB spectral distortions. These issues will be discussed later.

maintained (CS helps to maintain the kinetic equilibrium and BS and DS maintain the chemical equilibrium). In these circumstances the photon spectrum is always described by a Planck spectrum, which is fully specified by only one parameter, the temperature of the universe $T$. Suppose some energy $\Delta\rho_\gamma$ is injected into the photon bath (possible examples of energy injection mechanisms are described below), then due to energy conservation the energy density increases $\rho_\gamma \to \rho_\gamma + \Delta\rho_\gamma$. Photons are redistributed in frequency due to Compton scattering, to maintain a Planck spectrum with an increased temperature $T + \Delta T$, with $\Delta T/T = \Delta\rho_\gamma/4\rho_\gamma$. Furthermore, the number of photons has increased, to maintain the relation $n_\gamma \propto (T + \Delta T)^3$, which is possible thanks to DS and BS. That is, to maintain a Planck spectrum the two conditions are necessary, which are readjustment of number of photons (BS and DS), and redistribution of photons in frequency (CS). At lower redshifts one or both of these conditions are not satisfied and hence CMB spectrum deviates from a black body when some sort of energy release happens.

As the universe expands, the efficiencies of these processes decrease, partly because the number density of relevant particles, photons, electrons and protons decreases. At high redshifts $3 \times 10^5 \lesssim z$ [112][†11] DS is more important than BS, and DS becomes inefficient at $z \sim z_\mu \equiv 2 \times 10^6$, below which redshift any energy injection into the photon bath leads to deviation of the photon spectrum from a Planck distribution. This is because photons can no longer be produced efficiently by BS nor DS, namely, chemical equilibrium can not be maintained. For $z_y \equiv 5 \times 10^4 \lesssim z \lesssim z_\mu$, Compton scattering is still efficient, and in this case the photon spectrum becomes a Bose-Einstein distribution, with an effective positive chemical potential $\mu$. Energy injection during this redshift range leads to positive $\mu$, and so this epoch is often called $\mu-$era[†12]. At lower redshifts $z \lesssim z_y$, energy injection causes a global $y$-distortion, and so this epoch is sometimes called "$y$-era". COBE/FIRAS measured the CMB photon spectrum, and it turned out to be described by a Planck distribution quite well; COBE/FIRAS placed tight ($2\sigma$) upper bounds $\mu$ and $y$ distortions, $\mu \lesssim 9 \times 10^{-5}$ and $y \lesssim 1.5 \times 10^{-5}$ [114]. Future experiments are expected to constrain CMB distortions much tighter, or possibly detect CMB distortions. The expected $2\sigma$ detection limits of the Primordial Inflation Explorer (PIXIE) are $\mu \simeq 2 \times 10^{-8}$ and $y \simeq 4 \times 10^{-9}$ [115]. Recently another satellite mission PRISM was proposed, which has ten times the spectral sensitivity of PIXIE [116].

Constraints or future detection of CMB distortions carry vital information about possible physical processes involving energy injection in the early as well as late-time universe. There are several possible mechanisms which inject energy into the photon bath, and these mechanisms would be divided into two categories; astrophysical and cosmological mechanisms. The former includes Sunyaev-Zel'dovich effect, i.e. energy of hot electrons in e.g. clusters of galaxies, is transferred to lower-energy photons (inverse Compton scattering),

[†11] The reaction rates of CS, BS and DS are conveniently compared with the expansion rate in e.g. [112].

[†12] In reality CMB spectral distortions caused by any mechanisms are spatially inhomogeneous, namely, potentially observed CMB spectral distortions would be anisotropic, but the anisotropy of CMB spectral distortions (caused by cosmological processes) would be much harder to measure, and so usually attention is paid to the homogeneous part of CMB spectral distortions, when CMB distortions of cosmological origins are discussed. However, it would worthwhile to mention that anisotropy of CMB spectral distortions themselves also contain rich information, such as primordial non-Gaussianity of perturbations [113].

which distorts the energy spectrum of CMB photons (see e.g. [117]). The latter includes diffusion damping of primordial perturbations, which is one of the most plausible cosmological mechanisms since primordial perturbations on small scales must have existed, though the amplitude of them is unknown. We focus on this aspect of CMB spectral distortion in this dissertation.

Other possible energy injection mechanisms include (see. e.g. [118] and references therein) reionization and structure formation, evaporation of PBHs, accretion disks around PBHs, dissipation of perturbations induced by cosmic strings, energy injection due to shrinking cosmic string loops (this was recently discussed in Anthonisen et al. (2015) [119]), dissipation of small-scale magnetic fields, annihilation or decay of particles, and so all of these mechanisms can be probed by CMB spectral distortion. Potential distinction of several mechanisms of energy is discussed in [118]. During radiation domination, density perturbations $\delta_r$ of radiation on sub-horizon scales are characterized by two important physical processes; one is acoustic oscillation, or sound wave propagation driven by pressure forces of radiation, and sound waves carry fractional energy density of $\sim \delta_r^2$. Secondly, $\delta_r$ on sufficiently small scales at each epoch is damped due to Silk damping or diffusion damping, simply due to the diffusion of (basically) photons[†13]. The diffusion scales, below which scales perturbations are damped, can be roughly given by the mean free path of photons, in the presence of free electrons. Due to diffusion damping, the energy originally stored in sound waves is transferred into the background universe. Energy injection due to diffusion damping happening during the $\mu-$era and $y-$era causes $\mu$ and $y$ distortions. A Fourier mode is damped when the wavelength of that mode becomes comparable to the diffusion scale, determined by photon diffusion. Modes with comoving wavenumber $50\mathrm{Mpc}^{-1} \lesssim k \lesssim 10^4\mathrm{Mpc}^{-1}$ dissipate during the $\mu-$era (see e.g. [121]), so observational upper bounds on $\mu$ can be translated into upper bounds on the amplitude of these modes, while longer-wavelength modes cause $y$ distortion and so these can be in principle constrained by $y$ distortion. The magnitude of these distortions is roughly estimated by the amount of the fractional energy injection, and this amount can be roughly estimated by the energy stored in sound waves, $\sim \delta_r^2$. That is, $\mu, y \sim \delta_r^2$, and so the COBE/FIRAS upper bounds of $\mu, y \lesssim 10^{-5}$ are roughly translated into upper bounds on $\delta_r^2$ as $\delta_r^2 \sim \mathcal{P}_\zeta \lesssim 10^{-5}$ on corresponding scales which dissipate during the $\mu-$ or $y-$era, which provide precious information about the early universe. See [121] for more detailed discussions, where current/future constraints on several types of the power spectrum of the primordial curvature perturbation are presented, which can be translated into constraints on inflationary models which predict small-scale power larger than the standard almost-scale-invariant perturbation. Energy injection due to diffusion damping happening before the $\mu-$era causes only the global (slight) rise $\Delta T \sim \delta_r^2$ of the temperature of

[†13]To be more precise, the diffusion scale at each epoch is determined by [120]

> "the particle that is most weakly interacting, yet still kinetically coupled and as abundant as radiation".

The diffusion scale is determined by photons only for $z \lesssim 10^7$, and it is determined by other particles such as neutrinos at higher redshifts. That is, as long as we are interested in dissipation of acoustic waves for $z \lesssim 10^7$, which matters for CMB spectral distortions, we can assume the diffusion scale at each moment is determined by photons. So in the text we focus only on diffusion due to photons.

the universe, and this has not received much attention for a long time since cosmological CMB distortions have been intensively studied by e.g. Sunyaev and Zel'dovich (1970) [20]. More recently however, small-scale perturbations which damp before the $\mu-$era are also found to be constrained [43, 120]. This is discussed in Chapter 4 in detail, but it would be worthwhile to give a brief sketch here about this issue.

In [43] we argued that the slight global rise of the temperature $\Delta T \sim \delta_r^2$ (termed "acoustic reheating"), causes the fractional change of the baryon-to-photon ratio, $\Delta\eta/\eta \sim -\delta_r^2$. On the other hand, since $\eta$ at BBN and photon decoupling have been observationally inferred by the abundance of light elements of the universe and CMB anisotropy, if $\eta$ changes considerably between these events, it contradicts with these observations. Roughly we should require $|\Delta\eta/\eta| \lesssim \mathcal{O}(0.1)$, and so we obtain $\delta_r^2 \lesssim \mathcal{O}(0.1)$. The constraints from acoustic reheating will be discussed in Chapter 4 in more detail.

## 2.4 Dark matter mini-halos as a probe of primordial power on small scales

Perturbations in DM grow after the horizon reentry, slowly (or logarithmically) during radiation domination, and more rapidly (in proportion to the scale factor) during matter domination. Overdense regions can be locally regarded as closed universes, and the expansion of these regions becomes slower and slower. At some moment in time, this region stops expanding and starts to contract and finally collapses, at which moment the amplitude estimated by extrapolating linear theory reaches $\delta \simeq 1.7$, according to the so-called spherical collapse model.

Shorter wavelength modes reenter the horizon earlier, and hence they have more time to grow during radiation domination. That is, small-scale perturbations become nonlinear earlier, and smallest halos are formed first, and later they become part of even larger halos.

If we assume so-called weakly interacting massive particles (WIMPs) as DM, the minimum mass of halos is determined by the free streaming of DM, erasing DM perturbations below the free streaming scale, and also by the horizon scale at the moment of the kinetic decoupling, before which modes inside the horizon are damped due to the acoustic oscillation (see e.g. [122]). The minimums mass is determined by the larger of the scales determined by these mechanisms, and this depends on the temperature at the kinetic decoupling and the free streaming scale. Typically, the minimum mass is roughly the same as the earth mass ($\sim 10^{-6} M_\odot$). These smallest halos are formed at $z \sim \mathcal{O}(10)$, if we assume the standard almost scale-invariant power spectrum.

Recently, dark matter minihalos have attracted attention as a method to probe primordial power on small scales. Riccoti and Gould (2009) [22] pointed out that primordial perturbations which are smaller than $\mathcal{O}(1)$, but larger than $\sim 10^{-3}$, do not collapse to form PBHs at horizon crossing, but later collapse in the early universe ($z \sim 10^3$), much earlier than the formation of DM halos from the standard almost scale-invariant perturbations, and they called these halos formed at high redshifts as ultracompact minihalos (UCMHs). They calculated light curves of microlensing events caused by these UCMHs, and concluded that these can be distinguished from those caused by point-like objects. That is, they proposed UCMHs as a novel type of the so-called massive compact halo objects (MACHOs), and these are far more extended than the conventional point-like

MACHOs.

If we assume the standard almost scale-invariant Gaussian perturbations, smallest halos are formed at $z \sim \mathcal{O}(10)$, and the probability of halos formed at $z \sim 1000$ would be vanishingly small. However, if the typical amplitude of primordial perturbations is much larger than the standard value $\delta \sim 10^{-5}$, say, $\delta \sim 10^{-3}$, then UCMHs are formed abundantly at high redshifts (though the probability of PBH formation would be still vanishingly small). If these UCMHs survive the processes of relatively recent standard structure formation, they would be observed as their gravitational or dynamical effects, or annihilation signals from these UCMHs. In other words, any constraints on UCMHs can be translated into constraints on primordial power on small scales, just as observational upper bounds on PBHs do. For instance, since Ricotti and Gould have pointed out that UCMHs can cause microlensing, we can immediately place upper bounds on them through microlensing experiments, to constrain primordial power on some range of scales, the corresponding DM mass of which causes observable microlensing, though none has explicitly obtained such bounds yet as far as the author is aware.

Annihilation signals from UCMHs also provide a method to probe UCMHs. The annihilation rate of DM is determined by the square of the density, and as a result clumpiness of DM enhances annihilation signals. To precisely calculate annihilation signals from UCMHs, DM profile of them is needed. Recent works of UCMHs (e.g. [23]) adopt what is known as the secondary infall model (see e.g. Bertschinger (1985) [123]). In [123], a spherically symmetric initial overdensity in the Einstein de-Sitter universe is considered and its subsequent time evolution is analytically analyzed. When the amplitude of this initial overdensity becomes nonlinear, this initial overdensity stops expanding and starts to contract, or turn around, and finally to form a virialized object. If we consider some spherical shell whose radius is sufficiently larger than the initial overdensity, the density perturbation averaged inside this shell would be still in the linear regime, and so this shell is still expanding, but the expansion rate is smaller than the average in the universe, and it gets smaller and smaller as the density perturbation smoothed inside the shell grows. At some moment in time, the smoothed density perturbation inside this shell even becomes nonlinear, and this shell also collapses (secondary infall), and this process repeats. Bertschinger analyzed this process using self-similar solutions, and found that resultant profiles of collapsed objects are described by $\rho \propto r^{-9/4}$ for a collisionless gas.

Constraints on UCMHs or primordial power on small scales obtained from gamma-rays from DM constituting UCMHs have been investigated by Bringmann, Scott and Akrami (2012) [23] in detail. They assume the profile is described by the secondary infall model $\rho \propto r^{-9/4}$ outside some radius $r_c$, within which the density is assumed to be constant. They consider two physical mechanisms determining $r_c$, one of which is the breakdown of radial infall near the center; the profile $\rho \propto r^{-9/4}$ was obtained under the assumption of spherical symmetry, or perfectly radial infall of matter, but in reality infalling matter has non-zero angular momentum, so $\rho \propto r^{-9/4}$ would be naturally violated near the center. Another mechanism which potentially determines $r_c$ is annihilation of DM; if one believes $\rho \propto r^{-9/4}$ is correct up to the center, $\rho$ becomes infinitely large, and hence annihilation becomes infinitely efficient there, which would result in the decrease in the density near the center. They determine $r_c$ so that the time scale of the annihilation at the central core is comparable to the cosmological time scale. They assume a pair of WIMPs always

annihilate into $b\bar{b}$, with $\langle\sigma v\rangle = 3\times10^{-26}\mathrm{cm}^3\mathrm{s}^{-1}$[†14], as well as $m_\chi = 1\mathrm{TeV}$. Under these assumptions, they find annihilation is more important than the breakdown of radial infall in determining $r_c$. They constrain UCMHs as galactic or extra-galactic point sources, assuming no unassociated point sources reported by Fermi-LAT represent UCMHs. They also constrain UCMHs from diffuse components of gamma-rays observed by Fermi-LAT.

They estimate the probability of a region of comoving size $R$ later collapsing to UCMHs by the amplitude of perturbations of DM $\delta_\chi$ as follows:

$$\beta(R) = \frac{1}{\sqrt{2\pi}\sigma_{\chi,H}(R)}\int_{\delta_\chi^{\min}}^{\delta_\chi^{\max}} \exp\left(-\frac{\delta_\chi^2}{2\sigma_{\chi,H}(R)^2}\right)d\delta_\chi. \tag{2.9}$$

Perturbations larger than $\delta_\chi^{\min}$ later collapse to form UCMHs, while those larger than $\delta_\chi^{\max}$ collapse to form PBHs shortly after the horizon reentry, and $\delta_\chi^{\max}$ is something like $1/3$ or $0.5$, but this values is not so important in estimating the abundance of UCMHs, which is mostly determined by $\delta_\chi \simeq \delta_\chi^{\min}$. One may define UCMHs as minihalos which collapse before some redshift $z_c$, say $z_c \sim 1000$, before which the secondary infall model describes UCMH formation relatively well, and in this case $\delta_\chi^{\min} \sim 10^{-3}$. Bringmann et al. calculate $\delta_\chi^{\min}$ more rigorously based on the linear perturbation theory and the spherical collapse model, as a function of $k$ and $z_c$. $\delta_\chi^{\min}$ decreases as $k$ increases or $z_c$ decreases, since in these cases perturbations have more time to grow after horizon reentry. They refer to $z_c = 1000$ as their canonical value. They relate the mass variance of DM perturbations in the comoving gauge at the horizon reentry to the dimensionless power spectrum $\mathcal{P}_\mathcal{R}$ of the curvature perturbation as

$$\sigma_{\chi,H}(R)^2 = \frac{1}{9}\int_0^\infty x^3 W_{\mathrm{TH}}^2(x)\mathcal{P}_\mathcal{R}(x/R)T_\chi^2(x/\sqrt{3})dx, \tag{2.10}$$

where $x = kR$, $W_{\mathrm{TH}}(x)$ is the Fourier transformed top-hat window function, and the transfer function $T_\chi$ is given by

$$T_\chi(\theta) = \frac{6}{\theta^2}\left[\ln\theta + \gamma_E - \frac{1}{2} - \mathrm{Ci}(\theta) + \frac{1}{2}j_0(\theta)\right], \tag{2.11}$$

where $\gamma_E$ is the Euler-Mascheroni constant, Ci is the cosine integral function, and $j_0$ is the spherical Bessel function of the first kind. The above integration is mostly determined by the parts with $x \sim 1$, or $k \sim k_R = 1/R$, namely, this variance reflects the power spectrum of the curvature perturbation at around this wavenumber. They assume local scale invariance at around $k_R$, and find $\sigma_{\chi,H}^2(R)/\mathcal{P}_\mathcal{R}(k_R) = 0.907$. Then, constraints on UCMHs of each mass scale can be translated into constraints on $\sigma_{\chi,H}^2(R)$, with $R$ corresponding to that mass of UCMHs, or equivalently into constraints on $\mathcal{P}_\mathcal{R}(k = k_R)$. They report upper bounds on $\mathcal{P}_\mathcal{R}(k)$ from Fermi-Lat observations as $\mathcal{P}_\mathcal{R}(k) \lesssim 10^{-7} - 10^{-6}$ in $10\mathrm{Mpc}^{-1} < k < 10^7\mathrm{Mpc}^{-1}$, with constraints tighter on larger $k$ due to more time for growth of perturbations, but the dependence on $k$ is only logarithmic, reflecting the

[†14]This value of $\langle\sigma v\rangle$ is the so-called "canonical value", which can explain the current abundance of DM, and also which can be naturally obtained assuming the typical strength of electroweak interactions. This coincidence is sometimes referred to as "WIMP miracle" (see e.g. [124]).

logarithmic growth during radiation domination[†15]. UCMH constraints on the power spectrum are compared with other constraints, such as CMB, LSS and PBHs in their Fig.6.

It would be natural to assume that DM particles annihilate into standard model particles other than photons as well, and so UCMHs may be constrained by observations other than gamma-rays. Yang, Yang and Zong (2013) [125] use potential neutrino signals from UCMHs, and constrain them by demanding that the neutrino flux from UCMHs on earth be less than the flux of atmospheric neutrinos.

The properties of DM, such as annihilation modes, the annihilation cross section, and the mass of DM need to be assumed to place upper bounds on primordial power from annihilation signals, such gamma-rays or neutrinos. If DM properties are revealed in future, with moderate annihilation cross section, then these can be used as reliable upper bounds on primordial power, providing viable information about the early universe, but, needless to say, if they do not annihilate much these constraints are useless. Hence, at this stage one may regard these as joint constraints on the properties of DM, and primordial power.

In this sense, constrains on UCMHs from their dynamical or gravitational effects may be more promising, which are expected to be less sensitive to the properties of DM, one of which is gravitational microlensing caused by UCMHs mentioned above. Another example is astrometric microlensing caused by UCMHs, which is change of the apparent position of a star due to the variation of the gravitational field when a UCMH transpasses between the observer and the star. Li, Erickcek and Law (2012) [126] forecast constraints on primordial power assuming the Gaia mission [127]. They adopt the model of DM profiles in UCMHs similar to that used in [23], namely, the combination of the secondary infall model $\rho \propto r^{-9/4}$ and the constant core determined by the angular momentum of infalling DM or annihilation, and so the inner profile is affected by DM annihilation. Since the magnitude of astrometric microlensing turns out to be sensitive to the inner profile, their predicted constraints on primordial power also depend on DM properties, even though they discuss gravitational effects of UCMHs.

Most recently, Clark, Lewis and Scott (2015) [128, 129] have discussed constraints on UCMHs and primordial power by their effects on pulsar timing observations. Their constraints are probably less dependent on DM properties or DM profiles inside UCMHs than those obtained previously, and hence the reported upper bounds seem to be more robust.

[†15]They also obtained upper bounds from the effects of gamma-rays from UCMHs on reionization of the universe, and these are roughly one order of magnitude weaker than constraints from Fermi-LAT.

# Chapter 3

# Primordial black holes as potential seeds of supermassive black holes at high redshifts

Observations have revealed the existence of supermassive black holes (SMBHs) of about $10^9 M_\odot$ at high redshifts $z = 6 \sim 7$; so far, about 40 quasars, which are thought to be SMBHs blazing by accreting the surrounding gas, have been discovered [24–36]. In particular, a quasar suggesting an SMBH as massive as twelve billion-solar-mass was discovered recently [37]. Up to the present time, there is no established astrophysical explanation[†1] of why such massive black holes could have already existed in such high

[†1]There are several possible explanations of SMBHs at high redshifts, one of which is the so-called direct collapse model. According to this model, massive BHs $\sim 10^5 M_\odot$ are first formed as a result of collapse of supermassive stars of $\sim 10^5 M_\odot$ (see e.g. a recent work [130] and references therein).

Another candidate for the SMBHs at high redshifts is the remnants of Population III stars of $10^{2-3} M_\odot$. However, this scenario may be in tension with the standard ΛCDM cosmology, due to the lack of sufficient time for these seeds to grow to become SMBHs of $10^9 - 10^{10} M_\odot$ at high redshifts, which we briefly review following Bramberger et al. [131]. If a BH is accreting at a fraction $\lambda$ of the Eddington rate, its emitted luminosity is $L = \lambda M c^2 / t_* = \epsilon \dot{M}_{\rm acc} c^2$, where $t_* \simeq 4.5 \times 10^8$yrs is the Eddington time, $\epsilon$ is the accretion efficiency and $\dot{M}_{\rm acc}$ is the matter falling onto the black hole. The growth rate of the BH $\dot{M}$ is thus given by $\dot{M} = (1-\epsilon)\dot{M}_{\rm acc}$, since a fraction $\epsilon$ of the accreted mass is converted into energy and thus escapes the BH. These lead to the following expression for the growth from $M_{\rm i}$ to $M_{\rm f}$ as

$$M_{\rm f} = M_{\rm i} \exp\left( \frac{1-\epsilon}{\epsilon} \frac{\Delta t}{t_*} \lambda \right). \tag{3.1}$$

They adopt $(\epsilon, \lambda) = (0.1, 1)$, and from the above formula find that the seeds of $10^2 - 10^3 M_\odot$ have to be present already at $z \gtrsim 40$ to explain a recently discovered SMBH of $1.2 \times 10^{12} M_\odot$ at $z = 6.3$, which is noted to be unlikely under the assumption of Gaussian fluctuations in the standard ΛCDM cosmology. They estimated the mass of nonlinear objects whose comoving separation is Mpc, which roughly corresponds to that between galaxies, and this mass turns out to be much smaller than $10^2 M_\odot$ at $z \gtrsim 20$.

Note that above the Eddington rate is kept throughout the growth ($\lambda = 1$), and super-Eddington accretion may ameliorate the tension. In addition, if early structure formation is

redshifts when the age of the universe is less than a billion years (see e. g. [134–138] for reviews of SMBHs in the high-redshift universe).

In light of this situation, it is intriguing to consider a possibility that the observed SMBHs are primordial black holes (PBHs) which formed in the very early universe when the universe was still dominated by radiation [139], as is discussed in Chapter 2 in more detail. If some region has perturbation of order of unity, this region undergoes gravitational collapse shortly after the size of the region becomes comparable to the Hubble horizon [14, 15]. Typically, the mass of the resultant black hole is roughly equal to the horizon mass at the formation time (see (2.1)). Noting the formation time of PBHs can be related to the (comoving) scale of the perturbations collapsing to PBHs, the mass of PBHs can also be related to the (comoving) scale of the perturbations (see (2.2)). At first sight, the desired amount of PBHs of the desired mass, as large as necessary to grow to even $10^{10}M_\odot$ by $z \sim 6, 7$, can be formed by just preparing moderate probability of primordial perturbations of order unity at the corresponding (comoving) scale. Such perturbations can be indeed realized in some inflation models [38, 57–59, 61–74]. Note that the sufficient formation of such black holes does not happen in the standard cosmology in which primordial perturbations are almost scale-invariant and Gaussian [140], as is discussed in Chapter 2. Although the approximate scale invariance and Gaussianity of the primordial perturbation are observationally confirmed at large scales, namely the scales relevant to observations of the cosmic microwave background (CMB) (for the recent Planck results, see [141, 142]) or large-scale structures of the universe, these properties could be largely violated on much shorter scales, including the scales corresponding to the PBHs relevant to the seeds of SMBHs considered in this Chapter.

However, simply enhancing the amplitude of the primordial perturbation at the PBH scale to the value that yields sufficient amount of SMBHs is already excluded from the observations of the energy spectrum of CMB photons [39, 121, 140, 143]. To see this let us assume Gaussianity of the primordial perturbation, and note that the requirement that produced PBHs are sufficient enough to explain the abundance of the observed SMBHs fixes the typical amplitude, or the root-mean-square (RMS) amplitude, of the perturbations [140]. This amplitude is fairly greater than the upper limit set by non-detection of the distortion of the CMB spectrum by COBE [114], which severely restricts the validity of the scenario of PBHs exceeding $\sim 10^4 - 10^5 M_\odot$ as the origin of the SMBHs [39][†2]. The root of this constraint is the fact that requiring the formation of sufficient amount of PBHs inevitably leads to large inhomogeneities everywhere in the universe. More precisely, even though the site of PBH formation, where primordial perturbation is the order of unity, is rare, a Gaussian (or similar) probability density function (PDF) implies perturbations everywhere else take large enough amplitude, whose diffusion damping distorts the energy spectrum of CMB photons from a perfect Planck distribution (CMB distortion) at a level excluded by COBE measurement (see the left panel of Fig. 3.1). See Chapter 2 for more details about CMB distortion. There is possibility that PBHs whose initial mass is $\sim 10^4 - 10^5 M_\odot$ grow to explain SMBHs of $10^9 - 10^{10} M_\odot$ at high redshifts, as is argued

enhanced, one can ameliorate this tension. They resorted to cosmic string loops in [131], and to primordial non-Gaussianity in [132]. A blue-tilted primordial power spectrum of scalar perturbations may also help [133].

[†2]Smaller PBHs are also potentially excluded by compact dark matter halos [39] (or UCMHs, briefly discussed in Chapter 2) and acoustic reheating [43, 120], discussed in Chapter 4.

in [38], but whether PBHs can grow to these masses is uncertain. One of the benefits of resorting to PBHs is that one can create sufficiently large black holes in the early universe due to collapse of primordial perturbations, but this benefit seems to have been partially lost due to CMB $\mu-$distortion. Also, future experiments may reveal even more massive SMBHs at higher redshifts.

In this light, we propose a novel inflationary scenario in which density perturbations are generated yielding PBHs *larger* than $10^4 - 10^5 M_\odot$ as the origin of SMBHs while evading the constraint from CMB distortion mentioned above. The idea is to assume that the PDF of primordial perturbation smoothed on some small scale, corresponding to the scale of the seeds of SMBHs, is basically bimodal and has two sharp peaks of different heights as shown in the right panel of Fig. 3.1. We require that one spike is located at zero with small enough variance (for instance, the variance simply extrapolated from the observations of perturbations on large scales) and the other at amplitude of order unity from which PBHs can be formed. The height of the spike for PBHs must be much smaller than the other so that in most regions of the Universe primordial perturbations are small and sites of PBH formation are rare, as is required by the observations [24]. The PDF is negligibly small between the spikes, which ensures that there is virtually no place where primordial perturbation is smaller than that for PBH formation but is considerably larger than the upper limit set by the CMB distortion. In this way, the constraint from the CMB distortion can be satisfied while producing sufficient amount of PBHs.

After revisiting CMB distortion constraints on PBHs in the next section, we will discuss a mechanism of how such a non-Gaussian PDF can be realized in the framework of inflation. We also provide two simple toy models in which such a mechanism is realized. We focus on the most massive SMBHs ($10^9 - 10^{10} M_\odot$) observed high redshifts, since it is more difficult for astrophysical processes to explain these. In the last section, we discuss consequences of our scenario and how it can be tested and distinguished from astrophysical explanations.

As already mentioned, simply preparing Gaussian perturbations whose dispersion is sufficiently large to generate PBHs as the seeds of SMBHs is inconsistent with constraints of CMB distortion. One may first try to evade this by a monotonically decreasing PDF whose tail is considerably enhanced than a Gaussian one, different from a bimodal PDF discussed in this Chapter. In the Appendix B, this possibility is briefly explored, by calculating CMB distortion for a class of phenomenological models of PDFs. It turns out that it may work (if such a PDF can be indeed realized in some inflationary model, which we do not discuss any further here,) but the PDF has to be tremendously distorted from a Gaussian PDF.

This Chapter is based on a part of [39] and on a work in preparation [40], and is organized as follows: In §3.1, constraints on the abundance of PBHs obtained from CMB $\mu$-distortion are revisited. Then in §3.2 we discuss inflationary models, in which PBHs can be produced whose mass and abundance are adjustable to explain SMBHs observed at high redshifts, and we summarize and conclude in §3.3.

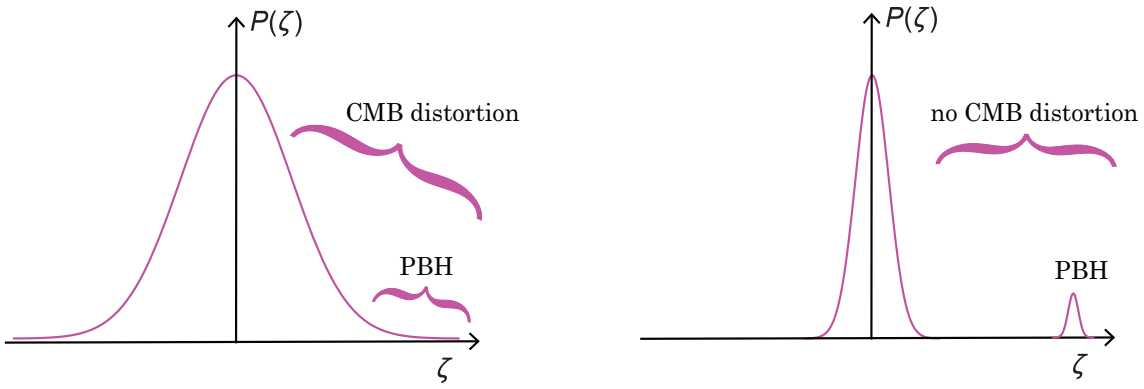


Figure 3.1: Left figure: The probability density function $P(\zeta)$ of the curvature perturbation $\zeta$ which is Gaussian or Gaussian-like. In this case, significant CMB distortion which is incompatible with the COBE/FIRAS measurement is induced if we require PBHs explain the SMBHs. Right figure: An illustration of the probability density function $P(\zeta)$ realized in the model proposed in this Chapter. In this case, only negligible CMB distortion is induced even if we require PBHs explain the SMBHs.

## 3.1 Constraints on the abundance of PBHs obtained from CMB $\mu$-distortion

Constraints on the abundance of PBHs obtained from CMB distortions were investigated in 1993 and 1994 by Carr et al. [140, 143]. Also in Chluba et al. (2012) [121] (here after CEB) the upper bound on the amplitude of the primordial power spectrum from CMB distortions for the locally scale-invariant spectrum with a Gaussian filter was compared with PBH upper bound, and the former was shown to be a few orders of magnitude tighter than the PBH bound around $10\mathrm{Mpc}^{-1} \lesssim k \lesssim 10^4\mathrm{Mpc}^{-1}$. In this section, following CEB, we briefly revisit this issue by considering $\delta$-function shape of the primordial power spectrum[†3]. In CEB, the primordial power spectrum of curvature perturbation was decomposed as follows;

$$P_\zeta = P_\zeta^{\mathrm{st}}(k) + \Delta P_\zeta(k), \tag{3.2}$$

where the first term represents the standard almost scale-invariant power spectrum, which has been determined by CMB experiments accurately, with the second term denoting the deviation from this standard spectrum. Let us consider the $\delta$-function like $\Delta P_\zeta(k)$

[†3]In typical models (e.g., [38]) predicting the formation of PBHs as the seeds of SMBHs, the power spectrum of curvature perturbation has a sharp peak, the height of which exceeds $\mathcal{O}(0.01)$. The width of the peak should be finite but it cannot be arbitrarily wide to avoid overproduction of PBHs of masses irrelevant to the seeds of SMBHs. In addition, if we take into account the effects of the finite width of the spectrum, it leads to more production of $\mu$ distortion since in this case more than one $k$-modes contribute to $\mu$ distortion. For example, if we consider a step-like power spectrum $\Delta P_\zeta(k) = 2\pi^2 A_\zeta k^{-3}(1\mathrm{Mpc}^{-1} < k), 0(\text{otherwise})$, the resultant $\mu$ distortion is $\mu \sim 11 A_\zeta$ (see CEB). Therefore, for our purpose here it is sufficient to restrict our attention to a delta-function like power spectrum.

parameterized as follows:

$$\Delta P_\zeta(k) = 2\pi^2 A_\zeta k^{-2} \delta(k - k_*). \tag{3.3}$$

They found that the $\mu$ distortion originating from a single $k$-mode is approximated by

$$\mu \sim 2.2 A_\zeta \left[ \exp\left( -\frac{\hat{k}_*}{5400} \right) - \exp\left( -\left[ \frac{\hat{k}_*}{31.6} \right]^2 \right) \right], \tag{3.4}$$

where $k_* = \hat{k}_* \mathrm{Mpc}^{-1}$. The COBE/FIRAS experiment provides the $2\sigma$ upper limit as $\mu \lesssim 9 \times 10^{-5}$ [114]. Noting that $A_\zeta \gtrsim \mathcal{O}(0.01)$ is necessary to produce PBHs to an observationally relevant level [17], we can plot $\mu$ as a function of $\hat{k}_*$. Fig. 3.2 shows the plot of $\mu$ with $A_\zeta$ fixed to 0.02. We find that any spike with $A_\zeta \gtrsim 0.02$ in a range $1 \lesssim \hat{k}_* \lesssim 3 \times 10^4$ produces $\mu$ larger than the COBE/FIRAS upper bound. Therefore, PBHs formed from the density perturbation in the above $\hat{k}_*$ range are excluded. This conclusion is insensitive to the change of $A_\zeta$ (as long as it is $\mathcal{O}(0.01)$), as is evident from the figure. Since $k_*$ is related to the PBH mass (see Eq. (2.2)), the above $\hat{k}_*$ range can be translated into the PBH mass range as (from (2.2)) $2 \times 10^4\ M_\odot \lesssim M_{\rm PBH} \lesssim 2 \times 10^{13}\ M_\odot$[†4]. PBHs in this mass range are basically ruled out, at least for Gaussian perturbations (see the subsequent sections and the Appendix B for non-Gaussian cases)[†5].

## 3.2 Supermassive black holes formed from inflationary perturbations

### 3.2.1 Basic idea

Our basic idea is the following. Let us first recall that our observable universe consists of many small patches which become causally disconnected during inflation. For instance, if we consider a patch of comoving wavenumber $k$, it becomes decoupled from the other patches of the same size at a time when $k = aH$. After this time, each patch evolves independently as if they themselves were an individual Friedmann-Lemaitre-Robertson-Walker (FLRW) universe. If the inflation is caused by a slowly rolling single field, only adiabatic perturbation is generated. In this case, each patch follows the same trajectory in field space and the difference between the patches is just the difference of time when the field value takes a particular value. On the other hand, if the inflation is caused

[†4]Density perturbations corresponding to larger PBH masses generate $y$-type distortion which is also constrained by the COBE/FIRAS experiment. From the view point of the observed supermassive black holes, such PBHs are too heavy and we do not consider this case.

[†5]This point was also noted in [38], but they concluded PBHs with $M_{\rm PBH} > 10^5 M_\odot$ are severely constrained, and this upper bound of mass is slightly larger than the one we obtain here ($M_{\rm PBH} \simeq 2 \times 10^4 M_\odot$). This is because, in [38], the upper bound was obtained by assuming only the perturbation modes which dissipate during the $\mu-$era are severely constrained, but strictly speaking the transition to the $\mu-$era is continuous, and modes which dissipate before the onset of $\mu-$era can also cause $\mu-$distortion and hence be constrained, though weakly, and this effect is taken into account in our calculation based on CEB.

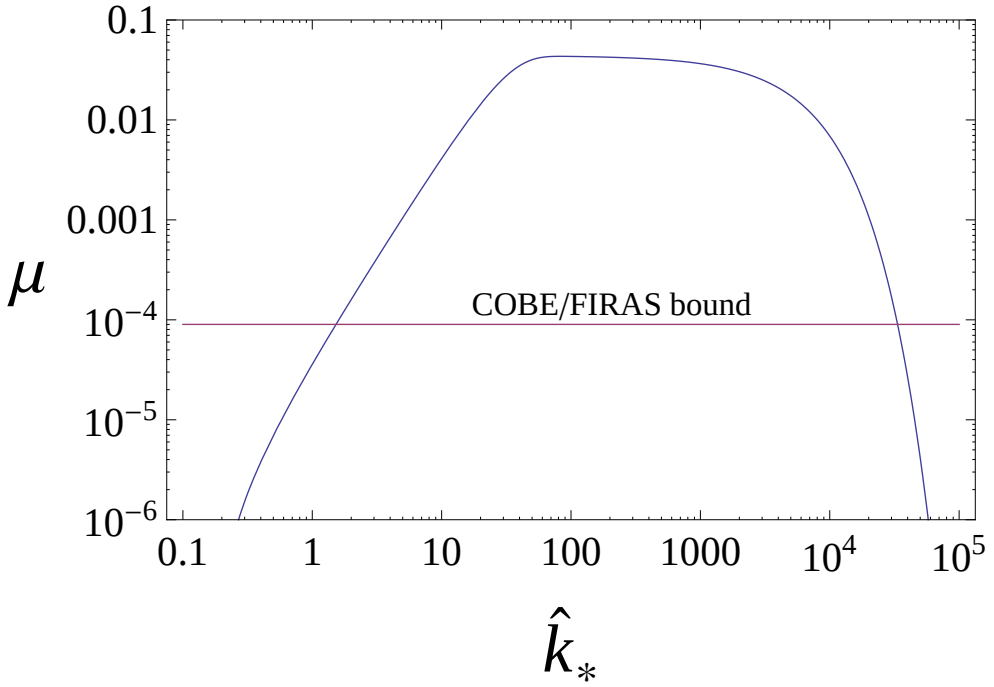


Figure 3.2: The $\mu$ distortion generated from a single $k$-mode, with $A_\zeta = 0.02$. The horizontal line corresponds to the $2\sigma$ upper limit provided by COBE/FIRAS.

by multiple fields, isocurvature perturbation as well as adiabatic one is also generated. Because of the presence of the isocurvature mode, each patch follows different trajectories in field space in general. In the following, we assume multiple field inflation.

Now, suppose that there are essentially only two different trajectories that each patch can follow (see the left panel of Fig. 3.3). Let us label each trajectory by A and B, respectively (see the right panel of Fig. 3.3). In general, the patches corresponding to A and the patches corresponding to B, after causally disconnected, expand by different amount, namely, $N_A \neq N_B$ ($N_A(N_B)$ is the number of e-folds in the patches A(B)). According to the $\delta N$ formalism [51, 144–148], $N_A - N_B$ is equal to the curvature perturbation $\zeta$ on constant density hypersurfaces. See the Appendix C for a brief review of $\delta$N formalism.

It is known that if the region of interest has $\zeta$ exceeding $\zeta_c \simeq 1$, such a region undergoes gravitational collapse to form a black hole when it reenters the Hubble horizon [15]. The threshold value $\zeta_c$ depends on perturbation profile and there is a lot of literature in which the determination of $\zeta_c$ as well as its dependence on the perturbation profile has been investigated (see Chapter 2 for more details). However, precise knowledge of $\zeta_c$ is not crucial for our discussions here and so we simply take $\zeta_c = 1$.

Let us assume that most of the patches followed the trajectory A and the trajectory B is followed by a small number of patches and that $N_B - N_A > \zeta_c = 1$. Then the patches corresponding to B distribute sparsely and each is surrounded by patches corresponding to A and each patch B has positive curvature perturbation $N_B - N_A$. In other words, large curvature perturbation of $\zeta > \zeta_c$ is generated only in the patches B and no substantial curvature perturbation is generated by the present mechanism in the patches A occupying

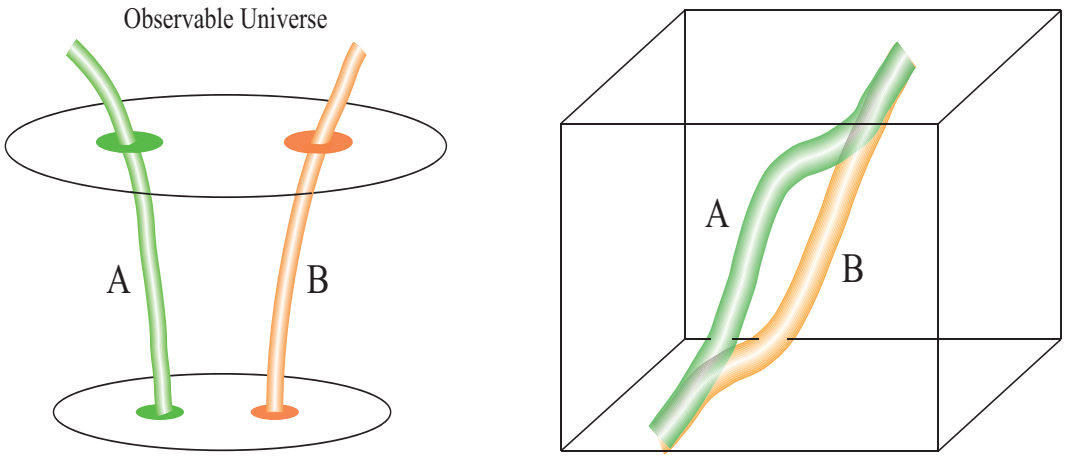


Figure 3.3: Left figure: This shows the separate universe picture in which patch A and B evolve independently as if each were an FLRW Universe. Right figure: Trajectories in field space corresponding to patch A and B, respectively.

most part of the universe. Because of our assumption that $N_B - N_A > \zeta_c$, each patch B turns into a BH upon horizon reentry. Noting that the mass of the resultant BH is directly related to the comoving size of the patch B, the time when the trajectories A and B start to deviate determines the BH mass. In this Chapter we consider two inflation models which can realize these situations with appropriately chosen model parameters.

Denoting by $\beta$ the probability that a region whose size is the same as that of patches B collapses to a BH, $\beta$ is given by

$$\beta = \frac{\text{number of patches B}}{\text{number of patches A}}. \tag{3.5}$$

The rareness of the patches B means $\beta \ll 1$, which is required by observations as we will show below.

Observations of SMBHs at high redshifts suggest that one SMBH of $M_{\rm BH} \sim 10^{10} M_\odot$ exists roughly in every comoving volume of 1 Gpc$^3$ [24]. Taking these as fiducial, we find the present energy density of these SMBHs normalized by the present critical density $\rho_c$, denoted by $\Omega_{\rm BH,0}$, from the observations is given by

$$\Omega_{\rm BH,0} = \frac{M_{\rm BH}}{\rho_c V} \approx 7 \times 10^{-11} \left(\frac{M_{\rm BH}}{10^{10} M_\odot}\right) \left(\frac{V}{\rm Gpc^3}\right)^{-1}. \tag{3.6}$$

In order to relate $\beta$ with $\Omega_{\rm BH,0}$, let us note that the mass of a BH that formed at a redshift $z$ is given by

$$M_{\rm BH} \simeq \frac{1}{2GH(z)}, \tag{3.7}$$

where $H(z)$ is the Hubble parameter at $z$. From this equation, we find $M_{\rm BH} = 6 \times 10^{17}\, M_\odot$ if it is formed at the matter-radiation equality $z = z_{\rm eq}$. Hence BHs with $M_{\rm BH} \lesssim 10^{10} M_\odot$, which we are interested in, formed in the radiation-dominated epoch. Using $H(z) = H_0 (1+z)^2 \sqrt{\Omega_{r,0}}$, valid for $z > z_{\rm eq}$, we have

$$1 + z = 2 \times 10^7 \left(\frac{M_{\rm BH}}{10^{10} M_\odot}\right)^{-1/2}. \tag{3.8}$$

Then, using a relation $\Omega_{\rm BH,0} = \beta\Omega_{r,0}(1+z)$, we have

$$\beta = 4\times 10^{-14}\left(\frac{M_{\rm BH}}{10^{10}M_\odot}\right)^{3/2}\left(\frac{V}{\rm Gpc^3}\right)^{-1}. \tag{3.9}$$

Thus, observations require $\beta \ll 1$. Note that the initial mass of PBHs does not have to be $\sim 10^{10}M_\odot$ to explain the observed SMBHs at high redshifts, since the mass of PBHs should grow to some extent, mainly after the matter-radiation equality since the growth during radiation domination is known to be quite limited. The accurate description of the growth of mass on a cosmological time scale would be a formidable task, which is beyond the scope of this work. However, we can adjust the typical mass of PBHs formed in our models simply by changing $\phi_{\rm BH}$ introduced later, so this issue won't affect the feasibility of our model. Also, it would be more natural to expect that only a fraction of SMBHs shine to be observed at high redshifts and so the total number density of SMBHs, including those which are too dim to be observed, would be larger than $\sim 1{\rm Gpc}^{-3}$ mentioned above. However, the uncertainty of $\beta$ stemming from these two issues does not affect the feasibility of our model, since $\beta$ turns out to only affect $\bar{\chi}$ estimated later in (3.28) slightly.

### 3.2.2 Simple model 1: a hill on top of $\phi^2$ potential

In this subsection, we provide a two-field inflation model in which PBHs as the observed SMBHs are produced by the mechanism we explained in the previous subsection. The Lagrangian density we consider is given by

$$\mathcal{L} = -\frac{1}{2}(\partial\phi)^2 - \frac{1}{2}(\partial\chi)^2 - V(\phi)\left(1+\theta(\chi)v(\phi)\right), \tag{3.10}$$

where $\theta(\chi)$ is the unit step function. Inflation is caused by the potential $V(\phi)$ for $\chi<0$ and $V(\phi)(1+v(\phi))$ for $\chi>0$. To be definite, we adopt the following functions for $V(\phi)$ and $v(\phi)$;

$$V(\phi) = \frac{1}{2}m^2\phi^2, \qquad v(\phi) = \alpha\exp\left(-\frac{(\phi-\phi_0)^2}{2\mu^2}\right). \tag{3.11}$$

Here $\alpha$ is a positive dimensionless parameter. Then, the field $\phi$ in the positive $\chi$ region rolls down the potential which is higher than the negative $\chi$ region. Thus, trajectories in the positive $\chi$ region experience a greater number of e-folds than those in the negative $\chi$ region. In terms of the definition introduced previously, trajectories with negative/positive $\chi$ correspond to patches A and B, respectively (see Fig. 3.4).

We describe how the above inflation model can realize the mechanism described in the previous subsection. The first thing to do is to evaluate the initial condition of each patch of the comoving size $k_{\rm BH}^{-1}$ corresponding to the mass of SMBHs when each patch becomes causally disconnected. In other words, we have to determine how different the field values in the two classes of patches eventually have to take to form PBHs. To this end, let us denote by $\phi_{\rm obs}$ and $\bar{\chi}$ the values of the scalar fields when the current observable universe crosses the Hubble horizon during inflation. At this moment, all the patches of the comoving size corresponding to the SMBHs are well deep inside the Hubble horizon and roughly take the same values $(\phi_{\rm obs},\bar{\chi})$. We require $\bar{\chi}<0$ so that the

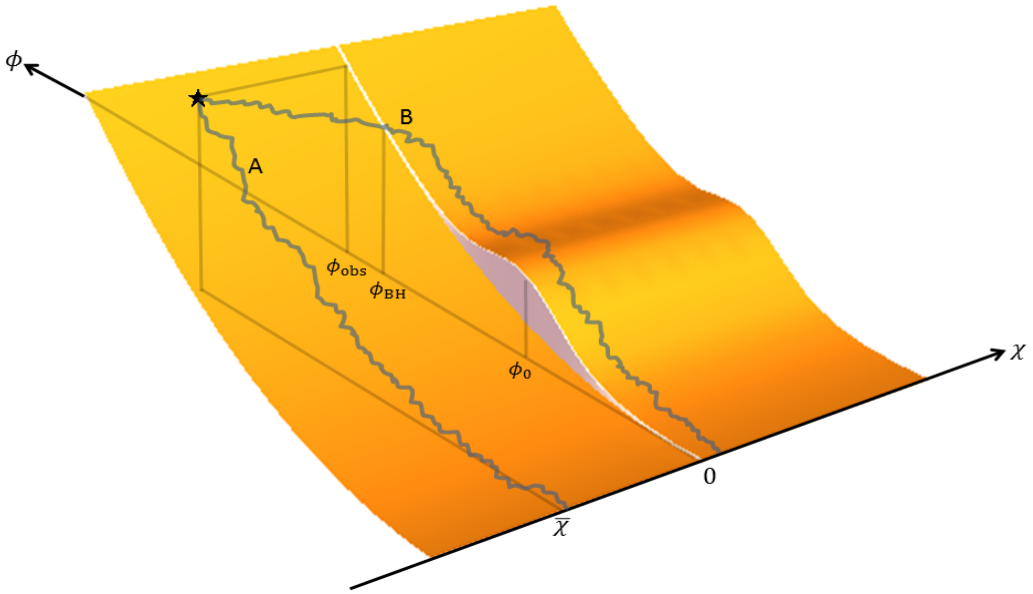


Figure 3.4: Illustrations of trajectories of mini-universes A and B in field space for the potential given by Eq. (3.11). Suppose there exists a hill at $\phi = \phi_0$ for $0 < \chi$, and all trajectories are assumed to start at $(\phi, \chi) \simeq (\phi_{\rm obs}, \bar{\chi})$, denoted by the star in this figure. Zigzag trajectories reflect quantum fluctuation of $\chi$, and if the absolute magnitude of $\bar{\chi}(< 0)$ is sufficiently large, only an extremely rare fraction of the patches of $\sim k_{\rm BH}$ enter into the region $0 < \chi$, subsequently reaching the hill. The amount of expansion is different between these two types of trajectories, and so patches experiencing the hill are where the curvature perturbation is locally large. If the hill is sufficiently wide and high, the amplitude of this curvature perturbation becomes order unity, leading to the formation of PBHs. The mass and abundance of PBHs can be roughly controlled by the position of the hill and $\bar{\chi}$, to explain SMBHs observed at high redshifts.

most regions of the universe follow trajectories with negative $\chi$ afterwards. By the time when $k_{\rm BH}$ becomes equal to $aH$, regions of comoving size larger than $k_{\rm BH}^{-1}$ but smaller than $k_{\rm obs}^{-1}$, the comoving scale of the current observable universe, have undergone classical slow-roll motion associated with stochastic motion originating from redshifting of the short wavelength vacuum fluctuations [149]. Thus, at the moment when $k_{\rm BH} = aH$, each patch of the comoving size $k_{\rm BH}^{-1}$ has randomly different field values centered at the values determined by the classical slow-roll equations of motion. The distribution of the $\chi$ field value around the center, in this case $\bar{\chi}$, is approximately Gaussian and its variance is given by [1]

$$\langle (\chi - \bar{\chi})^2 \rangle \simeq \frac{H^2}{4\pi^2} (N_{\rm obs} - N_{\rm BH}), \tag{3.12}$$

where $N_{\rm obs} - N_{\rm BH}$ is the number of e-folds between the time when the observable universe crossed the Hubble horizon and the one when the size of $k_{\rm BH}^{-1}$ crossed the Hubble horizon. Approximating that $H$ remains almost constant during that period, we have $N_{\rm obs} - N_{\rm BH} \simeq \ln(k_{\rm BH}/k_{\rm obs})$.

After the time $k_{\rm BH} = aH$, each patch of the comoving size $k_{\rm BH}^{-1}$ becomes causally

disconnected and the fields on each patch evolve independently from the others. Adopting the viewpoint of the separate universe picture [148], we make an assumption that the fields on each patch behave as spatially uniform fields which obey classical equations of motion for the homogeneous fields in the FLRW spacetime whose expansion is also determined by the field values in the same patch. Each patch follows different trajectories in field space due to different field values at the time $k_{\rm BH} = aH$. However, because of the special form of the potential we consider, only whether $\chi$ is positive or negative matters in terms of the number of e-folds. In this sense, there are essentially only two trajectories in field space (trajectories with positive $\chi$ and negative $\chi$) and the model can effectively realize the mechanism described previously. The condition that the patches having positive $\chi$ (the patches B in the language introduced previously) yield curvature perturbation greater than $\zeta_c$ imposes constraints among the model parameters. In addition to this, in order for the above inflation model to be successful for explaining the origin of SMBHs, the model also needs to achieve the observationally suggested values of $\beta$ and $M_{\rm BH}$, without stopping the classical motion of the $\phi-$field, or equivalently with the potential in the $\phi$ direction being everywhere monotonically decreasing, basically. We will show that there is a parameter space where all the conditions are simultaneously satisfied[†6].

Let us discuss how to calculate the curvature perturbation on $k_{\rm BH}^{-1}$ more closely, working in a box of comoving size $k_{\rm obs}^{-1} \sim \mathcal{O}(\rm Gpc)$. Let us first discuss the amplitude of the curvature perturbation on $k_{\rm BH}$, when this mode exits the horizon at $t_{\rm BH}$, noting that, as is discussed shortly, the effects of the hill are chosen to be negligible up to $\phi_{\rm BH}$. First, the amplitude of field fluctuations $\delta\phi$ and $\delta\chi$ on flat slices are given by (see e.g. [150])

$$\mathcal{P}_{\delta\phi,\delta\chi}(t_{\rm BH}, k_{\rm BH}) = \left(\frac{H_{k_{\rm BH}}}{2\pi}\right)^2, \tag{3.13}$$

where $H_{k_{\rm BH}}$ is the Hubble parameter when the mode $k_{\rm BH}$ exits the horizon. We assume that the energy density of $\chi$ is always negligible, and so the curvature perturbation $\zeta$ on uniform-density slices at $t_{\rm BH}$ is solely determined by $\delta\phi$ and is given by $\zeta = -H\delta\phi/\dot{\phi}$. Hence, the power spectrum of the curvature perturbation at $t_{\rm BH}$ is

$$\mathcal{P}_\zeta(t_{\rm BH}, k_{\rm BH}) = \frac{1}{4\pi^2}\left(\frac{H^2}{\dot{\phi}}\right)^2 = \frac{1}{24\pi^2 M_{\rm Pl}^4}\frac{V}{\epsilon}. \tag{3.14}$$

Without the presence of the hill ($\alpha = 0$), fluctuations on $k_{\rm BH}$ just correspond to the time difference on the essentially same trajectory, noting that in this case $\chi$ does not affect cosmic expansion and hence plays no role, and the curvature perturbation is conserved after $k_{\rm BH}$ exits the horizon. Also, perturbations in this case are Gaussian and almost scale-invariant. These perturbations are determined by $V(\phi)$ and we choose it so that $\mathcal{P}_\zeta \sim \mathcal{O}(10^{-9})$ to match observations on large scales. In this case, the probability of PBH formation is vanishingly small, as is discussed in Chapter 2. Next, let us consider the

[†6] The existence of the parameter space itself may be self-evident, since by increasing the height of the hill $N_B - N_A$ can become arbitrarily large, without stopping the slow-roll motion of $\phi$, noting the complete hindrance of the classical motion of the $\phi$ field corresponds to the limit of $N_B - N_A \to \infty$. So a certain probability of PBH formation would be guaranteed by an appropriate choice of the shape of the hill. Also, the abundance of PBHs or the rareness of patches B can be arbitrarily tuned by the choice of $\bar{\chi}$, as is estimated later.

effects of the hill ($\alpha \neq 0$). After $k_{\rm BH}^{-1}$ exits the horizon, each region of $k_{\rm BH}^{-1}$ can be regarded as evolving as an independent FLRW universe [148]. The metric on uniform density slices may be written as $dx^2 = -dt^2 + \tilde{a}(t,\boldsymbol{x})d^3\boldsymbol{x}$, where $\tilde{a}(t,\boldsymbol{x}) = a(t)\exp[\zeta(t,\boldsymbol{x})]$ is the local scale factor, $a(t)$ is the global scale factor and $\zeta(t,\boldsymbol{x})$ is the curvature perturbation. Here and hereafter, the position-dependent quantities are understood to be those smoothed over the comoving scale of $k_{\rm BH}^{-1}$, not over the Hubble radius at each moment. Let us consider two patches A and B of $k_{\rm BH}^{-1}$ around points $\boldsymbol{x}_A$ and $\boldsymbol{x}_B$, and assume that in most of the regions inside the patch A(B) $\chi$ continues to be negative (positive) for $t > t_{\rm BH}$. Note that, even if $\chi(t_{\rm BH},\boldsymbol{x}_B) > 0$, this does not ensure the positivity of $\chi$ in most of the regions inside the patch B for $t > t_{\rm BH}$. To see this first recall that, after $t_{\rm BH}$, the field values $\phi$ and $\chi$ smoothed over the Hubble radius at each point keep randomly fluctuating by $\sim H$ over the time scale $\sim H^{-1}$. This means that, naively, if $\chi(t_{\rm BH},\boldsymbol{x}_B) > 0$ but $\chi(t_{\rm BH},\boldsymbol{x}_B) \ll H$, roughly half of the region in the patch B would end up having $\chi < 0$, but more precisely due to the sharp wall at $\chi = 0$, hindering crossing from $\chi < 0$ to $\chi > 0$ for $t > t_{\rm BH}$, actually more than half of the region in the patch B would end up having $\chi < 0$. Hence, we need $\chi(t_{\rm BH},\boldsymbol{x}_B) > \mathcal{O}(1)H$ to ensure the positivity of $\chi$ in most of the regions in the patch B for $t > t_{\rm BH}$. The curvature perturbation at $(t_{\rm BH},\boldsymbol{x}_{A,B})$, $\zeta(t_{\rm BH},\boldsymbol{x}_{A,B})$, is of order $\mathcal{O}(10^{-5})$, the same as the case without the hill as explained above since the effects of the hill are negligible up to $t_{\rm BH}$. When the hill is present, the inflaton trajectories for $t > t_{\rm BH}$ qualitatively differ depending on $\chi$, and in this case the curvature perturbation of the patch B grows for $t_{\rm BH} < t < t_{\rm end}$, where $t_{\rm end}$ corresponds to the end of the inflation, and this growth is entirely determined by the difference in the overall expansion histories of the patches A and B for $t > t_{\rm BH}$. This is because, as long as $\chi$ stays negative (positive) in most regions in the patch A (B), quantum fluctuations of $\chi$ on the Hubble radius arizing after $t_{\rm BH}$ essentially do not play any role, in the sense that it no longer affects background expansion. Also, quantum fluctuations of $\phi$ on the Hubble radius arizing after $t_{\rm BH}$ keep being converted to curvature perturbation on $k > k_{\rm BH}$, but this does not affect the curvature perturbation on $k_{\rm BH}^{-1}$ either. To calculate the growth of the curvature perturbation for $t > t_{\rm BH}$ due to the difference in the expansions, let us define the local Hubble parameter $H(t,\boldsymbol{x})$ by

$$H(t,\boldsymbol{x}) \equiv \frac{\dot{\tilde{a}}(t,\boldsymbol{x})}{\tilde{a}(t,\boldsymbol{x})} = \frac{\dot{a}(t)}{a(t)} + \dot{\zeta}(t,\boldsymbol{x}). \tag{3.15}$$

During inflation, the equation of motion for $\phi$ in the patch A is given by

$$3H\dot{\phi} + V'(\phi) \simeq 0, \qquad H^2 \simeq \frac{1}{3M_{\rm Pl}^2}V(\phi), \tag{3.16}$$

where a prime denotes differentiation with respect to $\phi$ and $M_{\rm Pl}$ is the reduced Planck mass, and for the patch B

$$3H\dot{\phi} + \big[V(\phi)(1+v(\phi))\big]' \simeq 0, \qquad H^2 \simeq \frac{1}{3M_{\rm Pl}^2}V(\phi)(1+v(\phi)). \tag{3.17}$$

The numbers of e-folds of the patches A and B from $t_{\rm BH}$ to $t_{\rm end}$ are given by

$$N_A = \frac{1}{M_{\rm Pl}^2}\int_{\phi_{\rm end}}^{\phi_{\rm BH}} d\phi\ \frac{V(\phi)}{V'(\phi)}, \qquad N_B = \frac{1}{M_{\rm Pl}^2}\int_{\phi_{\rm end}}^{\phi_{\rm BH}} d\phi\ \frac{V(\phi)(1+v(\phi))}{\big[V(\phi)(1+v(\phi))\big]'}. \tag{3.18}$$

PBH formation is determined by the difference in the curvature perturbation at the end of inflation, since thereafter it is conserved, and from (3.15) it is expressed as

$$\zeta(t_{\rm end}, \boldsymbol{x}_B) - \zeta(t_{\rm end}, \boldsymbol{x}_A) = \zeta(t_{\rm BH}, \boldsymbol{x}_B) - \zeta(t_{\rm BH}, \boldsymbol{x}_A) + \Delta N, \quad \Delta N \equiv N_B - N_A. \tag{3.19}$$

As mentioned above, $\zeta(t_{\rm BH}, \boldsymbol{x}_{A,B}) \sim \mathcal{O}(10^{-5})$, while we are interested in situations where $\Delta N \sim 1$ to produce PBHs, and so we can safely neglect $\zeta(t_{\rm BH}, \boldsymbol{x}_{A,B})$ and focus on $\Delta N$ in the following. See also the Appendix C for a brief review of $\delta$N formalism.

Let us calculate the relationship between $\phi_{\rm BH}$ and $M_{\rm BH}$. The mass of PBHs $M_{\rm BH}$ is roughly estimated by the horizon mass at the moment when the comoving scale $k_{\rm BH}$ reenters the horizon, from which one finds

$$M_{\rm BH} \sim 2.2 \times 10^{13} M_\odot \left(\frac{k_{\rm BH}}{1{\rm Mpc}^{-1}}\right)^{-2}. \tag{3.20}$$

This can be inverted as follows:

$$k_{\rm BH} \sim 47 \left(\frac{M_{\rm BH}}{10^{10} M_\odot}\right)^{-1/2} {\rm Mpc}^{-1}. \tag{3.21}$$

Noting the following relation

$$\ln\left(\frac{k_{\rm BH}}{k_{\rm obs}}\right) \simeq N_{\rm obs} - N_{\rm BH} = \int_{t_{\rm obs}}^{t_{\rm BH}} dt H \simeq \frac{1}{M_{\rm Pl}^2} \int_{\phi_{\rm BH}}^{\phi_{\rm obs}} d\phi \frac{V}{V'} = \frac{1}{4M_{\rm Pl}^2}(\phi_{\rm obs}^2 - \phi_{\rm BH}^2) \tag{3.22}$$

and setting $k_{\rm obs} = 1{\rm Gpc}^{-1}$, we obtain

$$\phi_{\rm BH} = \sqrt{\phi_{\rm obs}^2 - 4M_{\rm Pl}^2 \log\left(\frac{k_{\rm BH}}{k_{\rm obs}}\right)} \simeq 13\sqrt{1 + 0.01 \log\left(\frac{M_{\rm BH}}{10^{10} M_\odot}\right)}, \tag{3.23}$$

where we have set $N_{\rm obs} = 55$ ($\phi_{\rm obs} \simeq 14.8 M_{\rm Pl}$). Note that the dependence of $\phi_{\rm BH}$ on $M_{\rm BH}$ is very weak, and for instance if we set $M_{\rm BH} = 1 M_\odot$, $\phi_{\rm BH} \simeq 12$. Therefore, though we assume $M_{\rm BH} = 10^{10} M_\odot$ and $\phi_{\rm BH} = 13$ in the following, our analysis is valid for other masses as well. For instance, one may choose the typical initial mass of PBHs to be smaller than $10^{10} M_\odot$, taking account possible mass growth of PBHs.

Note that for each $\mu$, $\phi_0$ has to be sufficiently smaller than $\phi_{\rm BH}$. This is needed in order that the sharp wall of the potential at $\chi = 0$ does not prevent stochastic motion of $\chi$ from crossing the wall at $k_{\rm BH} = aH$ to simplify the subsequent analysis. The criterion that the stochastic motion can cross over the wall freely is that the kinetic energy of $\chi$ field, $\sim H^4$, is larger than the potential gap at $\phi = \phi_{\rm BH}$. If this condition is not satisfied, the wall blocks the stochastic motion effectively and $\chi$ virtually cannot enter the positive region. The height of the potential wall at the peak $\phi = \phi_0$ is given by $\alpha V(\phi_0)$ and this is much larger than $H^4$ in our present model for a range of $\alpha$ in which $\mathcal{O}(1)$ difference of the number of e-folds is generated between A and B. Thus, $\phi_{\rm BH}$ must be located far from the peak where the height of the wall is smaller than $H^4$, which yields

$$R \equiv \frac{H^4}{V(\phi_{\rm BH}) v(\phi_{\rm BH})} \simeq \frac{m^2 \phi_{\rm BH}^2}{18\alpha M_{\rm Pl}^4 \exp\{-(\phi_{\rm BH} - \phi_0)^2/2\mu^2\}} \gg 1. \tag{3.24}$$

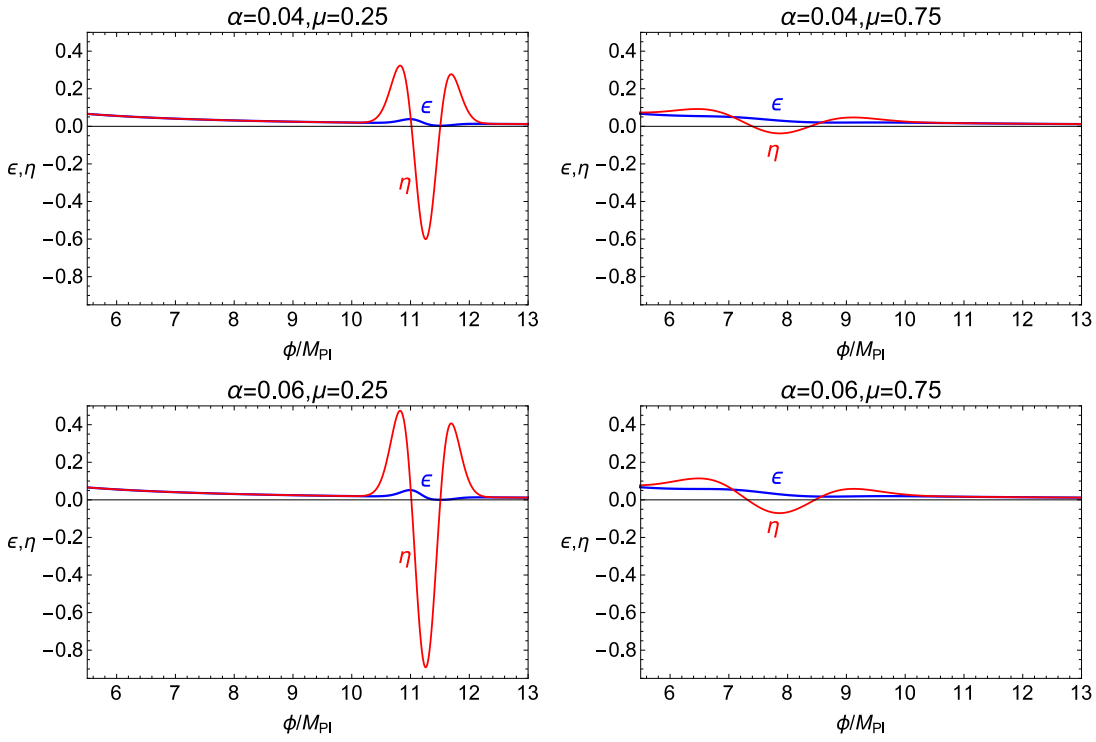


Figure 3.5: The time evolution of the slow-roll parameters for different choices of $\alpha$ and $\mu$.

If we require $R = 100$ and rewrite the exponential factor here by defining $\nu$ as $\phi_{\rm BH} = \phi_0 + \nu\mu$, we can calculate $\nu$ as

$$\nu \simeq 7\left\{1 + \log\left(\frac{\alpha}{0.06}\right)\right\}^{1/2}, \tag{3.25}$$

where we have set $\phi_{\rm BH} = 13$ and $m = 3 \times 10^{-6}$. Hence in the following we set $\nu = 7$[†7]. If $\alpha$ is larger and $\mu$ is smaller, $\Delta N$ is larger, but at the same time the absolute magnitudes of the slow-roll parameters ($\epsilon \equiv M_{\rm Pl}^2 V'^2/2V^2$ and $\eta \equiv M_{\rm Pl}^2 V''/V$) become also larger (see Fig. 3.5). Since our calculation of $\Delta N$ is based on the slow-roll approximation,

[†7]Here we assume the crossing to the positive $\chi$ region happens only at $\phi = \phi_{\rm BH} = 13$, leading to the monochromatic mass function of PBHs at $M_{\rm BH} \simeq 10^{10} M_\odot$. Strictly speaking however, the masses would be distributed around some mass scale determined by $\phi_0$, and this mass spectrum is determined by the following two effects. First, the crossing to the positive $\chi$ region can in principle occur also when $\phi > \phi_{\rm BH}$, though the probability of these cases is exponentially suppressed, since the probability of reaching $\chi = 0$ becomes rapidly rarer as $\phi$ is increased. This leads to a power-law tail of the mass function at larger masses, noting the exponential dependence of $M_{\rm BH}$ on $\phi_{\rm BH}$. Second, the crossing can occur even for $\phi < \phi_{\rm BH}$, though the probability would be increasingly suppressed as $\phi$ becomes closer to $\phi_0$, due to the gap of the potential at $\chi = 0$, for which quantification the probability of crossing with a gap has to be calculated. Or, one may introduce an additional wall at $\chi = 0$ except for $\phi \sim \phi_{\rm BH}$, allowing crossing of $\chi = 0$ only at around $\phi_{\rm BH}$, in which case an almost monochromatic mass function would be realized.

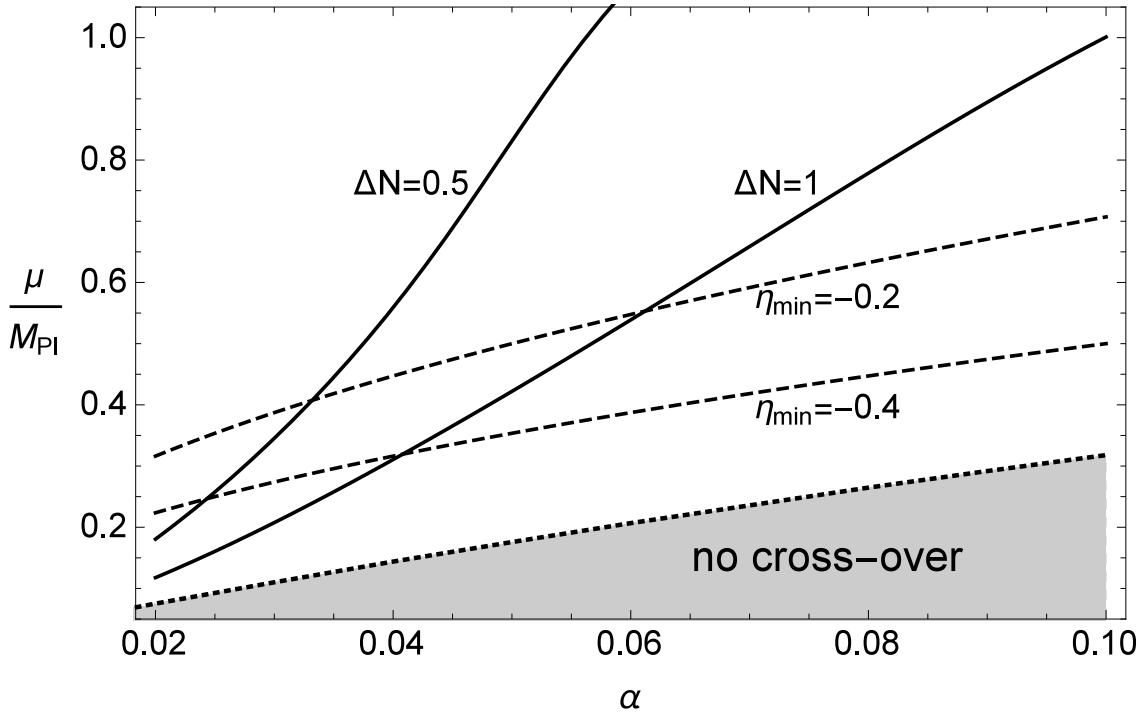


Figure 3.6: A contour plot of $\Delta N \equiv N_B - N_A$ and $\eta_{\rm min}$. For the parameter choices in the shaded region, the inflaton can not cross over the hill, and hence this region is prohibited.

the results where slow-roll conditions are violated are not trustable. It turns out that $\eta$ takes the minimum value at around $\phi_0$, $\eta(\phi_0) \simeq -\alpha/\mu^2 \equiv \eta_{\rm min}$, and ensuring $|\eta(\phi_0)| < 1$ is sufficient to maintain the slow-roll conditions (see Fig. 3.5). A contour plot of $\Delta N$ and $\eta_{\rm min}$ is shown in Fig. 3.6. Roughly, if $\dot\phi (\propto -[V(\phi)(1+v(\phi))]')$ becomes negative somewhere for some parameter choices $(\alpha, \mu)$, the inflaton cannot cross the hill, and so such cases should be excluded. This region is represented by the gray region in the Fig. 3.6. To conclude, there is a parameter space where the curvature perturbation exceeds unity and hence PBHs can be formed (see also the footnote †6), and the resulting SMBHs have mass around $10^{10} M_\odot$.

Finally, let us determine the initial value $\bar\chi$ of $\chi$ which leads to an observationally suggested value of $\beta$. As already mentioned, $\chi$ on the patches corresponding to $k_{\rm BH}$ when $\phi = \phi_{\rm BH}$ is randomly distributed around the central value $\bar\chi$ with its variance given by Eq. (3.12). As a result, noting (3.5) $\beta$ is given by[†8]

$$\beta \simeq \int_0^\infty d\chi \, \frac{1}{\sqrt{2\pi}\sigma_\chi} \exp\left( -\frac{(\chi - \bar\chi)^2}{2\sigma_\chi^2} \right) \simeq -\frac{\sigma_\chi}{\sqrt{2\pi}\bar\chi} \exp\left( -\frac{\bar\chi^2}{2\sigma_\chi^2} \right). \tag{3.26}$$

To obtain the right-hand side we have made an approximation that the integral picks up only the tail of the Gaussian distribution (notice that $\bar\chi < 0$). Solving the above equation

[†8] As explained previously, our calculation of the curvature perturbation at patches B is valid for $\chi(t_{\rm BH}, \boldsymbol{x}_B) > \mathcal{O}(1)H$, so the lower bound of the integration here should be strictly speaking taken as $\mathcal{O}(1)H$, but this only affects $\bar\chi$, evaluated below, only slightly.

for $\bar{\chi}$ yields

$$\bar{\chi} = -\sigma_\chi \sqrt{W_0\left(\frac{1}{2\pi\beta^2}\right)}, \tag{3.27}$$

where $W_0$ is the Lambert function (see the footnote †8 of Chapter 2). Using the expansion of $W_0(x)$ for large $x$ given by $W_0(x) = \ln x - \ln\ln x + \mathcal{O}(1)$, we have

$$\bar{\chi} \simeq -\frac{H}{2\pi}\sqrt{N_{\rm obs} - N_{\rm BH}}\left[ -\ln(2\pi\beta^2) - \ln(-\ln(2\pi\beta^2))\right]^{1/2}. \tag{3.28}$$

Thus, the observed abundance of SMBHs can be realized if $\bar{\chi}$ takes the above value.

### 3.2.3 Simple model 2: a hill on top of $R^2$-inflation type potential

The $\phi^2$ potential considered in the previous subsection is somewhat disfavored by the Planck data [151]. However, our mechanism can work for other types of potentials, including those favored by the Planck data. To see this in this subsection we consider a hill on top of the following potential:

$$V(\phi) = \frac{3M^2 M_{\rm Pl}^2}{4}\left\{1 - \exp\left(-\sqrt{\frac{2}{3}}\frac{\phi}{M_{\rm Pl}}\right)\right\}^2. \tag{3.29}$$

This can be obtained by a conformal transformation (see e.g. [152]) of $R^2-$inflation [47], which is so far favored by the Planck data. The parameter $M$ is fixed by the COBE-WMAP normalization of the amplitude of the curvature perturbations as follows (see e.g. [152]):

$$M \simeq 10^{-5} M_{\rm Pl}\frac{4\pi\sqrt{30}}{N_{\rm obs}}\left(\frac{\mathcal{P}(k_*)}{2\times 10^{-9}}\right)^{1/2} \simeq 1.25\times 10^{-5} M_{\rm Pl}\left(\frac{N_{\rm obs}}{55}\right)^{-1}\left(\frac{\mathcal{P}(k_*)}{2\times 10^{-9}}\right)^{1/2}. \tag{3.30}$$

If we define $\phi_f$ by $\epsilon = 1$, then $\phi_f = \sqrt{\frac{3}{2}}\log\left(1+\frac{2}{\sqrt{3}}\right) M_{\rm Pl} \simeq 0.94 M_{\rm Pl}$. $N_{\rm tot}$ for this model is given by

$$N_{\rm tot} = \frac{3}{4}\left\{\exp\left(\sqrt{\frac{2}{3}}\frac{\phi_{\rm obs}}{M_{\rm Pl}}\right) - \exp\left(\sqrt{\frac{2}{3}}\frac{\phi_f}{M_{\rm Pl}}\right)\right\} - \frac{\sqrt{6}}{4M_{\rm Pl}}(\phi_{\rm obs} - \phi_f). \tag{3.31}$$

This can be approximately solved for $\phi_{\rm obs}$ (neglecting the last two terms above) as

$$\phi_{\rm obs} \simeq \sqrt{\frac{3}{2}} M_{\rm Pl}\log\left\{\frac{1}{3}\left(4N_{\rm tot} + 2\sqrt{3} + 3\right)\right\}. \tag{3.32}$$

We set $N_{\rm tot} = 55$ and then $\phi_{\rm obs} \simeq 5.3 M_{\rm Pl}$. Then $\phi_{\rm BH}$ can be determined as follows:

$$\begin{aligned} N_{\rm obs} - N_{\rm BH} &\simeq \ln\left(\frac{k_{\rm BH}}{k_{obs}}\right) \simeq 10.8\left\{1 + 0.21\log_{10}\left(\frac{M_{\rm BH}}{10M_\odot}\right)\right\} \\ &\simeq \frac{3}{4}\left\{\exp\left(\sqrt{\frac{2}{3}}\frac{\phi_{\rm obs}}{M_{\rm Pl}}\right) - \exp\left(\sqrt{\frac{2}{3}}\frac{\phi_{\rm BH}}{M_{\rm Pl}}\right)\right\}, \end{aligned} \tag{3.33}$$

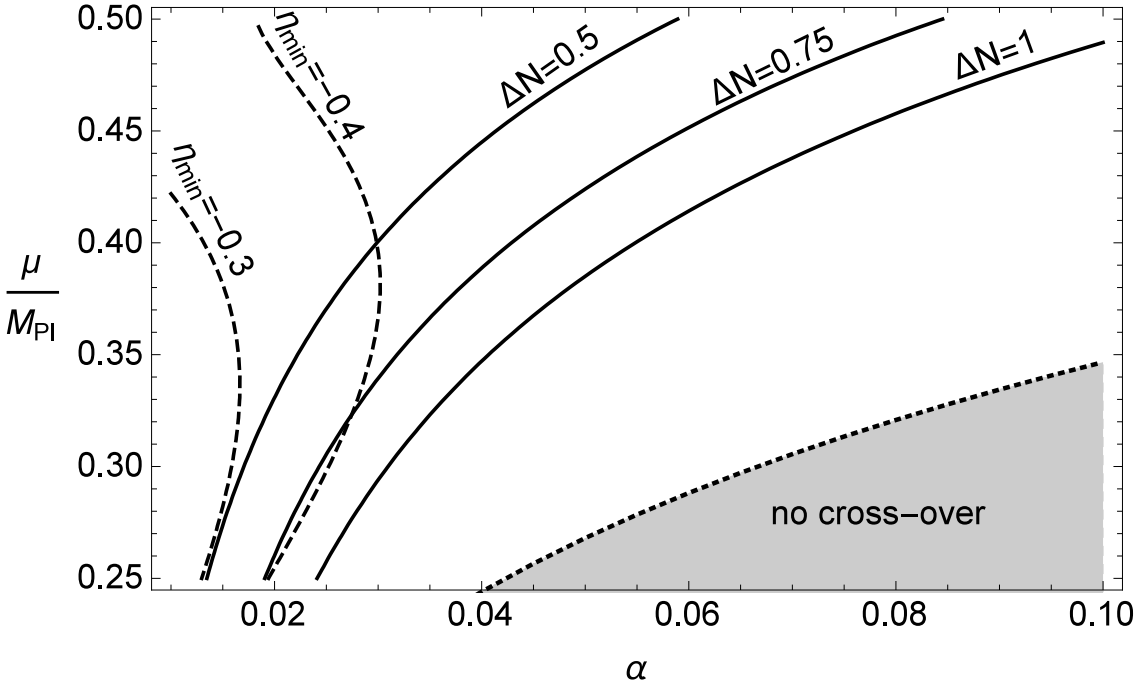


Figure 3.7: A contour plot of $\Delta N$ and $\eta_{\rm min}$ for an inflaton potential of (3.29).

from which

$$\phi_{\rm BH} \simeq 5.0 M_{\rm Pl} \left[1 + 0.56 \log_{10} \left\{1 - 0.049 \log_{10} \left(\frac{M_{\rm BH}}{10^{10} M_\odot}\right)\right\}\right]. \tag{3.34}$$

The condition corresponding to (3.24) is

$$R \equiv \frac{H^4}{V(\phi_{\rm BH}) v(\phi_{\rm BH})} \simeq \frac{M^2}{12\alpha M_{\rm Pl}^2} \exp\left\{\frac{(\phi_{\rm BH} - \phi_0)^2}{2\mu^2}\right\} \left\{1 - \exp\left(-\sqrt{\frac{2}{3}} \frac{\phi_{\rm BH}}{M_{\rm Pl}}\right)\right\}^2 \gg 1. \tag{3.35}$$

Once more, let us rewrite $\exp(\phi_{\rm BH} - \phi_0)^2/2\mu^2 = \exp \nu^2/2$ and solve for $\nu$ to get

$$\nu \simeq 7.1 \left[1 + 0.09 \left\{\log_{10} \left(\frac{R}{100}\right) + \log_{10} \left(\frac{\alpha}{0.01}\right)\right\}\right]^{1/2}. \tag{3.36}$$

A contour plot of $\Delta N$ and $\eta_{\rm min}$ is shown in Fig. 3.7. In this case in the parameter region where $\Delta N \gtrsim 1$, the slow-roll condition is not satisfied well, but it does not mean that the curvature perturbation can not become sufficiently large. It would be safe to conclude that there exists a parameter region where $\Delta N \gtrsim 1$ (see also the footnote †6).

## 3.3 Summary and discussion

We have proposed a new mechanism in which primordial perturbations large enough to produce PBHs are generated while keeping most regions of the universe to be almost homogeneous to the extent that constraints from CMB distortions can be evaded. In

particular, our model can explain SMBHs observed at high redshifts by PBHs. The basic idea is that each patch of the comoving size corresponding to the comoving Hubble horizon at the time of the PBH formation, after causally disconnected, followed either one of the two different inflationary histories yielding different amount of expansion. A history followed by a tiny number of patches has more expansion than the other history followed by most patches. If this difference of expansion, in terms of the number of e-folds, exceeds unity, the minor patches, having experienced more expansion than the major ones, collapse to form PBHs when they reenter the Hubble horizon. Since perturbation is tiny outside the minor patches, nothing special happens there that might lead to phenomena contradicting with observations. In particular, no significant CMB distortion is generated in our mechanism and the upper bound set by COBE/FIRAS measurements can be satisfied.

In our scenario, PBHs of mass $10^{10}M_\odot$, or less considering the growth of these PBHs, are produced at redshifts $z \gtrsim 2 \times 10^7$. Thus, this scenario predicts that SMBHs exist at any redshift range relevant to astrophysical observations. This is a huge difference from any astrophysical scenario in which the number of SMBHs rapidly decreases as the redshift is increased. If future observations continuously discover SMBHs at higher redshifts, then our scenario will be a strong candidate. On the other hand, if SMBHs turn out to be absent at higher redshifts, then our scenario will be disfavored.

There are a few more remarks to be given about our models. In order for the $\chi$-filed to take a positive value at around $\phi_{\rm BH}$ in some patch of $k_{\rm BH}$, larger regions encompassing that patch must have experienced more "kicks" to the positive direction (see Fig.3.4). This indicates that the spatial distribution of PBHs as the seeds of the SMBHs at high redshifts tend to be clustered in our models, which feature may turn out to be inconsistent with observations. One may circumvent this problem by modifying the potential in such a way that the field trajectory is restricted to some constant $\tilde{\chi}$ ($\bar{\chi} < \tilde{\chi} < 0$) for $\phi_{\rm BH} + d\phi < \phi \lesssim \phi_{\rm obs}$, with $d\phi$ chosen sufficiently small to avoid spatial clustering and $\tilde{\chi}$ adjusted to give an appropriate value of $\beta$, as has been done around (3.28). This work should be regarded as an existence proof of phenomenological models which can predict PBHs whose mass is sufficiently large to explain SMBHs of $\sim 10^{10}M_\odot$ at high redshifts, and to this end we have introduced two toy models. The potentials we used may appear somewhat contrived, and it would be more desirable to find simpler and apparently more natural models, which can realize the desired properties discussed here.

# Chapter 4

# Acoustic reheating: a novel probe of primordial power on small scales

Primordial inhomogeneities have been intensively investigated by cosmic microwave background (CMB) [153, 154] or large scale structures of the universe. However, the perturbation scales relevant to these probes are limited to $\mathcal{O}$(Mpc) to $\mathcal{O}$(Gpc) and information of fluctuations on smaller scales is relatively scarce. On the other hand, some models of the early universe predict enhancement of the power spectrum of fluctuations on small scales [57,68,155–166], so investigating small scale perturbations is important. Given this situation, several methods to probe small scale fluctuations have been studied such as primordial black holes (PBHs) [16,17], ultracompact minihalos [23,125,126,167,168], and CMB spectral distortions [121, 169–177]. See Chapter 2 for more details.

In this Chapter, we discuss a novel method to probe perturbations on smaller scales than those probed by CMB spectral distortions ($10^4\mathrm{Mpc}^{-1} < k$). This method is based on a phenomenon we call "acoustic reheating". During the radiation-dominated era, short-wavelength perturbations are damped below diffusion scales (diffusion damping or Silk damping [18,178]), injecting energy into the background universe. Before the $\mu$-era, or the epoch when energy release leads to $\mu$-distortions, any energy injection mostly causes an increase in the average photon temperature, without invoking subtantial spectral distortions [20,179,180]. If this energy injection takes place after the Big Bang Nucleosynthesis (BBN), it increases the number density of photons $n_\gamma$, without changing the number density of baryons $n_\mathrm{b}$, resulting in a decrease in the baryon-photon ratio $\eta \equiv n_\mathrm{b}/n_\gamma$. Since the value of $\eta$ is independently inferred by the abundance of the light elements [41] and CMB observations [42], we can put constraints on the amount of energy injection [181], or primordial perturbation amplitude (see also [182]) in the range of wavenumbers which dissipate after the BBN and before the $\mu-$era.

This Chapter is based on [43]. In §4.1 we calculate the energy injection due to dissipation of perturbations assuming constant power in the range $10^4\mathrm{Mpc}^{-1} < k < 10^5\mathrm{Mpc}^{-1}$, and then provide constraints on that power in §4.2, and conclude in §4.3.

## 4.1 Calculation of energy injection

The basic equations we use can be found in [121]. The total energy release due to the damping of acoustic waves from the redshift $z_2$ to $z_1 (< z_2)$ is given by

$$\frac{\Delta\rho_\gamma}{\rho_\gamma} = \int_{z_1}^{z_2} \frac{1}{a^4\rho_\gamma}\frac{d(a^4 Q_{\rm ac})}{dz} dz, \tag{4.1}$$

with

$$\frac{1}{a^4\rho_\gamma}\frac{d(a^4 Q_{\rm ac})}{dz} \sim 9.4a \int \frac{kdk}{k_{\rm D}^2}\mathcal{P}_\zeta(k) 2\sin^2(kr_{\rm s}) e^{-2k^2/k_{\rm D}^2}, \tag{4.2}$$

where $r_{\rm s} \sim 2.7\times10^5 (1+z)^{-1}$Mpc is the sound horizon and $k_{\rm D} \sim 4.0\times10^{-6}(1+z)^{3/2}$Mpc$^{-1}$ is the damping scale determined by the diffusion of photons.

Let us briefly review how this formula was obtained, following [171]. They use the Newtonian gauge: $ds^2 = a^2 e^{2\phi} dx^2 - e^{2\psi} c^2 dt^2$. Temperature perturbations in different orders are denoted by $\Theta^{(i)} \equiv (\Delta T/T)^{(i)}$, and peculiar velocities by $\boldsymbol{\beta}_p \equiv \mathbf{v}_p/c$. The unit vector representing the direction of photons is denoted by $\hat{\boldsymbol{\gamma}}$. The Legendre transforms of the temperature field are given by $\hat{\Theta}_l = \int \Theta(\mu) P_l(\mu) d\mu/2$, where $P_l(\mu)$ is a Legendre polynomial and $\mu \equiv \hat{\boldsymbol{\gamma}}\cdot\hat{\boldsymbol{\beta}}_p$. Let us assume the photon distribution in every direction $\hat{\boldsymbol{\gamma}}$ at every point $\boldsymbol{x}$ is given by a black body with temperature $T(t,\boldsymbol{x},\hat{\boldsymbol{\gamma}}) = T_{\rm av}(t)[1+\Theta(t,\boldsymbol{x},\hat{\boldsymbol{\gamma}})]$, with the spatial average $\langle T\rangle = T_{\rm av}$. Defining $x_{\rm av} = h\nu/kT_{\rm av}$, for $\Theta \ll 1$ the photon occupation number is expressed as

$$n(t, x_{\rm av}, \boldsymbol{x}, \hat{\boldsymbol{\gamma}}) = (e^{x_{\rm av}/[1+\Theta(t,\boldsymbol{x},\hat{\boldsymbol{\gamma}})]} - 1)^{-1} \simeq n_{\rm Pl}(x_{\rm av}) + \mathcal{G}(x_{\rm av})(\Theta+\Theta^2) + \frac{1}{2}\mathcal{Y}_{\rm SZ}(x_{\rm av})\Theta^2. \tag{4.3}$$

Here, $n_{\rm Pl}(x) = (e^x-1)^{-1}$, $\mathcal{G}(x) \equiv -x\partial_x n_{\rm Pl}(x)$, $\mathcal{Y}(x) \equiv \frac{1}{2}\mathcal{G}(x) x\frac{e^x+1}{e^x-1}$ and $\mathcal{Y}_{\rm SZ} = 2[\mathcal{Y}(x) - 2\mathcal{G}(x)]$. Allowing for the possible spectral distortion of the globally averaged spectrum $\Delta n_{\rm av}$, $n_{\rm av} = n_{\rm Pl} + \Delta n_{\rm av}$. From the second-order Boltzmann equation, with the second-order collision terms for Compton scattering, double Compton scattering and bremsstrahlung (obtained by lengthy calculations there) included, they arrive at $\frac{\partial \Delta n_{\rm av}^{(2)}}{\partial\tau} \ni \langle \mathcal{S}_{\rm ac}\rangle \mathcal{Y}_{\rm SZ}$, with $\dot{\tau} = N_{\rm e}^{(0)}\sigma_{\rm T} c$ denoting the time derivative of the Thomson optical depth and $\mathcal{Y}_{\rm SZ}\mathcal{S}_{\rm ac} \simeq \mathcal{Y}_{\rm SZ}[(3\hat{\Theta}_1 - \beta_p)^2/3 + 9\hat{\Theta}_2^2/2]$. The main source of distortions turned out to be determined by this term in the evolution equation for $\Delta n_{\rm av}^{(2)}$. In the tight coupling limit, we have, in the Fourier space [183], $\beta_p \simeq 3\hat{\Theta}_1/(1 - ikc_s R/\tau')$ and $\hat{\Theta}_2 \simeq 4ik\hat{\Theta}_1/9\tau'$, where $c_s \simeq 1/\sqrt{3(1+R)}$ is the effective sound speed of the photon-baryon fluid, $R = 3\rho_b/4\rho_\gamma$ is the baryon loading and $\tau'$ is the derivative of $\tau$ with respect to the conformal time. Then, the Fourier-transformed source term above becomes

$$\mathcal{S}_{\rm ac} \to \frac{k^2}{\tau'^2}\left[\frac{R^2}{1+R} + \frac{8}{9}\right]|\hat{\Theta}_1|^2 \mathcal{Y}_{\rm SZ}. \tag{4.4}$$

According to [183],

$$|\hat{\Theta}_1|^2 \simeq \frac{\sin^2(kr_s)}{3(1+R)}[3\hat{\Theta}_0(0)]^2 e^{-2k^2/k_D^2} \tag{4.5}$$

and this is related to the power spectrum of the curvature perturbation by [184]

$$[3\hat{\Theta}_0(0)]^2 = P_\zeta(k)/[1 + 4R_\nu/15]^2 \equiv \alpha_\nu P_\zeta(k), \tag{4.6}$$

where $R_\nu = \rho_\nu/(\rho_\gamma + \rho_\nu) \simeq 0.41$. Using $\partial_\eta k_D^{-2} = c_s^2[R^2/(1+R) + 9/8]/(2\tau')$,

$$\langle \mathcal{S}_{\rm ac} \rangle \simeq \frac{\alpha_\nu}{\tau'} \partial_\eta k_D^{-2} \int \frac{d^3k}{(2\pi)^3} k^2 P_\zeta(k) 2\sin^2(kr_s) e^{-2k^2/k_D^2}. \tag{4.7}$$

To obtain the heating rate, this is multiplied by $\tau' \mathcal{Y}_{\rm SZ}$ and integrated over $x^3 dx d^2\hat{\boldsymbol{\gamma}}$, which gives $\partial_\eta Q_{\rm ac}$. Since $\int x^3 \mathcal{Y}_{\rm SZ} dx = 4\rho_\gamma$, $(a^4\rho_\gamma)^{-1} d(a^4 Q_{\rm ac})/dz \equiv -4\dot{\tau} \langle \mathcal{S}_{\rm ac} \rangle / H(1+z)$. In the limit $R \ll 1$,

$$\begin{aligned} \frac{1}{a^4\rho_\gamma} \frac{d(a^4 Q_{\rm ac})}{dz} &\simeq \frac{32\alpha_\nu c}{45\tau' H} \int \frac{dk}{2\pi^2} k^4 P_\zeta(k) 2\sin^2(kr_s) e^{-2k^2/k_D^2} \\ &\simeq 9.4a \int \frac{kdk}{k_D^2} \mathcal{P}_\zeta(k) 2\sin^2(kr_s) e^{-2k^2/k_D^2}, \end{aligned} \tag{4.8}$$

where $\mathcal{P}(k) \equiv k^3 P_\zeta(k)/2\pi^2$.

The largest contributions to the energy release at a redshift $z$ come from the modes around $k \sim k_{\rm D}(z)$ and so we can safely approximate $\sin^2(kr_{\rm s}) \sim 1/2$, since $k_{\rm D}(z) r_{\rm s}(z) \sim (1+z)^{1/2} \gg 1$. Let us consider a top-hat power spectrum: $\mathcal{P}_\zeta(k) = A_\zeta(k_1 < k < k_2), 0$(otherwise), noting that the effects of acoustic reheating are more significant when the width of the enhanced part of the power spectrum is wider. We set $k_1 = 10^4 {\rm Mpc}^{-1}$, since the power spectrum is severely constrained for $k_1 < 10^4 {\rm Mpc}^{-1}$ by $\mu$-distortion [121]. On the other hand, the modes $10^5 {\rm Mpc}^{-1} < k$ dissipate before the neutrino decoupling due to the neutrino diffusion. This is because the comoving wavenumber for the neutrino diffusion becomes $k = 10^5 {\rm Mpc}^{-1}$ at the time of neutrino decoupling, which is close to the horizon scale at that time [185]. Let us briefly revisit the estimation of the horizon scale at the epoch of the neutrino decoupling following [186]. During the epoch when the relativistic particles in equilibrium are photons, electrons, neutrinos and their corresponding anti-particles, the cosmological time in seconds and the temperature in MeV are related by $t_{\rm sec} \simeq 0.74/T_{\rm MeV}^2$. When the time scale of the reactions between the electron neutrinos and the relativistic electron-positron plasma becomes comparable to the cosmological time scale, neutrinos are said to be decoupled. Equivalently, the free-streaming scale of the neutrinos becomes comparable to the horizon at this epoch, and consequently perturbations roughly below the horizon scale at this epoch are washed out. The main reactions to consider are[†1] $e^+ + e^- \leftrightarrow \nu_e + \bar{\nu}_e$, $e^\pm + \nu_e(\bar{\nu}_e) \to e^\pm + \nu_e(\bar{\nu}_e)$. At temperatures under consideration, much lower than the masses of the mediating Z- and W-bosons, the propagators of these reduce to $M_{W,Z}^{-2}$, and the Fermi theory can be used to estimate the cross sections. For relativistic electrons, $\sigma_{\nu e} \simeq \mathcal{O}(1)\alpha_w^2 M_{W,Z}^{-4}(p_1+p_2)^2$, where $\alpha_w \simeq 1/29$ is the weak fine-structure constant and $p_{1,2}$ are the 4-momenta of the colliding particles. Then, the collision time is $t_\nu \simeq (\sigma_{\nu e} n_e)^{-1} \simeq \mathcal{O}(1)\alpha_w^{-2} M_W^4 T^{-5}$, noting $(p_1+p_2)^2 \sim T^2$ and $n_e \sim T^3$. Comparing this and the cosmic time above, the electron neutrinos decouple at(, restoring the Planck mass $m_{\rm Pl} \simeq 10^{19}$Gev,) $T_{\nu_e} \simeq \mathcal{O}(1)\alpha_w^{-2/3}(M_W/m_{Pl})^{1/3} M_W \simeq 1.5$MeV. From this, it turns out that perturbations whose comoving wavenumber $10^5 {\rm Mpc}^{-1} \lesssim k$

[†1]The number densities of $\mu$- and tau-leptons are negligibly small at this epoch, and the only reactions which keep these in thermal contact with the rest of the matter are the elastic scatterings between them and electrons, mediated only by the neutral Z-bosons. The cross sections of these reactions are smaller than those of the reactions between $\nu_e$ and $e^\pm$, and hence $\nu_{\tau,\mu}$ decouple earlier than $\nu_e$.

are washed out at this epoch. Since what can be probed by the consistency between the BBN era and the CMB era (photon decoupling) is only energy injection *after* BBN, taking place shortly after the neutrino decoupling, modes shorter than $k = 10^5$ Mpc$^{-1}$ cannot be constrained and so we set $k_2 = 10^5 \mathrm{Mpc}^{-1}$. Correspondingly, we choose $z_1 = 2 \times 10^6$, the onset of $\mu$-era, and $z_2 = 8.5 \times 10^6$, around when the mode $k = 10^5$ Mpc$^{-1}$ dissipates, assuming it dissipates due to the diffusion of photons.

For the top-hat power spectrum ranging from $k_1$ to $k_2$, the energy release given by Eq. (4.2) becomes

$$\frac{1}{a^4\rho_\gamma}\frac{d(a^4 Q_{\rm ac})}{dz} \sim \frac{2.4A_\zeta}{1+z}\left[\exp\left\{-2\left(\frac{1+z_{*,1}}{1+z}\right)^3\right\} - \exp\left\{-2\left(\frac{1+z_{*,2}}{1+z}\right)^3\right\}\right], \tag{4.9}$$

where $k_* \equiv 4 \times 10^{-6} \mathrm{Mpc}^{-1}$ and

$$z_{*,i} \equiv \left(\frac{k_i}{k_*}\right)^{2/3} (i = 1, 2) \tag{4.10}$$

is the redshift when the mode $k_i$ dissipates. The total energy release then becomes

$$\frac{\Delta\rho_\gamma}{\rho_\gamma} \sim 0.8A_\zeta \left[\mathrm{Ei}\left(-2\left(\frac{1+z_{*,1}}{1+z}\right)^3\right) - \mathrm{Ei}\left(-2\left(\frac{1+z_{*,2}}{1+z}\right)^3\right)\right]_{z_2}^{z_1} \sim 2.3A_\zeta, \tag{4.11}$$

where Ei denotes an exponential integral.

## 4.2 Constraints on $A_\zeta$ obtained by the baryon-photon ratio

The baryon-photon ratio $\eta$ has been determined independently by the abundance of the light elements and the CMB anisotropy, and so the damping should not increase the number of photons too much (or equivalently should not decrease $\eta$ too much) after BBN, from which constraints on $A_\zeta$ can be obtained. To be consistent with observation, we require (noting $n_\gamma \propto T^3, \rho_\gamma \propto T^4$)

$$\frac{\eta_{\rm CMB}}{\eta_{\rm BBN}} = \left(1 - \frac{3}{4}\frac{\Delta\rho_\gamma}{\rho_\gamma}\right) > \frac{\eta_{\rm CMB,obs}}{\eta_{\rm BBN,obs}}, \tag{4.12}$$

where $\eta_{\rm BBN}$ and $\eta_{\rm CMB}$ are the baryon-photon ratios at the time of BBN and after the onset of the $\mu$-era ($\eta$ becomes constant after this moment since we only consider energy injection before the $\mu$-era); the subscript "obs" implies a value determined by observation. Using (4.11), this inequality is rewritten as a constraint on $A_\zeta$:

$$A_\zeta \lesssim 0.6\left(1 - \frac{\eta_{\rm CMB,obs}}{\eta_{\rm BBN,obs}}\right). \tag{4.13}$$

In [41] observations of $^4$He and deuterium were used[†2] to infer the baryon-to-photon ratio $\eta_{10} \equiv 10^{10}(n_b/n_\gamma)_0$, related to the current baryon density parameter by $\Omega_b h^2 = \eta_{10}/273.9$,

[†2] About the use of $^4$He and deuterium, they note the following in [41]:

as well as the effective number of neutrinos $N_{\rm eff}$. The constraints adopted there were, in terms of $y_{\rm DP} \equiv 10^5({\rm D/H})_{\rm P}$ and the $^4$He mass fraction $Y_{\rm P}$, $y_{\rm DP} = 2.60 \pm 0.12$ [187] and $Y_{\rm P} = 0.54 \pm 0.003$ [188]. From these they obtained $\eta_{10} = 6.19 \pm 0.21$ ($\Omega_b h^2 = 0.0226 \pm 0.0008$) and $N_{\rm eff} = 3.56 \pm 0.23$. They adopted Planck constraints, including BAO, of $\Omega_b h^2 = 0.0223 \pm 0.0003$ ($\eta_{10} = 6.11 \pm 0.08$)[†3] and $N_{\rm eff} = 3.30 \pm 0.27$. For $1\sigma$ constraint, we conservatively set $\eta_{\rm CMB,obs} = (6.11 - 0.08) \times 10^{-10}$ and $\eta_{\rm BBN,obs} = (6.19 + 0.21) \times 10^{-10}$ (and $2\sigma$ constraints are considered similarly). Then, the constraint on $A_\zeta$ is

$$A_\zeta \lesssim 0.03(1\sigma), \quad 0.06(2\sigma). \tag{4.14}$$

## 4.3 Discussion

The constraints on the amplitude of the curvature perturbation have also been obtained to avoid overproduction of PBHs to be consistent with observations [12, 110, 111]. If we

> "To account for, or minimize, the post-BBN contributions to the primordial abundances, observations at high redshift (z) and/or low metallicity (Z) are preferred. Deuterium (and hydrogen) is observed in high-z, low-Z, QSO absorption line systems and helium is observed in relatively low-Z, extragalactic H II regions. Even so, it may still be necessary to correct for any post-BBN nucleosynthesis that may have modified their primordial abundances. The post-BBN evolution of D and $^4$He is simple and monotonic. As gas is cycled through stars, D is destroyed and $^4$He produced."

They did not use $^3$He and $^7$Li for the following reasons:

> "In contrast, $^3$He has a more complicated, model dependent, post-BBN evolution and has only been observed in the relatively metal-rich interstellar medium of the Galaxy. $\cdots$. $^7$Li suffers from some of the same issues as $^3$He. Its post-BBN evolution is complicated and model dependent."

In their work also the BBN predicted abundance of $^7$Li, based on the parameter estimations obtained from $^4$He, deuterium and CMB, turns out to be inconsistent with that inferred from observations of $^7$Li, and so the so-called lithium problem still persists.

[†3]The amount of baryons can be well determined by the CMB anisotropy spectrum, due to the sensitive response of the CMB anisotropy spectrum to the change in the amount of the baryons. See e.g. [189] about the details, and we briefly summarize the discussions there. The $m$-th acoustic peak in the anisotropic spectrum of CMB corresponds to the wavenumber satisfying $kr_s = m\pi$. The odd-numbered peaks correspond to the compression phases of the baryon-photon fluid falling into the gravitational potential at the moment of the photon decoupling. When the baryons are more abundant, the sound speed is smaller, and the restoring forces of acoustic oscillations are weaker. This indicates larger compression rate, and so the amplitude of temperature perturbations is larger. On the other hand, the even-numbered peaks are roughly determined by the initial amplitude, without being affected by the baryon loading. Rather, the second peaks becomes smaller due to the effects of the cosmic expansion. Or, more baryons make it difficult for photons to escape from gravitational potential, reducing the amplitude of perturbations corresponding to underdensity [183]. In summary, only the odd-numbered peaks are enhanced with more baryons. Also, smaller amount of the baryons means the smaller sound velocity and sound horizon, and as a result the positions of the acoustic peaks are shifted towards the smaller angular scales. Furthermore, more baryons means more free electrons, which results in a decrease in the mean free path of photons. Then the diffusion damping gets weaker and the diffusion scale is shifted towards smaller scales.

follow [17] (see also [16]), considering the disruption of wide binaries, which is relevant to the scales accessible by acoustic reheating, we obtain a constraint by PBHs as $A_\zeta \lesssim 0.05$.

Although the order of magnitude of these constraints is the same, we may not compare the two directly. This is partly because PBHs are created at high-$\sigma$ peaks, and so possible non-Gaussian distribution may change their abundance in a model dependent manner [57, 155,162]. In particular, when non-Gaussianity is extremely large, it can change constraints to avoid overproduction of PBHs [190, 191].

On the other hand, acoustic reheating considered here is insensitive to the assumption of Gaussianity (as is also pointed out in [121]) and is relatively easy to quantify precisely as well as relate to observations. Furthermore, what is interesting about constraints on the amplitude of primordial fluctuations obtained by acoustic reheating is that they can improve almost in proportion to potential future decrease in error bars associated with the determination of $\eta$.

Though our constraints apply only in a relatively narrow range $10^4\mathrm{Mpc}^{-1} < k < 10^5\mathrm{Mpc}^{-1}$, this technique will have profound implications. For example, if the constraints from acoustic reheating become tighter in future, PBHs in the corresponding comoving horizon mass range $10^3 M_\odot < M < 10^5 M_\odot$ may be severely constrained (note that PBHs bigger than $10^5 M_\odot$ are severely constrained by $\mu$-distortion [39]), unless primordial perturbations are highly non-Gaussian (see Chapter 3). This mass range is particularly interesting in the context of scenarios of PBHs as the seeds of supermassive black holes.

# Chapter 5

# Primordial black holes as a novel probe of primordial short-wavelength gravitational waves

One of the profound implications of primordial inflation [47, 192, 193] (or other alternatives) is the generation of stochastic gravitational wave background (SGWB) [46] on a wide range of scales. SGWB on largest observable scales have been investigated by Planck [42] and BICEP2 [194]. SGWB on smaller scales can be constrained in terms of the value of $N_{\rm eff}$, the effective number of extra degrees of freedom of relativistic species, at the Big Bang Nucleosynthesis (BBN) through the current abundance of light elements [195], or at photon decoupling through the anisotropy of Cosmic Microwave Background (CMB) [196, 197]. (More recently SGWB on small scales has turned out to be constrained by CMB spectral distortions as well [198, 199].) BBN and CMB have played a major role in constraining SGWB since it is applicable on a wide range of scales, noting ground-based laser interferometers tend to target GWs on a relatively limited frequency range with high sensitivity. However, it would be worthwhile to note that upper bounds obtained through $N_{\rm eff}$ needs an assumption about the number of relativistic species in the early universe, as is discussed later. In addition, in obtaining BBN or CMB bounds we implicitly assume that any physical mechanisms, both known and unknown, *increase* $N_{\rm eff}$, making $N_{\rm eff}$ larger than the standard value $N_{\rm eff} = 3.046$ [200]. However, it may also be possible to *decrease* $N_{\rm eff}$ (see e.g. [201–203]). Given these and also given the importance of the issue, it would be desirable to have another independent cosmological method to probe SGWB on a wide range of scales, which does not depend on the assumptions mentioned above, and we propose such a method in this Chapter.

The very physical mechanism we employ to probe SGWB is the formation of primordial black holes (PBHs), black holes formed in the early universe well before the structure formation. There have been a number of mechanisms to create PBHs (see e.g. [12] and references therein), but one of the simple and natural mechanisms is the direct collapse of radiation overdensity during radiation domination, which happens when the density perturbation becomes order unity at the moment of the horizon crossing of the perturbation [15, 77, 204]. (See also [80] for an updated discussion of the formation condition and see also [81–84, 86, 92, 96] for numerical simulation of the formation of PBHs.) There is no conclusive evidence for the existence of PBHs and so upper bounds on the abundance

of PBHs on various mass scales have been obtained by various kinds of observations (see e.g. [12] and references therein). These upper bounds can be translated into those on the power spectrum of the curvature perturbation on small scales [16, 17], namely, they can be used to exclude models of the early universe which predict too many PBHs.

PBHs can also be used to constrain tensor modes generated during inflation, which we discuss in this Chapter for the first time quantitatively in detail. This is because large amplitude tensor perturbations induce scalar perturbations (*induced scalar perturbations*) due to their second-order effects, though tensor and scalar perturbations are decoupled at the linear level. If the typical amplitude of primordial gravitational waves is too large, then the typical amplitude of resultant induced scalar perturbations becomes also too large and there appear too many regions where the amplitude of density perturbation becomes order unity by the moment of their horizon crossing to form PBHs. In short, if the initial amplitude of tensor modes is too large, PBHs are created too abundantly, which situation is inconsistent with observations. In other words, we can obtain upper bounds on the amplitude of initial tensor modes requiring PBHs are not overproduced[†1][†2].

Due to our ignorance of the physics operating in the early universe, new upper limits on tensor perturbations on small scales in themselves would be worthwhile. In addition, it makes our new upper limits still more valuable that there are models of the early universe which can predict large tensor perturbations on small scales. Note that, if a model predicts large tensor perturbations on small scales, and even larger scalar perturbations at the same time, then such a model would be more severely constrained by PBHs generated from first-order scalar perturbations. Here we consider PBH formation only from second-order tensor perturbations, but if scalar perturbations are also large, PBHs are formed more, and so our bounds on tensor perturbations are conservative or model-independent, in the sense that those bounds do not depend on the amplitude of first-order scalar perturbations on small scales. Note also that there are models of the early universe which can predict not only large tensor perturbations on small scales, but also large *tensor-to-scalar ratio* on small scales, and our PBH bounds are particularly useful to constrain these types of models, some of which are briefly described below.

In [222], blue tensor power spectra (i.e. larger power on smaller scales) were obtained in cyclic/ekpyrotic models, with the spectrum of scalar perturbations being kept slightly red (smaller power on smaller scales) to match observations on large scales. The cyclic universe entails the periodic collisions of orbifold planes moving in an extra spatial dimension, which is equivalently described by a scalar field rolling back and forth in an effective

[†1]In several papers, second-order effects of scalar perturbations to induce tensor perturbations (termed induced gravitational waves) have been discussed [205–211]; we can place upper bounds on the amplitude of scalar perturbations (which can be translated into upper bounds on the abundance of PBHs [110,111,212]) from the non-detection of GWs. Our present work is opposite to this direction.

[†2]The direct gravitational collapse of nonlinear localized gravitational waves has been discussed in the literature [213–221] and so one may place upper bounds on tensor modes differently from this work using this direct collapse mechanism. However, the initial condition and dynamics of nonlinear gravitational waves originated from SGWB during the radiation domination have not been fully understood and so in this work we consider the second-order effects of GWs to induce radiation density perturbations, noting the dynamics of nonlinear radiation density perturbations is better understood.

potential. Each cycle consists of an accelerated expansion phase, a slow contraction phase (the ekpyrotic phase), during which the universe is dominated by the kinetic energy as well as negative potential energy of the scalar field and primordial fluctuations are generated, a rapid contraction phase followed by a bounce at which matter and radiation are generated, a phase dominated by the kinetic energy of the scalar field, a radiation dominated, expanding phase, and finally matter and dark energy domination. The spectrum of scalar perturbations can be adjusted to be slightly red by the choice of the scalar field potential during the ekpyrotic phase, and the tensor spectrum turns out to be blue up to the scale corresponding to the end of the ekpyrotic phase. For early universe scenarios where the spectrum of tensor perturbations is strongly blue, probing them on CMB scales may be challenging, while constraints on small-scale components, such as those discussed in this Chapter, may provide useful information. Indeed, they noted that the strongest constraint on the model parameters is obtained from BBN constraints on high-frequency GWs.

If the inflaton violates the Null Energy Condition (NEC, $\rho + p \geq 0$), the Hubble parameter increases during inflation(, called super inflation), and the spectral tilt $n_T$ becomes positive, since $n_T = -2\epsilon \equiv 2\dot{H}/H^2 \propto -(\rho + p)$ [223]. They pointed out that it is possible to violate NEC, without the instability of fluctuations of the inflaton. They introduced a toy model, with the energy density of the NEC-violating inflaton $\rho = \dot{\phi}^2/2 - V_0 e^{-\lambda\phi/M_{\rm pl}}$, which leads to a stage of pole-like inflation, when $a(t) \sim (-t)^p$, $t < 0$, $p = -2/\lambda^2 < 0$. The background and fluctuations are shown to be stable at the classical level. In this model, some mechanism, quantum effects or another field, is necessary to avoid singularity at $t \to 0$ and drive the universe into a radiation dominated epoch.

The spectrum of tensor perturbations generated during super inflation in the framework of Loop Quantum Cosmology (LQC) is calculated in [224]. There a strong blue tile with $n_T \simeq 2$ was obtained, while the form of the inflaton potential to realize a scale-invariant power spectrum of scalar perturbations was also discussed in their previous works. In their scenario, the non-dimensional power spectrum of tensor perturbations on smallest scales is roughly given by the square of the Hubble parameter $H_{\rm e}$ at the end of inflation in units of the Planck scale, and this means $H_{\rm e}$ can be constrained by our PBH constraints discussed in this Chapter. They note that $H_{\rm e}$ is in principle related to the amplitude of scale-invariant curvature perturbations as well, but such a relation has not been obtained yet in the scenarios they consider.

Large tensor perturbations on small scales may also be realized in the framework of the so-called generalized G-inflation ($\rm G^2$-inflation) [225]. This model was the most general non-canonical, non-minimally coupled single-field inflation ever, yielding second-order field equations and containing almost all the previously known single field inflation models in the literature, such as potential-driven slow-roll inflation, k-inflation, new Higgs inflation, $f(R)$ inflation. Non-canonical kinetic terms naturally arise in particle physics models of inflation, and an extra gravitational degree of freedom of modified gravity theories is often equivalently described by a scalar field non-minimally coupled to gravity or matter. The action of $\rm G^2$-inflation contains four generic functions $K, G_3, G_4, G_5$ of $\phi$ and $X = -\partial_\mu\phi\partial^\mu\phi/2$. The quadratic action for the tensor perturbations is

$$S_T^{(2)} = \frac{1}{8}\int dtd^3xa^3\left[\mathcal{G}_T\dot{h}_{ij}^2 - \frac{\mathcal{F}_T}{a^2}(\nabla h_{ij})^2\right], \tag{5.1}$$

$$\mathcal{F}_T \equiv 2\left[G_4 - X(\ddot{\phi}G_{5X} + G_{5\phi})\right], \tag{5.2}$$

$$\mathcal{G}_T \equiv 2\left[G_4 - 2XG_{4X} - X(H\dot{\phi}G_{5X} - G_{5\phi})\right]. \tag{5.3}$$

The squared sound speed is $c_T^2 = \mathcal{F}_T/\mathcal{G}_T$, which is not necessarily unity in general cases. The parameters $\epsilon \equiv -\dot{H}/H^2$, $f_T \equiv \dot{\mathcal{F}}_T/H\mathcal{F}_T$ and $g_T \equiv \dot{\mathcal{G}}_T/H\mathcal{G}_T$ are introduced and they are assumed to be nearly constant. The non-dimensional power spectrum of the tensor perturbations was obtained as

$$\mathcal{P}_T = 8\gamma_T \frac{\mathcal{G}_T^{1/2}}{\mathcal{F}_T^{3/2}} \frac{H^2}{4\pi^2}\bigg|_{-ky_T=1}, \tag{5.4}$$

where

$$\nu_T \equiv \frac{3-\epsilon+g_T}{2-2\epsilon-f_T+g_T}, \quad \gamma_T = 2^{2\nu_T-3}\left|\frac{\Gamma(\nu_T)}{\Gamma(3/2)}\right|^2 \left(1-\epsilon-\frac{f_T}{2}+\frac{g_T}{2}\right), \quad dy_T \equiv \frac{c_T}{a}dt. \tag{5.5}$$

The tensor spectral tilt is given by $n_T = 3-2\nu_T$, and the tensor spectrum is blue ($0 < n_T$) if $4\epsilon + 3f_T - g_T < 0$. Also, if the sound speed becomes temporarily small, the amplitude of tensor perturbations is enhanced on the corresponding scales.

A slightly red spectrum of the curvature perturbation, while keeping the gravitational spectrum strongly blue-tilted, was also shown to be realized during a stringy thermal contracting phase at temperatures beyond the so-called Hagedorn temperature (the Hagedorn phase) in [226], assuming a non-singular bounce. In that scenario, primordial curvature perturbations originate from statistical thermal fluctuations, not by scalar field quantum fluctuations.

Scalar and tensor perturbations in large field chaotic models with non-Bunch-Davies (non-BD) initial states were analyzed in [227], and it was shown that in that model also gravitational waves can be blue while maintaining slightly red scalar perturbations. Normally, initial states for perturbations are chosen to be Bunch-Davies (BD) vacuum states, namely, perturbation modes on sub-Hubble scales effectively propagate in vacuum states associated with flat space. Non-BD initial states were characterized by the Bogoliubov coefficients for each $k$ mode and for both scalar and tensor perturbations, which were denoted by $\alpha_k^S, \beta_k^S, \alpha_k^T, \beta_k^T$, with $(\alpha_k^{S,T}, \beta_k^{S,T}) = (1, 0)$ corresponding to the standard BD initial states. These parameters are determined by unknown high energy physics, and depending on the choice of the above parameters, blue gravitational waves were obtained while maintaining the scalar perturbations slightly red.

Blue gravity waves with slightly red scalar perturbations were also obtained without violating NEC by breaking the spatial diffeomorphism, usually imposed on the dynamics of perturbation, in the context of effective theory of inflation [228, 229]. There, breaking of spatial diffeomorphism was considered by effective quadratic mass terms or derivative operators for metric fluctuations in the Lagrangian during inflation without the necessity for specifying the UV completion, while noting that it may be a version of massive gravity coupled to an inflaton, some model of inflation using vectors, or sets of scalars obeying some symmetries.

This Chapter is based on [44, 45], and is organized as follows; In section §5.1 simple estimations of PBH upper bounds on tensor perturbations are provided; The radiation

density perturbation generated from tensor perturbations is calculated in §5.2; Section §5.3 is dedicated to the discussion of upper bounds on tensor modes from PBHs along with the comparison of them with those obtained from exiting methods such as BBN, CMB, ground-based laser interferometers and pulsar timing arrays; Finally we conclude in §5.4.

## 5.1 Simple physical arguments of PBH upper bounds on tensor perturbations

For simplicity we assume the typical amplitude of tensor fluctuations of only a limited range of wavelength around $\lambda_p$ (say, in the range $(e^{-1/2}\lambda_p, e^{1/2}\lambda_p)$) is particularly large, namely we consider a peak in the power spectrum around $\lambda_p$. Let us denote by $\sigma_h$ the root-mean-square amplitude (RMS) or the typical amplitude of tensor fluctuations when the relevant modes under consideration are on super-horizon scales. Note that $\sigma_h^2$ roughly corresponds to the dimensionless power spectrum $\mathcal{P}_h$ of primordial GWs. Suppose these large amplitude tensor perturbations whose wavelength is around $\lambda_p$ reenter the horizon during the radiation-dominated era. Then it generates radiation density perturbations $\delta_r$ whose wavelength is around $\lambda_p$ and whose RMS $\sigma_{\delta_r}$ at around the horizon crossing is roughly given by $\sigma_{\delta_r} \sim \sigma_h^2$, simply because $\delta_r$ is generated by second-order GWs. As confirmed later, this relation indeed holds well at least for the delta-function power spectrum. If $\delta_r > \delta_{r,\mathrm{th}} \sim 0.4$ [80], the induced radiation density perturbations collapse to form PBHs. The probability of formation of PBHs has to be extremely small to be consistent with various observations [12]. Therefore, in order not to overproduce PBHs, one may require (see (2.8)) $\mathcal{P}_h \sim \sigma_h^2 \sim \sigma_{\delta_r} \lesssim 0.1\delta_{r,\mathrm{th}} \sim 0.04$. This upper bound is applicable on all the scales which reenter the horizon during the radiation-dominated era. Furthermore, this bound is probably conservative on scales which reenter the horizon during the (early as well as late) matter-dominated era, since formation of black holes by direct collapse of primordial perturbations is easier when the universe is (literally or effectively) dominated by pressureless dust[†3]. To summarize, we have

$$\mathcal{P}_h \lesssim 0.04 \quad \text{(PBH)}, \tag{5.6}$$

and this is applicable from the comoving wavelength of $\sim$ 1Gpc all the way down to $\sim$ 1Gpc $\times\, e^{-60} \sim$ 0.3m, assuming the total number of e-folds during inflation is sixty[†4]. This is consistent with upper bounds obtained by more rigorous calculations later. See Discussion for some comments regarding the constraints on smallest scales.

[†3]Note that PBH formation due to second-order GWs during a dust-dominated universe cannot be completely regarded as collapse of dust in a dust-dominated universe, since locally the energy density of GWs is sizable, and so the effective equation of state there would be positive.

[†4]The idea of using PBHs to constrain tensor fluctuations itself is so simple and indeed it does not seem to be new. For example, we found in [230] PBH constraints are briefly mentioned. There they require $\mathcal{P}_h \lesssim 1$, which is probably too conservative to ensure the sufficient rareness of formation of PBHs to be consistent with observations (see eq.(5.6) and the preceding arguments). We discuss PBH constraints on tensor fluctuations in detail, quantitatively in [44] and an accompanying paper [45] for the first time.

## 5.2 The radiation density perturbation generated from tensor perturbations

Perturbations to the metric and energy momentum tensor are written as (see [231] for more details)

$$ds^2 = a^2[-(1+2\Phi)d\eta^2 + 2B_{,i}d\eta dx^i + \{(1-2\Psi)\delta_{ij} - 2E_{,ij} + 2h_{ij}\}\, dx^i dx^j], \tag{5.7}$$

$$T_{\mu\nu} = (p+\delta p)g_{\mu\nu} + (\rho + \delta\rho + p + \delta p)(u_\mu + \delta u_\mu)(u_\nu + \delta u_\nu), \tag{5.8}$$

and the spatial components of the velocity perturbation $\delta u_\mu$ are written as $\delta u_i = \delta u_{,i}$. Let us consider a coordinate transformation of the form $x^\mu \to x^\mu + \epsilon^\mu(x^\mu)$, with $\epsilon_0 = -\epsilon^0$, $\epsilon_i = a^2\epsilon^i$, $\epsilon_i = \epsilon_{,i}$. Then $E$ and $\delta u$ at each spacetime point can be thought of effectively transforming as $E \to E + \epsilon$, $\delta u \to \delta u - \epsilon_0$ (gauge transformation). Here we choose $\epsilon$ so that $E = 0$, and then choose $\epsilon_0$ so that $\delta u = 0$. Both choices are unique, so that there is no freedom to make gauge transformations, and this choice is called the comoving gauge. Then the metric is written as

$$ds^2 = a^2[-(1+2\Phi)d\eta^2 + 2B_{,i}d\eta dx^i + ((1-2\Psi)\delta_{ij} + 2h_{ij})dx^i dx^j]. \tag{5.9}$$

Here a few comments are in order. In calculations of this Chapter it is assumed that the amplitude of initial tensor perturbations is much larger than that of scalar perturbations (schematically, (scalar) $\ll$ (tensor)) and so the scalar quantities in the metric above should be regarded as second-order in $h_{ij}$. Hence, for scalar perturbations we write down the Einstein equations keeping second-order terms only in $h_{ij}$. Importantly, our PBH upper bounds on tensor perturbations thus obtained are applicable even if this initial hierarchy between tensor and scalar perturbations is not realized. This is because if the amplitude of scalar perturbations is as larger as, or larger than that of tensor perturbations, then the abundance of PBHs increases when the amplitude of tensor modes is fixed. That is, assuming (scalar) $\ll$ (tensor) initially is most conservative in placing upper bounds on tensor modes and hence our bounds are applicable even if that assumption does not hold.

Let us write down the fundamental equations in the following. We denote the energy density and pressure of dominating radiation by $\rho$ and $p$ respectively, and write $p = c_{\rm s}^2\rho$, where $c_{\rm s}$ is the speed of sound. In this Chapter we restrict our attention to the formation of PBHs due to collapse of the radiation density perturbation during radiation domination and so we set $c_{\rm s} = 1/\sqrt{3}$ in calculations, though we leave $c_{\rm s}$ unspecified in equations below for generality. We decompose $\rho$ and $p$ as $\rho(\eta, \boldsymbol{x}) = \rho_0(\eta) + \delta\rho(\eta, \boldsymbol{x})$ and $p(\eta, \boldsymbol{x}) = p_0(\eta) + \delta p(\eta, \boldsymbol{x})$.

The zeroth-order Einstein equations yield

$$\mathcal{H}^2 = \frac{8\pi G}{3}a^2\rho_0, \tag{5.10}$$

$$\mathcal{H}^2 - \mathcal{H}' = 4\pi G a^2(\rho_0 + p_0), \tag{5.11}$$

where $\mathcal{H} \equiv a'/a$ with a prime denoting differentiation with respect to the conformal time $\eta$. These two equations are combined to give

$$2\mathcal{H}' + (1+3c_{\rm s}^2)\mathcal{H}^2 = 0. \tag{5.12}$$

The Einstein equations at first-order gives the standard evolution equation for tensor modes as follows;

$$h''_{ij} + 2\mathcal{H}h'_{ij} - \Delta h_{ij} = 0. \tag{5.13}$$

The Einstein equations at second-order, derived in the Appendix D, are as follows:

$$\Delta\Psi - 3\mathcal{H}(\Psi' + \mathcal{H}\Phi) - \mathcal{H}\Delta B + S_1 = 4\pi G a^2 \delta\rho, \tag{5.14}$$

$$(\Psi' + \mathcal{H}\Phi + S_2)_{,i} = 0, \tag{5.15}$$

$$\Psi'' + \mathcal{H}(2\Psi + \Phi)' + (2\mathcal{H}' + \mathcal{H}^2)\Phi + \frac{1}{2}\Delta(\Phi - \Psi + B' + 2\mathcal{H}B) + S_3 + S_4 = 4\pi G a^2 \delta p, \tag{5.16}$$

$$(\Phi - \Psi + B' + 2\mathcal{H}B - 2S_5)_{,ij} = 0. \tag{5.17}$$

Here, the following terms, second order in $h_{ij}$, source the scalar perturbations:

$$S_1 \equiv -\frac{1}{4}h'_{ij}h^{ij\prime} - 2\mathcal{H}h_{ij}h^{ij\prime} + h_{ij}\Delta h^{ij} - \frac{1}{2}\partial_j h_{ik}\partial^k h^{ij} + \frac{3}{4}\partial_k h_{ij}\partial^k h^{ij}, \tag{5.18}$$

$$\Delta S_2 = \partial^i S_i, \tag{5.19}$$

$$S_i = -h^{jk}\partial_k h'_{ij} + \frac{1}{2}h^{jk\prime}\partial_i h_{jk} + h^{jk}\partial_i h'_{jk}, \tag{5.20}$$

$$S_3 \equiv \frac{3}{4}h'_{ij}h^{ij\prime} + h_{ij}h^{ij\prime\prime} + 2\mathcal{H}h_{ij}h^{ij\prime} - h_{ij}\Delta h^{ij} + \frac{1}{2}\partial_j h_{ik}\partial^k h^{ij} - \frac{3}{4}\partial_k h_{ij}\partial^k h^{ij}, \tag{5.21}$$

$$\Delta S_4 = \frac{1}{2}(\Delta S^i{}_i - \partial^i\partial^j S_{ij}), \tag{5.22}$$

$$\Delta^2 S_5 = \frac{1}{2}(3\partial^i\partial^j S_{ij} - \Delta S^i_i), \tag{5.23}$$

$$\begin{aligned} S_{ij} \equiv {} & -h_i{}^{k\prime}h'_{jk} - h_{ik}h_j{}^{k\prime\prime} - 2\mathcal{H}h_i{}^k h'_{jk} + h^{kl}\partial_k\partial_l h_{ij} + h_i{}^k\Delta h_{jk} - h^{kl}\partial_l\partial_i h_{jk} - h^{kl}\partial_l\partial_j h_{ik} \\ & -\partial_k h_{jl}\partial^l h_i{}^k + \partial_l h_{jk}\partial^l h_i{}^k + \frac{1}{2}\partial_i h_{kl}\partial_j h^{kl} + h^{kl}\partial_i\partial_j h_{kl}. \end{aligned} \tag{5.24}$$

Using (5.13), these source terms are rewritten as follows:

$$S_1 = -\frac{1}{4}h'_{ij}h^{ij\prime} + h_{ij}h^{ij\prime\prime} - \frac{1}{2}\partial_j h_{ik}\partial^k h^{ij} + \frac{3}{4}\partial_k h_{ij}\partial^k h^{ij}, \tag{5.25}$$

$$S_3 = \frac{3}{4}h'_{ij}h^{ij\prime} + \frac{1}{2}\partial_j h_{ik}\partial^k h^{ij} - \frac{3}{4}\partial_k h_{ij}\partial^k h^{ij}, \tag{5.26}$$

$$\begin{aligned} S_{ij} = {} & -h_i{}^{k\prime}h'_{jk} + h^{kl}\partial_k\partial_l h_{ij} - h^{kl}\partial_l\partial_i h_{jk} - h^{kl}\partial_l\partial_j h_{ik} \\ & -\partial_k h_{jl}\partial^l h_i{}^k + \partial_l h_{jk}\partial^l h_i{}^k + \frac{1}{2}\partial_i h_{kl}\partial_j h^{kl} + h^{kl}\partial_i\partial_j h_{kl}. \end{aligned} \tag{5.27}$$

The conservation of the energy-momentum tensor yields

$$\delta\rho' + 3\mathcal{H}(\delta\rho + \delta p) - (\rho + p)\Delta B - 3(\rho + p)\Psi' - 2(\rho + p)h^{ij}h'_{ij} = 0, \tag{5.28}$$

$$\partial_i(\delta p + (\rho + p)\Phi) = 0. \tag{5.29}$$

One can derive an evolution equation of $\Psi$ as follows. First, eqs.(5.28) and (5.29) lead to (hereafter we work in Fourier space)

$$\Phi' = -c_s^2 \left(-k^2 B + 3\Psi' + 2h^{ij}h'_{ij}\right). \tag{5.30}$$

The term $-k^2 B$ of the above can be eliminated by the following relation, obtained from eqs.(5.14) and (5.15):

$$-k^2 B = \frac{-k^2\Psi}{\mathcal{H}} + 3S_2 + \frac{S_1}{\mathcal{H}} - \frac{3}{2}\mathcal{H}\delta_r, \tag{5.31}$$

where $\delta_r \equiv \delta\rho/\rho_0$. Using these and (5.17) as well as (5.12), (5.16) can be rewritten as

$$\Psi'' + 2\mathcal{H}\Psi' + c_{\rm s}^2 k^2 \Psi = S, \tag{5.32}$$

where

$$S \equiv c_{\rm s}^2 S_1 - S_3 - \hat{k}^i\hat{k}^j S_{ij} + 2c_{\rm s}^2\mathcal{H}h^{ij}h'_{ij}. \tag{5.33}$$

From (5.15) and (5.29), the energy density perturbation is given by

$$\delta_r = \frac{1 + c_{\rm s}^2}{c_2^2\mathcal{H}}(\Psi' + S_2). \tag{5.34}$$

Eq.(5.32) can be formally solved as

$$\Psi(\eta, \boldsymbol{k}) = a^{-1}(\eta)\int_0^\eta d\tilde{\eta} g_k(\eta, \tilde{\eta}) a(\tilde{\eta}) S(\tilde{\eta}, \boldsymbol{k}), \tag{5.35}$$

where $g_k$ is the Green's function satisfying

$$g_k'' + \left(c_{\rm s}^2 k^2 - \frac{a''}{a}\right) g_k = \delta(\eta - \tilde{\eta}), \tag{5.36}$$

which can be constructed by the two homogeneous solutions

$$v_1(k, \eta) = \sin(c_{\rm s} k\eta), \quad v_2(k, \eta) = \cos(c_{\rm s} k\eta) \tag{5.37}$$

as follows [209]:

$$g_k(\eta, \tilde{\eta}) = \frac{v_1(k,\eta)v_2(k,\tilde{\eta}) - v_1(k,\tilde{\eta})v_2(k,\eta)}{v_1'(k,\tilde{\eta})v_2(k,\tilde{\eta}) - v_1(k,\tilde{\eta})v_2'(k,\tilde{\eta})} = \frac{1}{c_{\rm s}k}\sin\left(c_{\rm s}k(\eta - \tilde{\eta})\right). \tag{5.38}$$

The two point correlation function of $\Psi$ can be expressed as

$$\begin{aligned}\langle\Psi(\eta, \boldsymbol{k})\Psi^*(\eta, \boldsymbol{K})\rangle &= \frac{2\pi^2}{k^3}\delta(\boldsymbol{k} - \boldsymbol{K})\mathcal{P}_\Psi(k) \\ &= a^{-2}(\eta)\int_0^\eta d\eta_1 \int_0^\eta d\eta_2 g_k(\eta, \eta_1) g_K(\eta, \eta_2) a(\eta_1) a(\eta_2) \langle S(\eta_1, \boldsymbol{k}) S(\eta_2, \boldsymbol{K})\rangle.\end{aligned} \tag{5.39}$$

In the following, let us write down the Fourier components of the source (5.33). First let us decompose $h_{ij}(\eta, \boldsymbol{x})$ as follows (following [111]):

$$h_{ij}(\eta, \boldsymbol{x}) = \int \frac{d^3\boldsymbol{k}}{(2\pi)^{3/2}} e^{i\boldsymbol{k}\cdot\boldsymbol{x}} (h^+(\eta, \boldsymbol{k}) e^+_{ij}(\boldsymbol{k}) + h^\times(\eta, \boldsymbol{k}) e^\times_{ij}(\boldsymbol{k})), \tag{5.40}$$

where for $\boldsymbol{k}$ in the $z$-direction

$$e^+_{11}(\hat{z}) = -e^+_{22}(\hat{z}) = e^\times_{12}(\hat{z}) = e^\times_{21}(\hat{z}) = 1, \quad \text{others} = 0 \tag{5.41}$$

while for $\hat{k}$ in any other direction $e^r_{ij}(\hat{k})(r = +, \times)$ is defined by applying on each of the indices $i$ and $j$ a standard rotation, that takes the $z$-direction into the direction of $\hat{k}$ (see e.g. [231]). Then one can check the following:

$$\sum_{ij} e^r_{ij}(\boldsymbol{k}) e^s_{ij}(\boldsymbol{k}) = 2\delta^{rs}. \tag{5.42}$$

Let us further decompose Fourier components as $h^r(\eta, \boldsymbol{k}) = D(\eta, k) h^r(\boldsymbol{k})$, where $h^r(\boldsymbol{k})$ is the initial amplitude and $D(\eta, k)$ is the growth factor, which can be obtained by solving the linear evolution equation (5.13) for $h_{ij}$:

$$D(\eta, k) = \frac{\sin k\eta}{k\eta}. \tag{5.43}$$

It turns out that the source can be written as follows (see the Appendix E):

$$S(\eta, \boldsymbol{k}) = \sum_{rs} \int \frac{d^3\boldsymbol{k}'}{(2\pi)^{3/2}} h^r(\boldsymbol{k}') h^s(\boldsymbol{k} - \boldsymbol{k}') A_{rs}(\eta, \boldsymbol{k}, \boldsymbol{k}'), \tag{5.44}$$

$$A_{rs}(\eta, \boldsymbol{k}, \boldsymbol{k}') \equiv f_1(\eta, \boldsymbol{k}, \boldsymbol{k}') E^{rs}_1(\boldsymbol{k}, \boldsymbol{k}') + f_2(\eta, \boldsymbol{k}, \boldsymbol{k}') E^{rs}_2(\boldsymbol{k}, \boldsymbol{k}'), \tag{5.45}$$

where

$$E^{ij}_{rs\,kl}(\boldsymbol{k}, \boldsymbol{k}') \equiv e^{ij}_r(\boldsymbol{k}') e^s_{kl}(\boldsymbol{k} - \boldsymbol{k}'), \tag{5.46}$$

$$E^{rs}_1(\boldsymbol{k}, \boldsymbol{k}') \equiv \hat{k}_j \hat{k}^k E^{rs\ ij}_{ik}(\boldsymbol{k}, \boldsymbol{k}'), \quad E^{rs}_2(\boldsymbol{k}, \boldsymbol{k}') \equiv E^{ij}_{rs\ ij}(\boldsymbol{k}, \boldsymbol{k}'), \tag{5.47}$$

whose components are written by

$$E^{++}_1(\boldsymbol{k}, \boldsymbol{k}') = -\mu_1 \sqrt{1 - \mu^2} \sqrt{1 - \mu_2^2}, \tag{5.48}$$

$$E^{\times\times}_1(\boldsymbol{k}, \boldsymbol{k}') = -\sqrt{1 - \mu^2} \sqrt{1 - \mu_2^2}, \tag{5.49}$$

$$E^{++}_2(\boldsymbol{k}, \boldsymbol{k}') = 1 + \mu_1^2, \tag{5.50}$$

$$E^{\times\times}_2(\boldsymbol{k}, \boldsymbol{k}') = 2\mu_1, \tag{5.51}$$

$$\mu \equiv \boldsymbol{k} \cdot \boldsymbol{k}' / k\, k', \tag{5.52}$$

$$\mu_1 \equiv \frac{\boldsymbol{k}' \cdot (\boldsymbol{k} - \boldsymbol{k}')}{k' |\boldsymbol{k} - \boldsymbol{k}'|} = \frac{k\mu - k'}{|\boldsymbol{k} - \boldsymbol{k}'|}, \tag{5.53}$$

$$\mu_2 \equiv \frac{\boldsymbol{k} \cdot (\boldsymbol{k} - \boldsymbol{k}')}{k |\boldsymbol{k} - \boldsymbol{k}'|} = \frac{k - k'\mu}{|\boldsymbol{k} - \boldsymbol{k}'|}, \tag{5.54}$$

with other components shown to vanish[†5].

The definitions of $f_1$ and $f_2$ should be read off from eq.(E.9) as follows;

$$f_1(\eta,\boldsymbol{k},\boldsymbol{k}') = D(\eta,k')\left\{\overleftarrow{\partial_\eta}\partial_\eta - \frac{1}{2}(3-c_{\rm s}^2)k^2 + 3kk'\mu - k'^2\right\}D(\eta,|\boldsymbol{k}-\boldsymbol{k}'|), \tag{5.55}$$

$$\begin{aligned} f_2(\eta,\boldsymbol{k},\boldsymbol{k}') = D(\eta,k')\Bigg\{&-\frac{1}{4}(3+c_{\rm s}^2)\overleftarrow{\partial_\eta}\partial_\eta + c_{\rm s}^2\partial_\eta^2 + 2c_{\rm s}^2\mathcal{H}\partial_\eta + \frac{1}{8}(1-3c_{\rm s}^2)k^2 \\ &-\frac{1}{2}k'\mu(k-k'\mu) + \frac{3}{4}(1+c_{\rm s}^2)k'^2\Bigg\}D(\eta,|\boldsymbol{k}-\boldsymbol{k}'|), \end{aligned} \tag{5.56}$$

where $\overleftarrow{\partial_\eta}$ is supposed to differentiate *only* $D(\eta,k')$ on the left.

Introducing the power spectrum of tensor perturbations as

$$\langle h^r(\boldsymbol{k})h^{s*}(\boldsymbol{K})\rangle = \frac{2\pi^2}{k^3}\delta(\boldsymbol{k}-\boldsymbol{K})\delta_{rs}\mathcal{P}_h(k) \tag{5.57}$$

and assuming $h^r(\boldsymbol{k})$ is Gaussian, we can obtain the following expression for the correlation of the source:

$$\langle S(\eta_1,\boldsymbol{k})S(\eta_2,\boldsymbol{K})\rangle = \pi\delta(\boldsymbol{k}+\boldsymbol{K})\sum_{rs}\int d^3\boldsymbol{k}'\frac{\mathcal{P}_h(k')\mathcal{P}_h(|\boldsymbol{k}-\boldsymbol{k}'|)}{k'^3|\boldsymbol{k}-\boldsymbol{k}'|^3}A_{rs}(\eta_1,\boldsymbol{k},\boldsymbol{k}')A_{rs}(\eta_2,\boldsymbol{k},\boldsymbol{k}'). \tag{5.58}$$

In this work, we assume the following delta function tensor-mode power spectrum:

$$\mathcal{P}_h(k) = \mathcal{A}^2 k\delta(k-k_p). \tag{5.59}$$

From (5.34) and (5.35), the energy density perturbation can be calculated as

$$\delta_r(\eta,\boldsymbol{k}) = \frac{1+c_{\rm s}^2}{c_{\rm s}^2\mathcal{H}}\sum_{rs}\int\frac{d^3\boldsymbol{k}'}{(2\pi)^{3/2}}h^r(\boldsymbol{k}')h^s(\boldsymbol{k}-\boldsymbol{k}')F_{rs}(\eta,\boldsymbol{k},\boldsymbol{k}'), \tag{5.60}$$

where

$$\begin{aligned} F_{rs}(\eta,\boldsymbol{k},\boldsymbol{k}') \equiv &\int d\tilde{\eta}(\tilde{\eta}/\eta)A_{rs}(\tilde{\eta},\boldsymbol{k},\boldsymbol{k}')(\partial_\eta-\mathcal{H})g_k(\eta,\tilde{\eta}) \\ &+ D(\eta,k')\left\{-\partial_\eta E_1^{rs} + \left(\frac{1}{2}\overleftarrow{\partial_\eta}+\partial_\eta\right)\left(1-\frac{k'}{k}\mu\right)E_2^{rs}\right\}D(\eta,|\boldsymbol{k}-\boldsymbol{k}'|). \end{aligned} \tag{5.61}$$

The power spectrum is defined by

$$\langle\delta_r(\eta,\boldsymbol{k})\delta_r^*(\eta,\boldsymbol{K})\rangle_{\rm C} \equiv \langle\delta_r(\eta,\boldsymbol{k})\delta_r^*(\eta,\boldsymbol{K})\rangle - \langle\delta_r(\eta,\boldsymbol{k})\rangle\langle\delta_r^*(\eta,\boldsymbol{K})\rangle = \frac{2\pi^2}{k^3}\delta(\boldsymbol{k}-\boldsymbol{K})\mathcal{P}_{\delta_r}(\eta,k) \tag{5.62}$$

[†5]These expressions are obtained by first setting $\hat{k}=\hat{z}$, which is possible due to isotropy, and by assuming $\hat{k'}$ is on the $x-y$ plane, which is justified by the rotational invariance of $E_1^{rs}$ and $E_2^{rs}$.

and calculated as follows:

$$\mathcal{P}_{\delta_r}(\eta, k) = \left(\frac{1+c_{\rm s}^2}{c_{\rm s}^2}\right)^2 \mathcal{A}^4 \left(\frac{k}{k_p}\right)^2 \eta^2 \Theta\left(1-\frac{k}{2k_p}\right) \sum_{rs} F_{rs}\left(\eta, k, k_p, \frac{k}{2k_p}\right)^2 . \tag{5.63}$$

The time evolutions of the power spectrum for a few modes are shown in Fig.5.1, where $\mathcal{A} = 1$. The power spectrum takes the maximum value shortly after the horizon crossing of each mode. After reaching the maximum, it starts oscillation with the amplitude almost constant, similarly to the behavior in the standard linear cosmological perturbation theory. This is because the first order tensor perturbations decay after the horizon crossing, and so do the source terms, leading to the reduction of our fundamental equations to the standard ones in the linear theory.

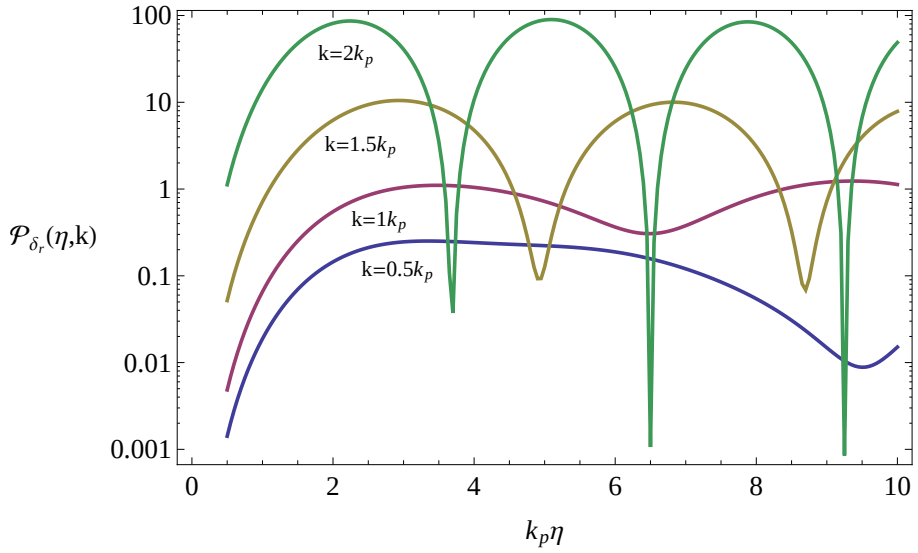


Figure 5.1: The time evolution of the power spectrum for each mode.

## 5.3 PBH upper bound on SGWB

In order to place upper bounds on tensor-modes from PBHs, the abundance of PBHs needs to be calculated, which is obtained by integrating the high-$\sigma$ tail of the probability density function (PDF) of the density perturbation averaged over the horizon scale. In the following we estimate the moment when the PBH formation is most efficient for each position of the spike specified by $k_p$, by calculating the dispersion of the density perturbation, and then present the PDF at this moment to calculate the abundance of PBHs and place upper bounds on tensor perturbations.

First it is important to note that the average $\langle \delta_r(\eta, \boldsymbol{x}) \rangle$ is non-zero, since the density perturbation is generated by the second-order effects of tensor modes, and so let us evaluate it in the following. First we introduce $f_3$ and $f_4$ by rewriting $F_{rs}$ as

$$F_{rs}(\eta, \boldsymbol{k}, \boldsymbol{k}') = f_3(\eta, \boldsymbol{k}, \boldsymbol{k}') E_1^{rs} + f_4(\eta, \boldsymbol{k}, \boldsymbol{k}') E_2^{rs}. \tag{5.64}$$

The explicit forms of $f_3$ and $f_4$ can be obtained by using (5.45), though the integration over $\eta$ can not be done analytically for general $\boldsymbol{k}$:

$$f_3(\eta,\boldsymbol{k},\boldsymbol{k}') = \int d\tilde{\eta}(\tilde{\eta}/\eta) f_1(\tilde{\eta},\boldsymbol{k},\boldsymbol{k}')(\partial_\eta - \mathcal{H}) g_k(\eta,\tilde{\eta}) - D(\eta,k')\partial_\eta D(\eta,|\boldsymbol{k}-\boldsymbol{k}'|), \quad (5.65)$$

$$f_4(\eta,\boldsymbol{k},\boldsymbol{k}') = \int d\tilde{\eta}(\tilde{\eta}/\eta) f_2(\tilde{\eta},\boldsymbol{k},\boldsymbol{k}')(\partial_\eta - \mathcal{H}) g_k(\eta,\tilde{\eta}) + D(\eta,k')\left(\frac{1}{2}\overleftarrow{\partial_\eta} + \partial_\eta\right)\left(1 - \frac{k'}{k}\mu\right) D(\eta,|\boldsymbol{k}-\boldsymbol{k}'|). \quad (5.66)$$

Noting only the zero-mode $\delta_r(\eta,\boldsymbol{k}=\boldsymbol{0})$ contributes to $\langle\delta_r(\eta,\boldsymbol{x})\rangle$, we need $f_3$ and $f_4$ in $\boldsymbol{k}\to\boldsymbol{0}$ limit, which are, assuming the delta-function power spectrum,

$$f_3 = 0, \quad f_4 = -\frac{-1+2k_p^2\eta^2+\cos(2k_p\eta)}{24k_p^2\eta^3}. \quad (5.67)$$

Hence,

$$\begin{aligned}
&\langle\delta_r(\eta,\boldsymbol{x}=\boldsymbol{0})\rangle \\
&= \int \frac{d\boldsymbol{k}^3}{(2\pi)^{3/2}}\frac{1+c_{\rm s}^2}{c_{\rm s}^2\mathcal{H}}\int\frac{d^3\boldsymbol{k}'}{(2\pi)^{3/2}}\frac{2\pi^2}{k_p^3}\delta(\boldsymbol{k})\mathcal{A}^2 k_p\delta(k'-k_p) f_4(\eta,\boldsymbol{k}=\boldsymbol{0},\boldsymbol{k}')\times(2-(-2)) \\
&= -\frac{(1+c_{\rm s}^2)\mathcal{A}^2}{6c_{\rm s}^2k_p^2\eta^2}\{-1+2k_p^2\eta^2+\cos(2k_p\eta)\}. \quad (5.68)
\end{aligned}$$

When $k_p\eta \gg 1$, the time average of this asymptotes to

$$\langle\delta_r\rangle = -\frac{(1+c_{\rm s}^2)}{3c_{\rm s}^2}\mathcal{A}^2, \quad (5.69)$$

while $\langle\delta_r\rangle \to 0$ for $k_p\eta\to 0$. We denote the density perturbation averaged over a sphere with comoving radius $R$ by $\delta_r(\eta,\boldsymbol{x},R)$, the dispersion of which is related to the power spectrum as follows:

$$\sigma(\eta,R) \equiv (\langle\delta_r(\eta,\boldsymbol{x},R)^2\rangle - \langle\delta_r(\eta,\boldsymbol{x})\rangle^2)^{1/2} = \left(\int\frac{dk}{k}W^2(kR)\mathcal{P}_{\delta_r}(\eta,k)\right)^{1/2}, \quad (5.70)$$

where $W$ is the Fourier transform of the top-hat window function: $W(x) = 3(\sin x - x\cos x)/x^3$. It turned out that the dispersion of the density perturbation at the horizon crossing of some mode $k_1$ smoothed over the horizon scale at that moment (namely, $\eta = k_1^{-1}$), $\sigma(\eta = k_1^{-1}, R = k_1^{-1})$, is maximum and is $\sim \mathcal{A}^2$ at around $k_1 \sim 0.7k_p$ (see Fig. 5.2), which means the PBH formation is most efficient at around this moment, so we restrict our attention to this moment in the following.

To determine the abundance of PBHs, the PDF of the density perturbations is necessary. In many cases the PDF of the density perturbations is assumed to be Gaussian, but in our situation it is in general highly non-Gaussian, since the density perturbation is generated due to the second-order effects of tensor perturbations, whose statistical properties are assumed to be Gaussian in this work. We can simulate the PDF of $\delta_r$ by randomly

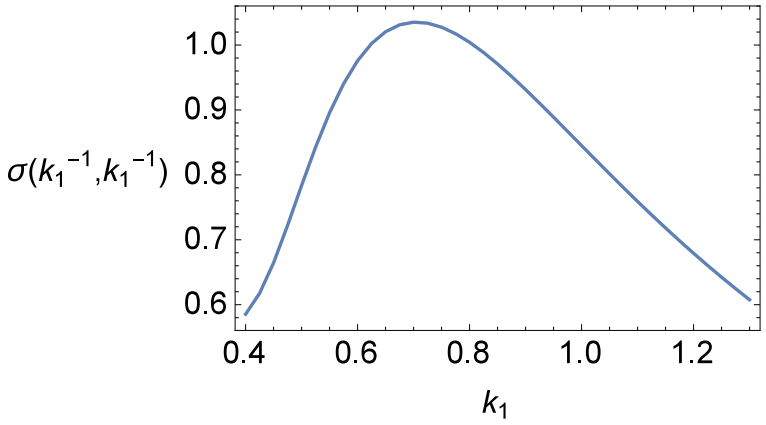


Figure 5.2: The dependence of $\sigma(\eta = k_1^{-1}, R = k_1^{-1})$ on $k_1$.

generating the Fourier modes of GWs $\{h^r(\boldsymbol{k})\}$ repeatedly, in principle (for the details see the Appendix F), whose result is shown in Fig.5.3. The simulated PDF $P(\delta_r)$ of $\delta_r$ turns out to be well approximated by the formula (F.29). The fraction of the volume which has collapsed into PBHs at the moment of the formation is estimated by

$$\beta = \int_{\delta_{r,th}}^{\infty} \tilde{P}(\delta_r - \langle\delta_r\rangle)d\delta_r = \int_{\delta_{r,th}/\mathcal{A}^2}^{\infty} P(\tilde{\delta}_r)d\tilde{\delta}_r, \tag{5.71}$$

where $\delta_{r,\mathrm{th}}$ is the threshold amplitude required for the formation of PBHs, in the following assumed to be $\delta_{r,\mathrm{th}} \sim 0.4$ [81, 82][†6]. This quantity $\beta$ has been constrained observationally on various mass scales and we use Fig.9 of [12]. Upper bounds for each value of $\beta$, corresponding to different masses of PBHs, can be obtained, which is shown in Fig.5.4. Here, upper bounds are shown as a function of $k_p$, using the following relation between the mass of PBHs and the comoving scale of perturbations:

$$M_{\mathrm{PBH}} = 2.2 \times 10^{13} M_\odot \left(\frac{k}{1\mathrm{Mpc}^{-1}}\right)^{-2}. \tag{5.72}$$

Note that the dependence of the upper bounds on the perturbation scales is logarithmically weak, which can be understood from the exponential dependence of the PDF on $\delta_r$ and hence on $\mathcal{A}^2$ for $0 \lesssim \delta_r$.

Let us compare this PBH bound with BBN and CMB bound. To see this let us first rederive the formula for the energy density of gravitational waves $\rho_{\mathrm{GW}}$ on sub-horizon

[†6]In these papers the initial conditions of numerical simulations were given in terms of the curvature profile in the limit of the vanishing ratio of the Hubble radius to the scale of perturbation, which is related to the radial profile of the curvature perturbation. In the present work scalar perturbations are sourced by second-order tensor perturbations, and so strictly speaking the threshold values obtained in these numerical simulations may not be directly applied. A more precise treatment may require dedicated numerical simulations, which is beyond the scope of this work. It would be worthwhile to mention here that the energy density of GWs is expected to help gravitational collapse, in light of previous works on direct collapse of nonlinear GWs, mentioned in the footnote †2. This effect is not taken into account in the present work, so in this sense our upper bounds may be conservative.

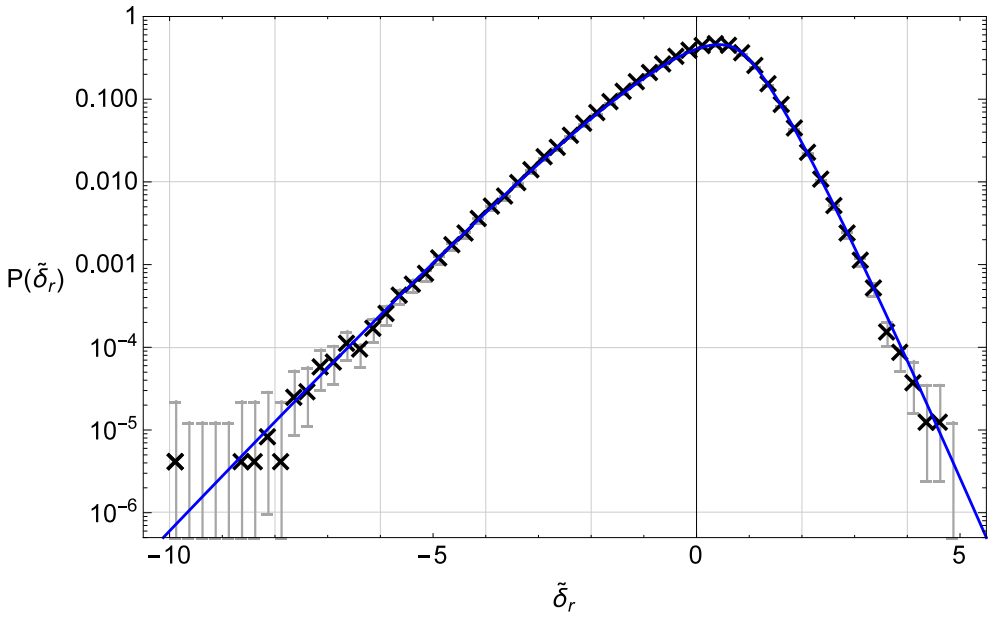


Figure 5.3: The PDF of $\tilde{\delta}_r \equiv (\delta_r - \langle\delta_r\rangle)/\mathcal{A}^2$ for $\sim 10^6$ realizations of $\{h^r(\boldsymbol{k}_i)\}$ (see Appendix F for the details). The curve is the approximate PDF of $\tilde{\delta}_r$ given by (F.29).

scales. Noting $\rho_{\rm GW} = -\langle S_1\rangle/4\pi G a^2$ from (5.14), where the brackets here imply temporal and spatial average (see e.g. [232] for more details), let us rewrite $\langle S_1/a^2\rangle$ in the following. By integration by parts and using (5.13),

$$\begin{aligned}\left\langle \frac{S_1}{a^2}\right\rangle &= \left\langle \frac{1}{a^2}\left(-\frac{1}{4}h'_{ij}h^{ij\prime} - \frac{3}{2}\mathcal{H}h_{ij}h^{ij\prime} + \frac{1}{4}h_{ij}h^{ij\prime\prime}\right)\right\rangle \\ &= \left\langle -\frac{1}{4}\dot{h}_{ij}\dot{h}^{ij} - \frac{5\dot{a}}{4a}h_{ij}\dot{h}^{ij} + \frac{1}{4}h_{ij}\ddot{h}^{ij}\right\rangle = -\frac{1}{2}\langle \dot{h}_{ij}\dot{h}^{ij}\rangle, \end{aligned} \tag{5.73}$$

hence[†7],

$$\rho_{\rm GW} = \frac{\langle \dot{h}_{ij}\dot{h}^{ij}\rangle}{8\pi G}. \tag{5.74}$$

Assuming the delta-function power spectrum (5.59),

$$\rho_{\rm GW} = \frac{\mathcal{A}^2\langle \dot{D}(\eta,k_p)^2\rangle}{2\pi G} = \frac{\mathcal{A}^2}{2\pi G a^2}\left\langle\left(\frac{\cos k_p\eta}{\eta} - \frac{\sin k_p\eta}{k_p\eta^2}\right)^2\right\rangle \sim \frac{\mathcal{A}^2}{4\pi G a^2\eta^2}. \tag{5.75}$$

The following will be used shortly, obtained from $\rho_{\rm rad} = 3H^2/8\pi G = 3/8\pi G a^2\eta^2$:

$$\frac{\rho_{\rm GW}}{\rho_{\rm rad}} = \frac{2}{3}\mathcal{A}^2. \tag{5.76}$$

It is often useful to characterize the existence of gravitational waves in terms of the effective number of degrees of freedom of *fermionic* relativistic species. First note that

[†7]If we defined tensor perturbations without the factor 2 in front of $h_{ij}$ in (5.9), then we would obtain, instead of (5.74), the formula often used in the literature: $\rho_{\rm GW} = \langle \dot{h}_{ij}\dot{h}^{ij}\rangle/32\pi G$.

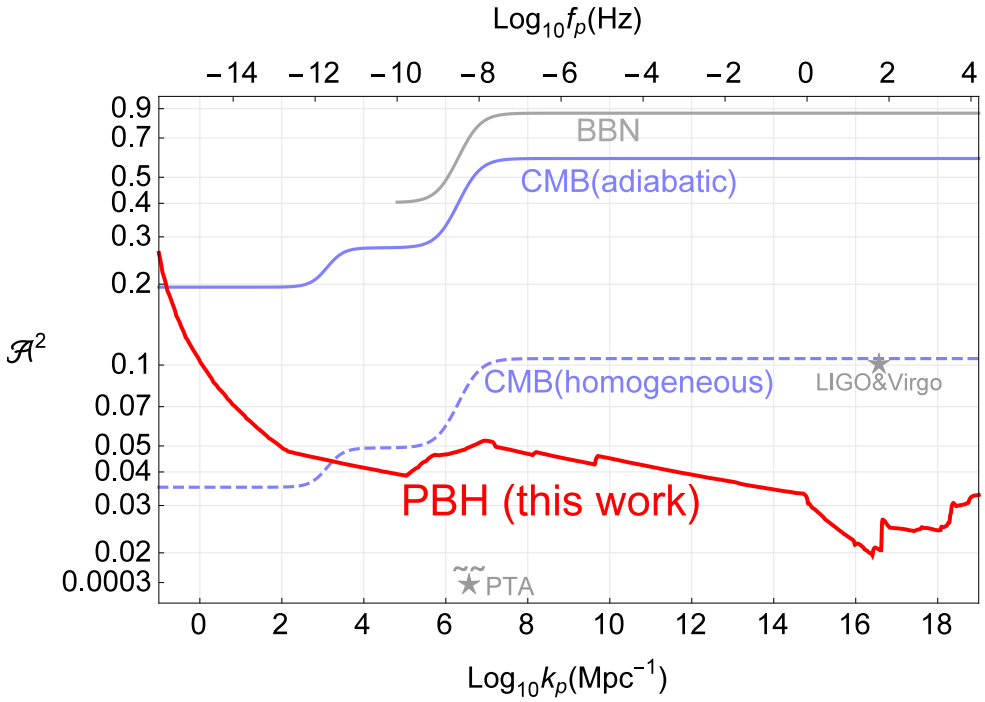


Figure 5.4: Comparison of upper bounds on the amplitude $\mathcal{A}^2$ of a spike in the power spectrum of primordial tensor perturbations, $\mathcal{P}_h(k) = \mathcal{A}^2 k\delta(k - k_p)$, as a function of $k_p$. Note that in this figure the PTA bound is shown to be more than two-orders-of-magnitude tighter than the PBH bound at around $4 \times 10^6 \mathrm{Mpc}^{-1}$.

the total energy density of radiation without the presence of gravitational waves is written as

$$\rho_{\rm rad}(T) = \frac{\pi^2}{30} g_* T^4. \tag{5.77}$$

Here, $g_*$ is the effective number of degrees of freedom of relativistic species and at around the epoch of BBN it is given by [195, 233]

$$g_* = 2 + \frac{7}{8}(4 + 2N_\nu), \tag{5.78}$$

where $N_\nu$ is the standard effective number of neutrinos $N_\nu = 3.046$[†8]. This value of $g_*$ is obtained by counting the degrees of freedom of photons, electrons, positrons, and (anti-)neutrinos. Note that electrons and positrons annihilate when $T \simeq 0.5$MeV and hence should not be included at the photon decoupling. Effects of GWs or, possibly, dark radiation, are denoted by $\Delta N_{\rm eff}$, as a correction to $N_\nu$ above. In the following we use $\Delta N_{\rm GW}$ as a contribution of GWs and relate it to $\mathcal{A}^2$. When GWs are present, the total energy density becomes (noting (5.69))

$$\rho_{\rm tot} = \rho_{\rm rad}(T)(1 + \langle \delta_r \rangle) + \rho_{\rm GW}, \tag{5.79}$$

[†8]The slight deviation from $N_\nu = 3$ arises from the slight heating of neutrinos due to the relic interactions between $e^\pm$ and neutrinos at the epoch of $e^\pm$ annihilations, which took place only shortly after the neutrino decoupling [200].

which can be written, with the redefinition of the temperature $T \to T(1 + \langle \delta_r \rangle/4)$, as

$$\rho_{\rm tot} = \rho_{\rm rad}(T) + \rho_{\rm GW}. \tag{5.80}$$

Note that $\rho_{\rm GW}/\rho_{\rm rad} \sim \mathcal{P}_h \ll 1$ by definition of tensor "perturbations", or this is marginally guaranteed at least thanks to our PBH constraint. Therefore in the following we assume this inequality, but it turns out that most of the upper limits discussed below are too weak to be compatible with this condition, which may appear to invalidate the following analyses. However, our purpose here is to show that other constraints are not so tight and hence the above condition can be assumed. After the horizon crossing of GWs, its energy density starts to scale as $\propto a^{-4}$, while, denoting the effective degrees of freedom of relativistic species in terms of entropy at temperature $T$ by $g_S(T)$, the photon temperature evolves following $g_S(T)T^3a^3 =$const. (i.e. constant entropy) and $\rho_{\rm rad} \propto g_* T^4 \sim 1/(a^4 g_S^{1/3})$ (see e.g. [233]). Then, defining $\Omega_{\rm GW} \equiv \rho_{\rm GW}/\rho_{\rm crit} \simeq \rho_{\rm GW}/\rho_{\rm rad}$,

$$\Omega_{\rm GW}(T) = \left(\frac{g_S(T)}{g_S(T_{\rm in})}\right)^{1/3} \Omega_{\rm GW}(T_{\rm in}), \tag{5.81}$$

where $T_{\rm in} = T_{\rm in}(k_p)$ is the temperature of radiation at the moment of the horizon crossing of GWs with comoving wavenumber $k_p$, and $T < T_{\rm in}$[†9]. The contribution of GWs is characterized by $\Delta N_{\rm GW}$ as follows, at the epoch of BBN;

$$\rho_{\rm rad}(T) + \rho_{\rm GW}(T) = \frac{\pi^2}{30}\left[2 + \frac{7}{8}\left\{4 + 2(N_{\rm sta} + \Delta N_{\rm GW})\right\}\right] T^4, \tag{5.83}$$

which leads to

$$\rho_{\rm GW}(T) = \rho_{\rm rad}(T) \times \frac{7}{8} \times 2 \times \Delta N_{\rm GW}(T) \Big/ \left\{2 + \frac{7}{8}(4 + 2N_{\rm sta})\right\} \fallingdotseq \frac{7}{43}\rho_{\rm rad}\Delta N_{\rm GW}(T). \tag{5.84}$$

Since

$$\Omega_{\rm GW}(T_{\rm in}) \simeq \frac{2}{3}\mathcal{A}^2 \tag{5.85}$$

from (5.76), $\Delta N_{\rm GW}(T)$ can be written as

$$\Delta N_{\rm GW}(T) = \frac{43}{7}\Omega_{\rm GW}(T) = \frac{86}{21}\mathcal{A}^2 \left(\frac{g_S(T)}{g_S(T_{\rm in})}\right)^{1/3}. \tag{5.86}$$

An upper bound on $\Delta N_{\rm eff} < \Delta N_{\rm upper}$ is usually translated into an upper bound on $\Delta N_{\rm GW}$, $\Delta N_{\rm GW} < \Delta N_{\rm upper}$. As is also mentioned previously, here it is assumed that any physical

[†9] In [234] the following convenient fitting function is shown:

$$g_S(T_{\rm in}(k)) = g_{S0}\left\{\frac{A + \tanh\left[-2.5\log_{10} k/2\pi f_1\right]}{A+1}\right\}\left\{\frac{B + \tanh\left[-2.0\log_{10} k/2\pi f_2\right]}{B+1}\right\}, \tag{5.82}$$

where $A = (-1 - g_{\rm BBN}/g_{S0})/(-1 + g_{\rm BBN}/g_{S0})$, $B = (-1 - g_{\rm max}/g_{\rm BBN})/(-1 + g_{\rm max}/g_{\rm BBN})$, $g_{S0} = 3.91$, $g_{\rm BBN} = 10.75$, $f_1 = 2.5 \times 10^{-12}$Hz and $f_2 = 6.0 \times 10^{-9}$Hz. As for $g_{\rm max}$ following [234] we assume the sum of the standard-model particles, $g_{\rm max} = 106.75$. Note that $k/2\pi f_1 = k/(1.6 \times 10^{-3}{\rm pc}^{-1})$ and $k/2\pi f_2 = k/(3.9{\rm pc}^{-1})$.

mechanisms, both known and unknown, contribute positively to $N_{\rm eff}$. However, it would be worthwhile to note that at least there are examples where $N_{\rm eff}$ decreases [201–203]. The requirement above, $\Delta N_{\rm GW} < \Delta N_{\rm upper}$, is translated into an upper bound on $\mathcal{A}^2$ from (5.86) as follows:

$$\mathcal{A}^2 \lesssim \frac{21}{86}\left(\frac{g_S(T_{\rm in})}{g_S(T)}\right)^{1/3}\Delta N_{\rm upper}. \tag{5.87}$$

Note that $g_S(T) = 10.75$, for BBN.

On the other hand, at the epoch of photon decoupling,

$$\begin{aligned}&\rho_{\rm rad}(T) + \rho_{\rm GW}(T)\\ &= \frac{\pi^2}{30}\left\{2 + 2\times\frac{7}{8}\left(\frac{4}{11}\right)^{4/3}(N_\nu + \Delta N_{\rm GW})\right\},\end{aligned} \tag{5.88}$$

which yields

$$\Omega_{\rm GW}(T) = \frac{2\times\frac{7}{8}\left(\frac{4}{11}\right)^{4/3}}{2 + 2\times\frac{7}{8}\left(\frac{4}{11}\right)^{4/3}N_\nu}\Delta N_{\rm GW} \simeq 0.13\Delta N_{\rm GW}. \tag{5.89}$$

So in this case we find

$$\mathcal{A}^2 < 0.13\times\frac{3}{2}\times\Delta N_{\rm upper}\left(\frac{g_S(T_{\rm in})}{g_S(T)}\right)^{1/3}. \tag{5.90}$$

Note that this constraint depends on $g_S$, which one may regard as a drawback of these methods since $g_S$ is uncertain especially at high temperatures. It also depends on other potential entropy productions [234]. On the other hand, the PBH constraint is not so sensitive to $g_S$ nor other entropy productions.

In order not to spoil BBN, we set, following [234], $\Delta N_{\rm upper} = 1.65$ as a 95% C.L. upper limit, which is applicable for the scales smaller than the comoving horizon at the time of BBN, namely, $6.5\times10^4{\rm Mpc}^{-1} \lesssim k$[†10]. As for CMB constraints, in [196] the use of homogeneous initial conditions of GWs is advocated for SGWB generated, for instance, by quantum fluctuations during inflation. In this case 95 % upper limits are $\Delta N_{\rm upper} = 0.18$ [235][†11]. For adiabatic initial conditions of GWs we refer to

$$N_{\rm eff} = 3.52^{+0.48}_{-0.45} \quad (95\%;\ \ Planck + {\rm WP} + {\rm highL} + H_0 + {\rm BAO}) \tag{5.91}$$

of [42] to set $\Delta N_{\rm upper} = 1.00$ [197].

The current energy density of SGWB, $\Omega_{\rm GW,0}$, is also constrained by LIGO and Virgo, most severely in the band $41.5 - 169.25$Hz as $\Omega_{\rm GW,0} \lesssim 5.6\times10^{-6}\times\log(169.25/41.5) \simeq 8\times10^{-6}$ [236]. Noting $\Omega_{\rm GW,0} \sim (4/100)^{1/3}\times2\mathcal{A}^2/3z_{\rm eq} \sim 7.6\times10^{-5}\mathcal{A}^2$ ($z_{\rm eq}\sim3000$ is the

[†10]The effect of potential extra degrees of freedom of relativistic species, which we denote by $\Delta N$, on BBN is summarized as follows (see e.g. [233]); $\Delta N > 0$ increases the expansion rate, leading to the freeze-out of the conversion reaction between protons and neutrons at a higher temperature; this increases neutrons available at BBN and therefore $^4$He is produced more.

[†11]One would get somewhat tighter constraints than those in [235] for homogeneous initial conditions of GWs energy density, by repeating the analysis of [235] using more recent data.

redshift at the matter-radiation equality, and the factor $z_{\rm eq}^{-1}$ reflects $\Omega_{\rm GW} \propto (1+z)/(1+z_{\rm eq})$ during a matter-dominated era), we have $\mathcal{A}^2 \lesssim 0.1$[†12].

Pulsar timing arrays (PTAs) have also been used to constrain GWs. Following [234] we use the most stringent upper bound around $f = 5.72\times10^{-9}$Hz ($\sim 4\times10^6 {\rm Mpc}^{-1}$), $\Omega_{\rm GW,0} \sim (4/11)^{1/3} \times 2\mathcal{A}^2/3z_{\rm eq} \lesssim 5\times10^{-8}$, which leads to $\mathcal{A}^2 \lesssim 3\times10^{-4}$.

Note that GW detectors or PTA experiments usually target GWs on a relatively limited frequency range, while cosmological methods like PBHs probe primordial GWs on a wide range of frequencies, and this is another advantage of PBHs in constraining primordial GWs (see Fig.5.4).

These upper bounds as a function of $k_p$ is shown in Fig.5.4 along with the PBH upper bound. One may not regard some of these constraints as meaningful, because upper limits correspond to the amplitude of GWs which is (almost) nonlinear.

PBH upper bounds can also be expressed in temrs of $\Delta N_{\rm GW}$ using (5.86), and also in terms of the current energy density parameter of GWs, $\Omega_{\rm GW,0}$, using

$$\Omega_{\rm GW,0} = \frac{2\mathcal{A}^2}{3z_{\rm eq}} \left( \frac{g_{S0}}{g_S(T_{\rm in})} \right)^{1/3}, \tag{5.92}$$

which follows from (5.81) and (5.85). Here, the factor $z_{\rm eq} \simeq 3000$ takes into account the relative dilution of the energy density of GWs in comparison to that of non-relativistic matter during the matter domination. PBH upper bounds in terms of these quantities are shown in Fig.5.5. Be reminded that if future experiments reveal meaningfully large value of $\Delta N_{\rm eff}$, then primordial GWs provide a possible explanation, as well as dark radiation. However, if the value of $\Delta N_{\rm eff}$ is large, say 0.5, exceeding the values indicated in Fig.5.5, then we may exclude primordial GWs as a candidate thanks to our PBH bounds on them[†13]. This shows an example of how our PBH upper bounds can provide useful information about the early universe.

## 5.4 Discussion

A novel method to probe primordial gravitational waves is discussed, which method involves the formation of PBHs. If the amplitude of tensor perturbations initially on super-horizon scales is very large, large-amplitude scalar perturbations are generated due to the second-order effects of tensor modes. If the typical amplitude of resultant induced scalar

[†12]They also obtained weaker upper bounds on a few other frequency ranges other than the one around $\sim$ 100Hz, which we did not include. Also, strictly speaking, in [236] some power low frequency dependence is assumed in each band, and so their results may not be directly translated into constraints on a narrow peak in the power spectrum we consider. Indeed in [237] an optimal analysis method is discussed to search for a sharp emission line of SGWB, which can increase the signal-to-noise ratio by up to a factor of seven. That is, our comparison here is only a crude one, but it is sufficient for our purposes. The same applies to the comparison with PTA.

[†13]There may be a loophole, however. Logically, if primordial GWs follow a tremendously non-Gaussian PDF, it might be possible to realize large $\Delta N_{\rm GW}$ without producing too may PBHs. See also a discussion about possible effects of non-Gaussianity of primordial GWs, made in the Discussion of this Chapter.

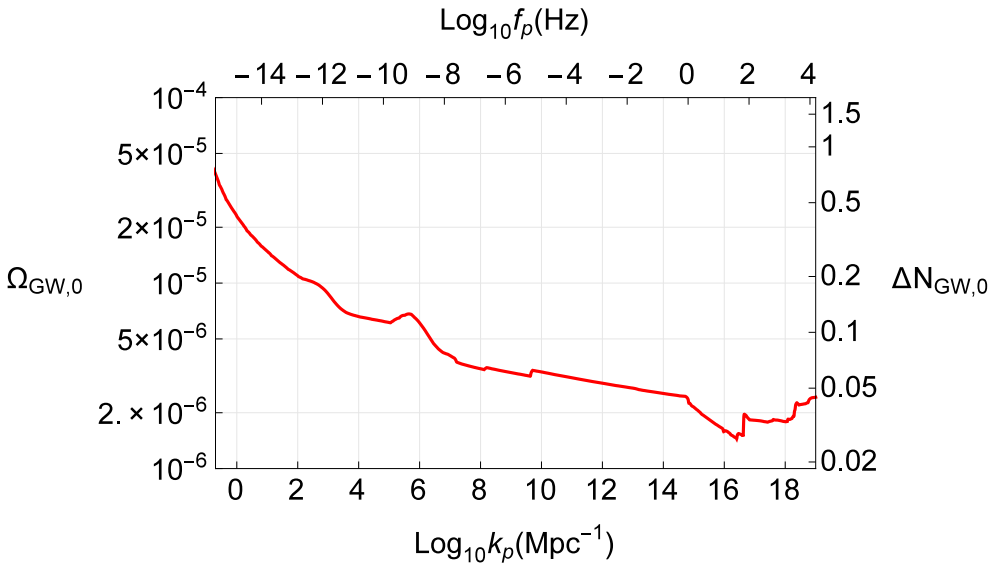


Figure 5.5: PBH upper bounds in terms of $\Omega_{\rm GW,0}$ and $\Delta N_{\rm GW}$ as a function of $k_p$.

perturbations becomes too large, PBHs are produced too abundantly to a level that is inconsistent with various types of existing observations which have placed upper bounds on the abundance of PBHs on a wide range of mass scales.

To constrain tensor modes from PBHs, as well as the power spectrum of the radiation density perturbations, we have calculated the PDF of the radiation density perturbations, which is in general highly non-Gaussian since they are sourced by the terms in the Einstein equations which are second-order in tensor modes $h_{ij}$. The PDF is inferred from a Monte Carlo simulation and an approximate formula for the PDF is also derived.

Using this PDF we have placed upper bounds on the initial amplitude of tensor modes assuming a delta-function power spectrum. PBH bounds have been compared with other bounds obtained from BBN, CMB, LIGO and Vigo, and PTAs.

As already mentioned PBH constraints are applicable from $\sim$ Gpc all the way down to $\sim 0.3$m if we assume the number of e-folds during inflation is sixty. Note that the exclusion of an overproduction of smallest PBHs ($M_{\rm PBH} \lesssim 10^5 g$) depends on the assumption that stable Planck mass relics are left over at the end of Hawking evaporation, which contribute to cold dark matter (see [107], [12] and references therein). The range of comoving scales corresponding to $M_{\rm PBH} \lesssim 10^5 g$ is roughly $\lesssim 50$m, and so PBH upper bounds in this range depend on this assumption. If Planck mass relics are not formed, to what extent an overproduction of PBHs with $M_{\rm PBH} \lesssim 10^5 g$ is cosmologically problematic is uncertain. Such an overproduction of smallest PBHs may lead to an early matter-dominated era, during which PBH binaries are formed and emit GWs, or larger PBHs may form due to merger taking place after the collapse of perturbations of PBHs' density, thereby leaving observable traces [238]. Therefore, in principle one may still exclude such an over production of smallest PBHs even without the left over of Planck mass relics to fully validate our upper bounds on smallest scales, though we do not discuss it in detail here.

In this Chapter the delta function power spectrum of tensor modes (5.59) is assumed and an upper bound on the amplitude of that spike is obtained from the non-detection of

PBHs. This PBH upper bound in this case turns out to be somewhat tighter than upper bounds obtained from BBN or CMB. It would be worthwhile to generalize our analysis to other types of tensor power spectrum such as a blue spectrum. Let us briefly discuss to what extent a blue tensor spectrum can be constrained by simple estimations. To this end here we assume the tensor power spectrum has the following form:

$$\mathcal{P}_h(k) = r\mathcal{P}_\zeta(k_{\rm ref})\left(\frac{k}{k_{\rm ref}}\right)^{n_T}, \quad (k < k_{\rm max}), \tag{5.93}$$

where $\mathcal{P}_\zeta$ is the dimensionless power spectrum of the curvature perturbation on uniform-density hypersurfaces and $r$ is the tensor-to-scalar ratio, here defined at $k_{\rm ref}= 0.01{\rm Mpc}^{-1}$. Let us further assume $r = 0.2$ and $\mathcal{P}(k_{\rm ref}) = 2.2 \times 10^{-9}$ following [234] and also $k_{\rm max} \sim 1{\rm Gpc}^{-1}{\rm e}^{60} \sim 3{\rm m}^{-1}$. If we simply require $\mathcal{P}_h(k_{\rm max}) \lesssim 0.04$, referring to (5.6), we obtain $n_T \lesssim 0.3$, which is tighter than other constraints such as BBN constraints shown in [234]. Once more, this PBH bound is not so sensitive to the details of a potential early matter-dominated era phase nor an entropy production, on which constraints other than PBHs are sensitive [234]. If we use a more secure but weaker constraint on PBHs of around $10^5 g$ by their entropy production [12], we may require $\mathcal{P}_h(20{\rm km}^{-1}) \lesssim 0.4$, leading to $n_T \lesssim 0.4$, still tighter than other constraints. To conclude, PBHs can provide important constraints also on a blue spectrum, though a more careful analysis would be merited.

We have used perturbative expansion in terms of small perturbations so far, so one may be worried about the validity of the PDF, shown in Fig.5.3, close to the threshold of $\delta_{\rm th} \simeq 0.4$ we adopted, which value indicates further nonlinearities may affect. Very naively, next-order corrections would appear in the fundamental equations whose magnitude is $\sim \mathcal{O}(h_{ij}) \sim \sqrt{0.4} \sim 0.6$, so the upper bounds can be affected by $\sim 60\%$. Certainly this estimation is very naive and so a more careful estimation would be merited. If additional nonlinearities enlarge the amplitude of induced perturbations, then our upper bounds based on the present formulation would be conservative. To see how these nonlinearities can affect eventual results, one may write down the next-order correction terms, and the behaviors of these terms may provide insight into how additional nonlinearities affect our results. Gradient expansion approach may also be helpful (see e.g. [97] and references therein). This is another perturbative approach based on the smallness of the ratio of spatial derivatives to time derivatives for perturbations on super-horizon scales. This is valid only on super-horizon scales, but this can treat nonlinear perturbations, relevant to PBH formation. If one compares the amplitude of induced perturbations obtained by the gradient expansion approach and that we have obtained, one would gain insight into how nonlinearities might affect. However, the gradient expansion approach itself is not perfect either, since it does not allow us to evolve perturbations up to the moment of the horizon crossing of perturbations under consideration, which is required to calculate the probability of PBH formation. Refining our results further would be a formidable task, which is beyond the scope of this work. The present formulation would be acceptable, providing moderately precise and potentially conservative bounds, for our purpose here to propose a novel method to constrain primordial tensor perturbations on small scales from PBHs with detailed calculations for the first time. Though PBH upper bounds on scalar perturbations have long been known, probably since [143], we have newly found PBH upper bounds on *tensor* perturbations as well.

In this Chapter we have assumed Gaussianity of primordial tensor perturbations, but PBH constraints on tensor perturbations depend on the statistics of tensor perturbations,

determining the statistics of induced density perturbation, just as PBH constraints on *scalar* perturbations depend on the statistics of scalar perturbations [190]. If high-$\sigma$ realizations of tensor perturbations are suppressed (enhanced) in comparison to a Gaussian case, PBH constraints on tensor perturbations are tighter (weaker). One may conjecture the dependence of PBH constraints of tensor perturbations on the statistics of tensor perturbations is weaker than the dependence of PBH constraints of scalar perturbations on the statistics of scalar perturbations. This is because in the former case the probability of PBHs is determined by the statistics of induced radiation perturbations, generated from second-order tensor perturbations, and so the PDF of induced radiation perturbations is something similar to a $\chi^2$ distribution (see (F.28)). That is, the probability of high-$\sigma$ peaks of radiation leading to PBH formation is determined by lower-$\sigma$ realizations of tensor perturbations, for which non-Gaussianity is less important than it is for higher-$\sigma$ realizations, but a more careful analysis on this matter also would be merited.

We have restricted attention to PBH formation as a result of direct collapse of radiation density perturbations induced by second-order tensor perturbations, but these density perturbations would also dissipate to induce CMB spectral distortion, and hence constraints on CMB spectral distortion would also be used to probe tensor perturbations. Furthermore, second order tensor perturbations naturally induce perturbations in DM as well, and if the amplitude of induced DM perturbations is large, it leads to substantial formation of UCMHs. That is, (potential) constraints on UCMHs can also be translated into upper bounds on tensor perturbations, which will be explored elsewhere [239].

# Chapter 6

# Conclusion

Primordial perturbations on a wide range scales were generated in the early universe. Those with largest comoving wavelengths, $\mathcal{O}(\mathrm{Mpc}) - \mathcal{O}(\mathrm{Gpc})$, are (indirectly) observed as anisotropy of cosmic microwave background (CMB), or they serve as the seeds of large-scale-structures of the universe we see today, as a result of which the nature of these perturbations on large scales are relatively well understood. On the other hand, primordial perturbations on much smaller scales should also exist, but the nature of these is less understood. Since different models of the early universe predict different properties of primordial perturbations on small scales, investigation of these also provides valuable information about the early universe.

There are several methods to probe primordial power on small scales, one of which is primordial black holes (PBHs), which was reviewed in Chapter 2. If an overdensity of order unity exists on the horizon scale in the early universe, this region collapses to form a black hole. There has been no conclusive evidence for the existence (both in the past and in the present) of these PBHs, which fact itself serves as a unique tool to probe the early universe. If we assume standard almost-scale-invariant primordial perturbations with amplitude $\mathcal{O}(10^{-5})$, confirmed on large scales mentioned above, then the probability of PBH formation is vanishingly small. In order for PBHs to be produced to an observationally relevant level, we must have the dispersion, or the typical squared amplitude of primordial perturbations at horizon crossing, of $\sim 10^{-3}$, under the assumption of Gaussianity of primordial perturbations (See Chapter 2 for more details). In other words, the amplitude of primordial perturbations on small scales has to be smaller than this values, in order not to overproduce PBHs, and this is the only method we have to probe primordial power all the way down to smallest scales.

As we briefly reviewed in Chapter 2, Another method to probe primordial power on small scales is CMB spectral distortion. In the sufficiently early universe ($z \gtrsim 2 \times 10^6$), the energy spectrum of photons is maintained to be a black body spectrum well, which is characterized by only one parameter, the temperature. This is because at such high redshifts all of the three predominant processes determining the photon spectrum, which are double Compton scattering (DS), Bremsstrahlung (BS) and Compton scattering (CS), are efficient, in comparison to the expansion rate of the universe, with DS and BS controlling the number of photons, and with CS redistributing photons in frequency. Below $z \sim 2 \times 10^6$, DS and BS become relatively inefficient, after which a black body spectrum can no longer be kept when some energy is injected into the background universe.

During the redshift interval $5 \times 10^5 \lesssim z \lesssim 2 \times 10^6$, CS is still efficient, and under these circumstances the photon spectrum becomes a Bose-Einstein spectrum with an effective chemical potential if some energy is injected into the background universe, and so this redshift range is sometimes called the "$\mu-$era". CMB spectral distortion has been tightly constrained by COBE/FIRAS and will be detected or more tightly constrained by future experiments, and these have provided and will provide valuable information about the mechanisms which release energy in the early universe. One of important physical mechanisms of energy injection, leading to CMB distortion, is dissipation of primordial perturbations due to diffusion of photons. The energy originally stored in acoustic waves is released in this process of diffusion damping, which causes CMB $\mu$-distortion if it happens during the $\mu-$era.

Supermassive black holes (SMBHs) of $10^{9-10} M_\odot$ have been observed at high redshifts ($z \sim 10$). The reason why such gigantic SMBHs already existed at such high redshifts is not fully understood yet, and so far it appears to be difficult for usual astrophysical processes to provide an established explanation, though intensive studies are under way. Given this situation, it would be worthwhile and interesting to consider a possibility of PBHs providing the seeds of these SMBHs. To this end, let us recall that, as is discussed in Chapter 3, primordial perturbations whose comoving wavenumber lies in the range $50\mathrm{Mpc}^{-1} \lesssim \mathrm{k} \lesssim 10^4\mathrm{Mpc}^{-1}$ dissipate during the $\mu-$era, leading to positive $\mu-$distortion. This implies primordial perturbations of these wavenumbers can be constrained by CMB $\mu-$distortion, and resultant COBE/FIRAS upper bounds are tighter than upper bounds obtained by the absence of PBHs. This means that PBHs larger than $10^{4-5} M_\odot$ are excluded, to be consistent with COBE/FIRAS upper bounds on $\mu-$distortion. However, this conclusion is based on the assumption that primordial perturbations are Gaussian, and hence can be evaded if primordial perturbations (on small scales) are highly non-Gaussian. A few examples of such models were discussed, which predict highly non-Gaussian and large amplitude small-scale primordial perturbations with a certain probability, and consequently predict formation of PBHs as massive as necessary to later serve as the seeds of SMBHs at high redshifts, without violating CMB distortion bounds by COBE/FIRAS. There we have resorted to two-inflation models which are characterized by the form of the inflaton potential depicted in Fig.3.4.

In Chapter 4, we have discussed another novel probe, named *acoustic reheating*, of primordial power in the comoving wavenumber range $10^4\mathrm{Mpc}^{-1} \lesssim k \lesssim 10^5\mathrm{Mpc}^{-1}$. These modes dissipate before the $\mu-$era, which (basically) only results in a slight global increase in the temperature of the universe (acoustic reheating), without causing substantial CMB $\mu-$distortion, and so the dissipation of these modes has not received much attention for a long time. However, recently in [43] (see also [120]), we have pointed out that acoustic reheating caused by the dissipation of these modes results in an increase in the number density of photons, without changing that of baryons, and hence results in a slight decrease of the baryon-to-photon ratio $\eta$. Since the values of $\eta$ at the epoch of big bang nucleosynthesis and photon decoupling are independently inferred from observations of the current abundance of the light elements and CMB anisotropy, too much decrease in $\eta$ between these two epochs contradicts with observations. This consideration lead to upper bounds on the amplitude of primordial perturbations in the above range of comoving wavenumbers.

Perturbations to the isotropic and homogeneous universe can be decomposed into

scalar, vector and tensor parts, and Chapters 2, 3 and 4 are dedicated to discussions of investigation of primordial scalar perturbations on small scales. In Chapter 5, we have also discussed investigation of primordial tensor perturbations on small scales. In linear theory, scalar, vector and tensor perturbations evolve independently, but at the second-order level they are coupled. For instance, scalar perturbations can be generated from second-order tensor perturbations (*induced scalar perturbations*). If the amplitude of primordial tensor perturbations is sufficiently large, then the amplitude of induced scalar perturbations becomes also large enough for PBHs to be generated abundantly. This means that the absence of PBHs can also be translated into upper bounds on primordial *tensor* perturbations, just as it leads to upper bounds on *scalar* perturbations. PBH upper bounds on the delta-function power spectrum, introduced by (5.59), are expressed in Fig.5.4, which shows PBHs provide valuable bounds on a relatively wide range of scales, in comparison to other bounds.

To conclude, primordial power on small scales causes a wealth of phenomenology, such as PBH formation, acoustic reheating (Chapter 4) and CMB distortion. PBHs potentially have various implications, for instance, they may explain SMBHs at high redshifts (Chapter 3). Viewed from a different angle, constraints on these consequences of primordial power on small scales can be used to place upper bounds on primordial short-wavelength scalar (Chapter 4) as well as tensor perturbations (Chapter 5), which would provide helpful information about the early universe when primordial perturbations arose. These constraints on primordial power are often expressed in terms of the power spectrum, but, importantly, these constraints depend on the statistical properties of primordial perturbations, for which Gaussianity is often assumed. In other words, what we obtain should be regarded as joint constraints on the power spectrum and non-Gaussianity. This tendency is most noticeable for PBH constraints, which are related to the extremely rare, high-$\sigma$ realizations of perturbations. This is why it was possible to produce appreciable amount of PBHs to explain SMBHs at high redshifts, without violating CMB distortion constraints on the dispersion or the typical amplitude of primordial perturbations. With this kept in mind, constraints on primordial perturbations on small scales provide complementary information about the early universe, which can not be obtained by methods based on CMB or LSS. For instance, in Chapter 3, we have discussed a phenomenological inflationary model which can produce PBHs to explain SMBHs, but, viewed from a different angle, PBHs provide a unique tool to constrain those types of features in the inflaton potential discussed there since overproduction of PBHs is inconsistent with various observational facts we have. This would be just one of many known or unknown examples which can only be investigated by probes of small-scale primordial power, discussed in this dissertation.

# Appendices

# Appendix A

# PBH formation revisited

Here we briefly review PBH formation process numerically investigated, following [82,83].

## A.1 Setting up the initial condition

Assuming spherical symmetry, it is convenient to divide the collapsing matter into a system of concentric spherical shells and to label each shell with a Lagrangian comoving radial coordinate $r$. Then the metric can be written in the form used by Misner and Sharp [85]:

$$ds^2 = -a^2dt^2 + b^2dr^2 + R^2(d\theta^2 + \sin^2\theta d\phi^2), \tag{A.1}$$

where $R$, $a$ and $b$ are functions of $r$ and the time coordinate $t$. We consider a perfect fluid with the energy density $\rho(r,t)$ and pressure $P(r,t)$ and a constant equation-of-state parameter $\gamma$, $P(r,t) = \gamma\rho(r,t)$. We express the proper time derivative of $R$ as

$$U \equiv \frac{\dot{R}}{a}, \tag{A.2}$$

with a dot denoting a derivative with respect to $t$.

We define the mass, sometimes referred to as the Misner-Sharp mass in the literature, within the shell of circumferential radius $R$ by

$$M(r,t) = 4\pi \int_0^{R(r,t)} \rho(r,t)R^2dR. \tag{A.3}$$

We consider the evolution of a perturbed region embedded in a flat Friedmann-Lemaitre-Robertson-Walker (FLRW) universe with metric

$$ds^2 = -dt^2 + S^2(t)(dr^2 + r^2d\theta^2 + r^2\sin^2\theta d\phi), \tag{A.4}$$

which is a particular case of (A.1). The scale factor in this background evolves as

$$S(t) = \left(\frac{t}{t_{\rm i}}\right)^{\alpha}, \quad \alpha \equiv \frac{2}{3(1+\gamma)}, \tag{A.5}$$

where $t_{\rm i}$ is some reference time.

We denote the background solution with a suffix 0. In terms of the metric variables defined in (A.1), we find

$$a_0 = 1,\ b_0 = S(t),\ R_0 = rS(t). \tag{A.6}$$

The background Hubble parameter is

$$H_0(t) = \frac{\dot{R}_0}{a_0 R_0} = \frac{\dot{S}}{S} = \frac{\alpha}{t}, \tag{A.7}$$

and the energy density is calculated from the Friedmann equation,

$$\rho_0(t) = \frac{3\alpha^2}{8\pi G t^2}. \tag{A.8}$$

The energy density perturbation is defined as

$$\delta(t,r) \equiv \frac{\rho(t,r) - \rho_0(t)}{\rho_0(t)}. \tag{A.9}$$

We introduce a variable $H$ defined by

$$H(t,r) \equiv \frac{\dot{R}}{aR} = \frac{U}{R}. \tag{A.10}$$

The curvature profile $K(t,r)$ is defined by rewriting $b$ as

$$b(t,r) = \frac{R'(t,r)}{\sqrt{1 - K(t,r)r^2}}. \tag{A.11}$$

This quantity $K(t,r)$ vanishes outside the perturbed region so that the solution asymptotically approaches the background FLRW solution at spatial infinity.

We denote the comoving radius of a perturbed region by $r_{\rm i}$, the precise definition of which will be given later (see eq. (A.15)), and define a dimensionless parameter $\epsilon$ in terms of the square ratio of the Hubble radius $H_0^{-1}$ to the physical length scale of the configuration,

$$\epsilon \equiv \left(\frac{H_0^{-1}}{S(t) r_{\rm i}}\right)^2 = (\dot{S} r_{\rm i})^{-2} = \frac{t_{\rm i}^{2\alpha} t^{\beta}}{\alpha^2 r_{\rm i}^2}, \quad \beta \equiv 2(1-\alpha). \tag{A.12}$$

When we set the initial conditions for PBH formation, the size of the perturbed region is much larger than the Hubble horizon. This means $\epsilon \ll 1$ at the beginning, so it can serve as an expansion parameter to construct an analytic solution of the system of Einstein equations to describe the spatial dependence of all the above variables at the initial moment when we set the initial conditions. Here, the second order solution, obtained in [96], is basically used to provide the initial conditions for the numerical computations.

We define the initial curvature profile as

$$K(0,r) \equiv K_{\rm i}(r), \tag{A.13}$$

where $K_{\rm i}(r)$ is an arbitrary function of $r$ which vanishes outside the perturbed region. Note that, from (A.11), $K_{\rm i}(r)$ has to satisfy the condition

$$K_{\rm i}(r) < \frac{1}{r^2}. \tag{A.14}$$

We normalize radial Lagrangian coordinate $r$ in such a way that $K_{\rm i}(0) = 1$.

In order to represent the comoving length scale of the perturbed region, we use the co-moving radius, $r_{\rm i}$, of the overdense region. We can calculate $r_{\rm i}$ by solving the following equation for the energy density perturbation defined by (A.9):

$$\delta(t, r_{\rm i}) = 0. \tag{A.15}$$

Since the initial condition is taken at the superhorizon regime, when $\epsilon$ is extremely small, the following lowest-order solution [81]

$$\delta(t, r) = \frac{2r_{\rm i}^2}{9r^2}(r^3 K_{\rm i}(r))'\epsilon(t) \tag{A.16}$$

suffices to calculate $r_{\rm i}$, which is obtained by solving

$$3K_{\rm i}(r_{\rm i}) + r_{\rm i}K_{\rm i}'(r_{\rm i}) = 0. \tag{A.17}$$

Note that the physical length scale in the asymptotic Friedmann region is obtained by multiplying by the scale factor $S(t)$, the normalization of which we have not specified. We can therefore set up initial conditions for the PBH formation with arbitrary mass scales by adjusting the normalization of $S(t)$ which appears in the expansion parameter.

We also introduce the averaged over-density, denoted by $\bar{\delta}$ and defined as the energy density perturbation averaged over the over-dense region as follows:

$$\bar{\delta}(t) \equiv \left(\frac{4}{3}\pi R(t, r_{\rm od}(t))^3\right)^{-1} \int_0^{R(t, r_{\rm od}(t))} 4\pi\delta R^2 dR. \tag{A.18}$$

Here $r_{\rm od}(t)$ represents the comoving radius of the overdense region and is the solution of $\delta(t, r_{\rm od}(t)) = 0$. It turns out that $r_{\rm od}(t)$ is very close to $r_{\rm i}$ calculated from (A.17), i.e. lowest-order expansion.

## A.2 Basic equations used in the numerical computations

The following equations were used in [240] to analyze the gravitational collapse of spherically symmetric masses:

$$\dot{U} = -a\left(4\pi R^2 \frac{\Gamma}{w}P' + \frac{MG}{R^2} + 4\pi GPR\right), \tag{A.19}$$

$$\dot{R} = aU, \tag{A.20}$$

$$\frac{(\nu R^2)^{\cdot}}{\nu R^2} = -a\frac{U'}{R'}, \tag{A.21}$$

$$\dot{E} = -P\left(\frac{1}{\nu}\right)^{\cdot}, \tag{A.22}$$

$$\frac{(aw)'}{aw} = \frac{E' + P(1/\nu)'}{w}, \tag{A.23}$$

$$M = 4\pi \int_0^r \rho R^2 R' dr, \tag{A.24}$$

$$\Gamma = 4\pi\nu R^2 R', \tag{A.25}$$

$$P = \gamma\rho, \tag{A.26}$$

$$w = E + P/\nu, \tag{A.27}$$

where $E \equiv \rho/\nu$ and

$$\nu \equiv \frac{1}{4\pi b R^2}. \tag{A.28}$$

The constraint equation reads

$$\left(\frac{R'}{b}\right)^2 = \Gamma^2 = 1 + U^2 - \frac{2M}{R}. \tag{A.29}$$

We introduce the barred variables, which are defined by factoring out the scale factor $S$ and the background energy density $\rho_0$ as shown below:

$$\bar{R} \equiv R/S, \tag{A.30}$$

$$\bar{a} \equiv a, \tag{A.31}$$

$$\bar{U} \equiv U/\dot{S}, \tag{A.32}$$

$$\bar{\rho} \equiv \rho/\rho_0, \tag{A.33}$$

$$\bar{M} \equiv M/(\rho_0 S^3), \tag{A.34}$$

$$\bar{b} \equiv b/S, \tag{A.35}$$

$$\bar{\nu} \equiv S^3\nu, \tag{A.36}$$

$$\bar{\Gamma} \equiv \Gamma, \tag{A.37}$$

$$\bar{P} \equiv P/\rho_0, \tag{A.38}$$

$$\bar{w} \equiv w/(\rho_0 S^3). \tag{A.39}$$

The boundary conditions are imposed such that $\bar{U} = \bar{R} = \bar{M} = 0$ and $\Gamma = 1$ at the center, and $\bar{a} = \bar{\rho} = 1$ on the outer boundary so that the numerical solution is smoothly connected to the FLRW solution.

## A.3 Typical time evolution of perturbed regions in the cosmic time slicing

Let us adopt the following two-parameter family of curvature profile

$$K_{\rm i}(r) = \left[1 + \frac{B}{2}\left(\frac{r}{\sigma}\right)^2\right] \exp\left[-\frac{1}{2}\left(\frac{r}{\sigma}\right)^2\right], \tag{A.40}$$

which was also investigated in [81] (hereafter PM). As mentioned previously, the amplitude of the profile is set to unity at the origin, meaning that we use the same normalization as a spatially closed Friedmann universe. Here the parameters $B$ and $\sigma$ control the shapes of

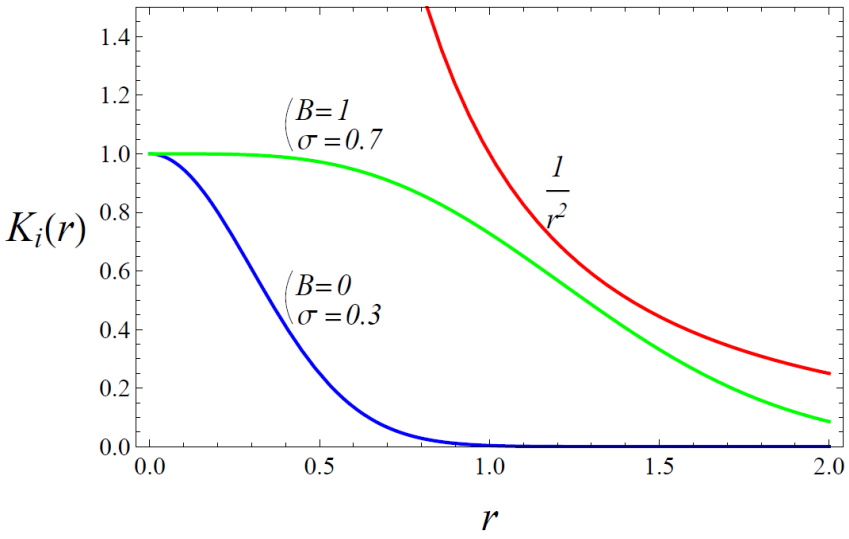


Figure A.1: A wide and narrow initial curvature profiles $K_{\rm i}(r)$ represented by (A.40). Note that $K_{\rm i}(r)$ has to satisfy the condition $K_{\rm i}(r) < 1/r^2$.

initial perturbations. The range of $B$ is limited to $0 \leq B \leq 1$ so that $K_{\rm i}(r)$ is a monotonic function. Two examples of (A.40) are shown in Figure A.1.

In order to relate the initial curvature perturbation to the amplitude of the density perturbation, following PM, let us approximately evaluate the energy density perturbation averaged over the over-dense region, denoted by $\bar{\delta}$ and defined by (A.18), at the time of the horizon crossing. Using (A.16) $\bar{\delta}(t)$ becomes

$$\bar{\delta}(t) = \left(\frac{4}{3}\pi r_{\rm i}^3\right)^{-1} \int_0^{r_{\rm i}} \frac{8\pi r_{\rm i}^2}{9} (r^3 K_{\rm i}(r))' \epsilon(t) dr = \frac{2}{3} K_{\rm i}(r_{\rm i}) r_{\rm i}^2 \epsilon(t). \tag{A.41}$$

By setting $\epsilon(t) = 1$, we define

$$\bar{\delta}_{\rm hc} \equiv \frac{2}{3} K_{\rm i}(r_{\rm i}) r_{\rm i}^2. \tag{A.42}$$

Note that (A.41) is valid only when $\epsilon(t) \ll 1$, so this formula gives just an approximate value of $\bar{\delta}(t)$ at the time of the horizon crossing. Still, (A.42) gives a good indicator of how strong gravity is.

A profile for which $\bar{\delta}_{\rm hc}$ is small corresponds to a small amplitude perturbation and PBH is not formed from this kind of initial configurations. The narrow profile in Figure A.1 with $(B, \sigma) = (0, 0.3)$ corresponds to $\bar{\delta}_{\rm hc} = 0.04$, while the wide profile with $(B, \sigma) = (1, 0.7)$ corresponds to $\bar{\delta}_{\rm hc} = 0.51$. So the width of $K_{\rm i}(r)$ approximately tells how large $\bar{\delta}_{\rm hc}$ is, as can be seen from (A.42). In the following the time evolution of the initial perturbed region for these two cases is presented as illustration.

First, let us look at the case of the narrow profile ($\bar{\delta}_{\rm hc} = 0.04$). The time evolution of the energy density $\bar{\rho}$, normalized by the background energy density, is shown in Figure A.2. In this case the growth of the perturbation stops at some point in time after the horizon crossing and the energy density starts to decrease in the central region, with a

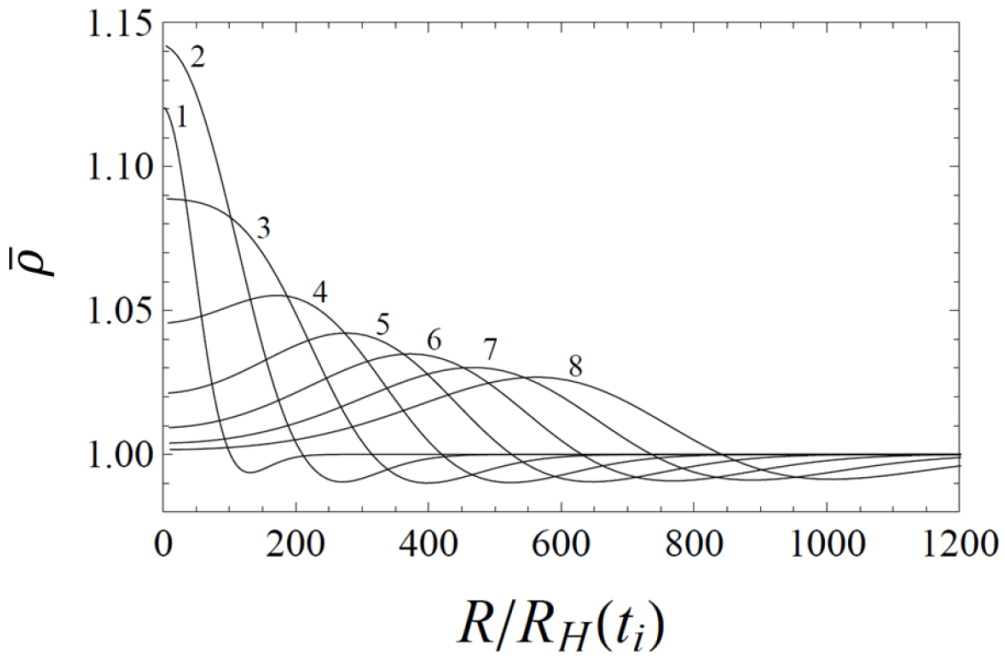


Figure A.2: An example of the time evolution of the energy density perturbation $\bar{\rho}$, normalized by the background energy density, in a case where $(B, \sigma) = (0, 0.3)$ and no PBH is formed. The plots are numbered in order of time evolution.

sound wave propagating outward, the amplitude of which gradually decreases. That is, the initial perturbation dies away and the eventual state at $t = \infty$ is the flat FLRW universe.

Next, let us consider a case where the amplitude of the initial perturbation is sufficiently large ($(B, \sigma) = (1, 0.7), \bar{\delta}_{\rm hc} = 0.51$) and a PBH is eventually formed. The time evolution of $\bar{\rho}$, $U$ and $2M/R$ in this case is shown in Figure A.3.

Near the center the energy density increases drastically and the central perturbed region gradually expands outward. The central perturbed region is always surrounded by the under-dense region.

From (A.10) $U$ is written as $U = HR$ and it corresponds to the recession velocity in the FLRW universe. At an early stage, when the amplitude of the perturbation is small, $U$ is positive everywhere, reflecting the expansion of the universe. In the central region where gravity becomes increasingly stronger, the expansion decelerates rapidly and therefore $U$ decreases rapidly. Then at some point in time, the central region stops expanding and $U$ becomes negative there, starting gravitational contraction.

The mass $M$ is defined by (A.3) and represents the total energy contained in a sphere of radius $R$. When the amplitude of perturbation is small, $M \sim \rho_0(t)R(t,r)^3$ hence $2M/R \propto R^2$. As mentioned earlier, at a later stage the energy density in the central region increases dramatically as a black hole is formed, which is contrasted with the decrease in the energy density in the surrounding region due to the expansion of the universe. In such a situation the mass profile in the central region is steep but is relatively gentle in the surrounding region. This feature of the mass profile can be easily understood by

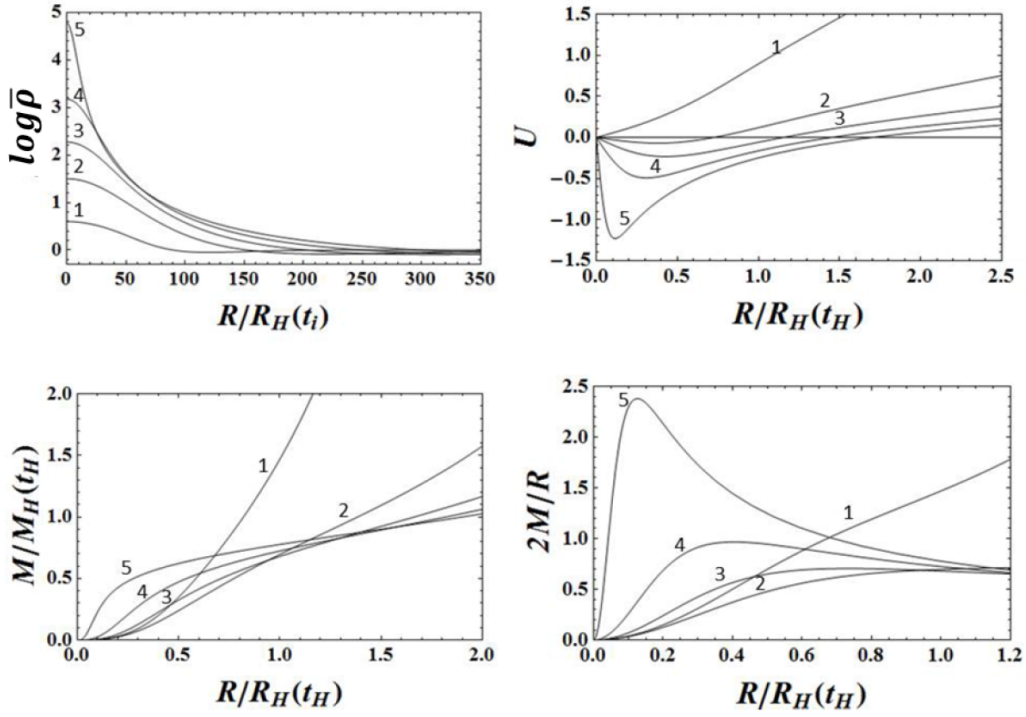


Figure A.3: Examples of time evolution of $\bar{\rho}$(top-left), $U$(top-right), $M$(down-left) and $2M/R$(down-right), calculated using the cosmic time slicing. These are obtained for the case $(B, \sigma) = (1, 0.7)$ and a PBH is formed. Each line is numbered in order of the time evolution.

an analogy with a situation where a star resides in the vacuum, in which case the mass profile is a monotonically increasing function inside the radius of the star and is flat outside that radius. Due to this behavior of $M$ at a later stage, in the region away from the center the mass only weakly depends on $R$ and so approximately $2M/R \propto R^{-1}$ there. This means that a peak appears in the profile of $2M/R$ at some moment in cases where perturbation grows sufficiently. Specifically, in cases where a black hole is formed, the height of this peak exceeds unity and this implies the formation of the apparent horizon from the following arguments [241].

Suppose the trajectory of a photon moving outward, along which

$$adt = bdr, \tag{A.43}$$

so along the geodesic of this photon,

$$\frac{dR}{dt} = \frac{\partial R}{\partial t}dt + \frac{\partial R}{\partial r}dr = a(U + \Gamma)dt, \tag{A.44}$$

where the definition of $U$ (A.2) and $\Gamma = R'/b$, followed from (A.25) and (A.28), have been used. From this we find $dR/dt = 0$ where $U = -\Gamma$ holds, meaning the photon reaching that point cannot escape further away from the center. Since we find $U = -\Gamma$ when $2M/R = 1$ from the constraint (5.4), the peak of $2M/R$ with the height exceeding unity means that there exist photons which are trapped by the gravitational potential of the

central black hole and cannot escape to infinity. That is, the apparent horizon has been formed.

## A.4 accretion onto PBHs and null slicing

The determination of the mass without facing a singularity by using the null slicing [88, 242–245] is discussed in this section. In this slicing, the space-time is sliced along the null geodesics of hypothetical photons emitted from the center and reaching a distant observer. In other words, the space-time is sliced with the hyper-surfaces, each defined by a constant null coordinate $u$, the so-called observer time defined shorterly. By this construction of the null slicing, only the information outside the horizon is calculated, without looking into what happens inside the apparent horizon. The initial conditions are given on some hypersurface defined by $u$ =const., which is depicted by a blue dotted line in Figure A.4, and are obtained using the cosmic time slicing by calculating the null geodesic of a hypothetical photon which reaches a distant observer after being emitted from the center at some moment in time, while at the same time recording the physical quantities of this null geodesic [88]. As is seen in Figure A.4, in this slicing, the information can

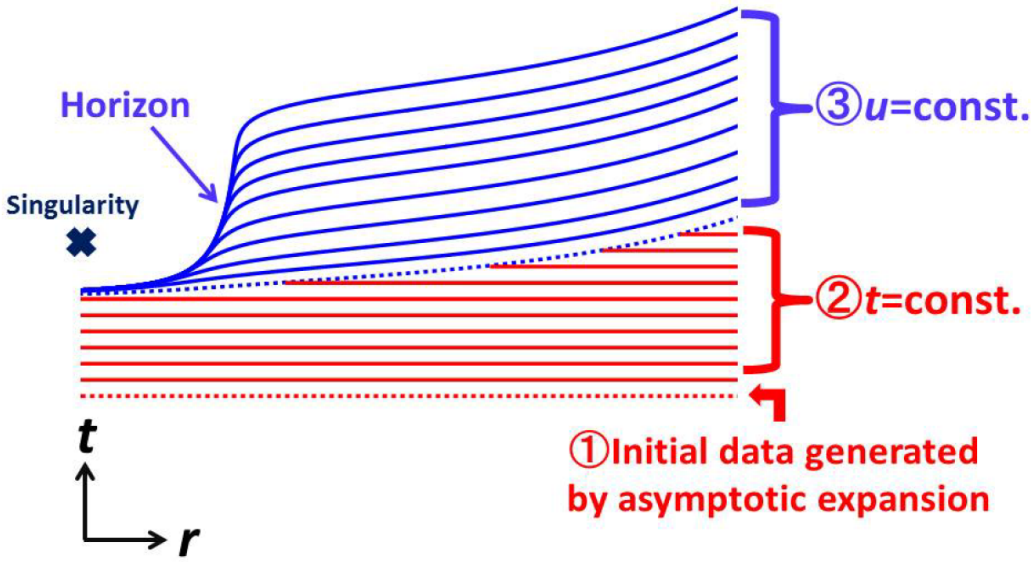


Figure A.4: Illustration of how a singularity is avoided in the null slicing.

be obtained without facing a singularity until a sufficiently later time when the eventual mass of a PBH can be determined.

Let us define the time variable $u$ by first noting

$$adt = bdr \tag{A.45}$$

along an outgoing photon. Then, $u$ is defined by

$$fdu = adt - bdr, \tag{A.46}$$

where $f$ is the lapse function and is necessary to make $du$ a perfect differential. From this definition, (A.45) holds along the hypersurfaces each defined by $u$ =const., meaning that these surfaces correspond to the null geodesics of outgoing photons. Using $u$ as the time variable then means that the space-time is sliced with the null slices. A boundary condition on the lapse function is imposed by setting $a(u, r = \infty) = f(u, r = \infty) = 1$, hence $u = t$ at the surface defined by $r = \infty$. The physical meaning of this boundary condition is that $u$ is chosen to coincide with the proper time measured by a distant observer residing at spatial infinity in the background FLRW universe. For this reason, the null slicing is also sometimes referred to as observer time slicing in the literature.

The Einstein equations in the null slicing were obtained in [242] and were later used to simulate the gravitational collapse followed by the formation of a black hole [88, 243] and recently to simulate the PBH formation as well [244, 245]. We used numerical techniques similar to those used in [88, 245]. The fundamental equations are as follows:

$$U = \frac{1}{f} R_u, \tag{A.47}$$

$$\frac{1}{f} M_u = -4\pi R^2 P U, \tag{A.48}$$

$$E_u = -P \left(\frac{1}{\nu}\right)_u, \tag{A.49}$$

$$b = \frac{1}{4\pi\nu R^2}, \tag{A.50}$$

$$\frac{1}{f} U_u = -\frac{3}{2}\left(\frac{4\pi\Gamma R^2}{w} P' + \frac{M + 4\pi R^3 P}{R^2}\right) - \frac{1}{2}\left(4\pi\nu R^2 U' + \frac{2U\Gamma}{R}\right), \tag{A.51}$$

$$\frac{1}{f}\left(\frac{1}{\nu}\right)_u = \frac{1}{\nu\Gamma}\left(\frac{2U\Gamma}{R} + 4\pi\nu R^2 U' - \frac{1}{f} U_u\right), \tag{A.52}$$

$$\frac{1}{b}\left(\frac{\Gamma + U}{f}\right)' = -4\pi R \frac{\rho + P}{f}, \tag{A.53}$$

where the subscript $u$ denotes differentiation with respect to $u$.

We now present results of numerical computations using the null slicing. The hypersurfaces of $u$ =const., corresponding to null geodesics, are shown in the top left panel of Figure A.5. Observe that the intervals between the null geodesics are tiny in the central region, meaning that time does not pass there in effect. Therefore, the formation of a singularity can be avoided in this slicing as expected. The upper lines in this figure correspond to the null geodesics of the hypothetical photons which are emitted from the center at later times and feel the effects of stronger gravity, so that they need more time to reach a distant observer. In this figure there is an envelope curve of the null geodesics, which shows approximately the location of the apparent horizon. In this way the time evolution is computed only outside the apparent horizon, so the eventual mass of a PBH can be determined without facing a singularity. From the same figure, the apparent horizon radius can be confirmed to asymptote to a constant value after its formation. This means that the black hole mass asymptotes to a constant value because $R = 2M$ on the apparent horizon, and this behavior of the mass can be confirmed by the converging curves of the mass profile in the bottom left panel of Figure A.5.

The flatness of the mass profile in later time can be understood by noting that the energy density in a region away from the center decreases due to the expansion of the universe and also due to the existence of an underdense region surrounding the central overdense region. As mentioned earlier, this behavior of the mass profile is similar to that of the vacuum inhabited by a star at the center, in which case the mass profile is a monotonically increasing function in $r$ inside the star and is flat outside.

The time evolution of $2M/R$ is shown in the bottom right panel of Figure A.5. The fact that the height of the peak of $2M/R$ saturates to unity in a late time in the null slicing is clearly seen, which is contrasted with the cosmic time slicing in which the peak is confirmed to exceed unity (see Figure A.3). This feature of the time evolution being frozen near the center in the null slicing can also be confirmed by the behavior of the lapse function, which is shown in the top right panel of Figure A.5. Thus Figure A.5 as a whole shows that using the null slicing the Einstein equations can be solved until a sufficiently late time when the eventual mass of a PBH can be determined.

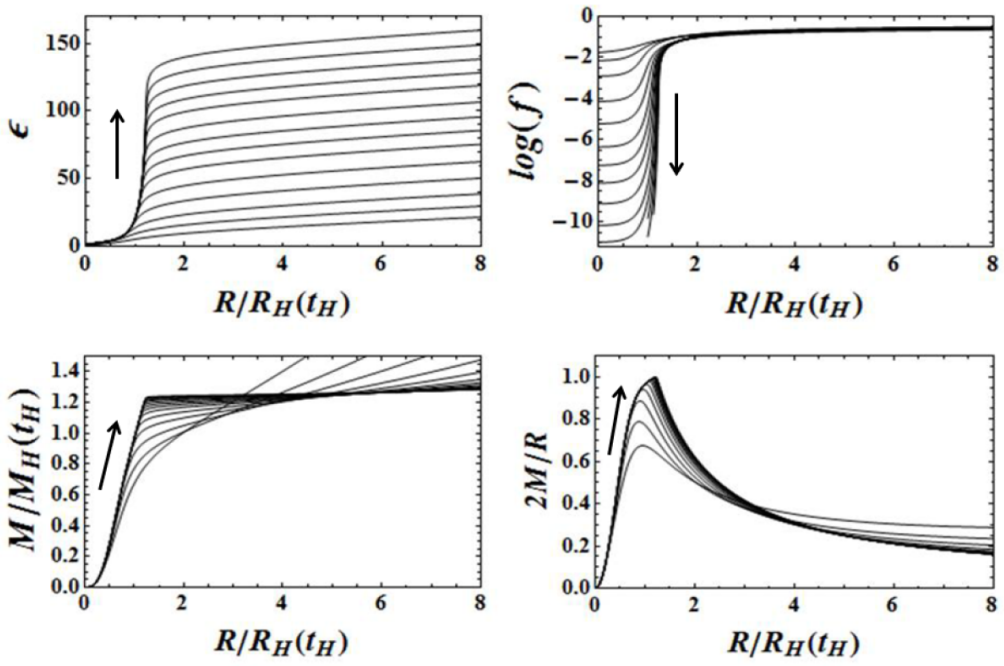


Figure A.5: Examples of time evolutions of the relevant quantities in the null slicing for the case where $(B, \sigma) = (1, 0.7)$. The horizontal line represents the circumferential radius $R$, normalized by the Hubble radius at the horizon crossing. The $u$ =const. surfaces are shown in the top left panel. Shown in the top right panel is the lapse function, which goes to zero near the center. The mass $M$ normalized by the horizon mass at the time of the horizon crossing is shown in the down left panel. The profile of $2M/R$, the height of which asymptotes to unity, is shown in the down right panel. Arrows in each figure indicate the evolution in time sequence.

## A.5 The double formation of PBHs

Suppose there exists a highly perturbed region which will collapse to form a PBH after horizon crossing, and also that this region is superposed on a much larger region, which also collapses as it enters the horizon later. Then, the collapse of the central smaller region at the time of the horizon crossing should be followed by another collapse of the larger-scale perturbation at the time of the horizon crossing of this larger-scale perturbation (double formation of PBHs). The smaller PBH, formed earlier, is involved in the second collapse leading to a larger PBH as the final state. It is expected that the first collapse is not significantly affected by the presence of the larger perturbation since it is still outside the horizon at the time of the crossing of the smaller perturbation.

In [82], the following function was introduced to parameterize various types of initial curvature profiles:

$$K_{\rm i}(r) = A\left[1 + B\left(\frac{r}{\sigma_1}\right)^{2n}\right]\exp\left[-\left(\frac{r}{\sigma_1}\right)^{2n}\right] + (1-A)\exp\left[-\left(\frac{r}{\sigma_2}\right)^{2}\right], \tag{A.54}$$

which turned out to allow us to investigate double formation. We consider a profile with $A = 0.99, B = 0, \sigma_1 = 1.45, \sigma_2 = 10\sigma_1$ and $n = 1$, depicted in Fig.A.6. In this case, the central perturbed region, represented by the first term of (A.54), is superposed on the perturbed region represented by the second term whose length scale is ten times larger than the central perturbed region. The first term itself corresponds to an initial perturbation which can collapse to form a PBH after the perturbed region $r \lesssim \sigma_1$ crosses the horizon as mentioned earlier. The perturbation represented by the second term is physically equivalent to the following profile, after a scale transformation $r \to \sqrt{1-A}r$:

$$K_{\rm i} = \exp\left[-\left(\frac{r}{\sqrt{1-A}\sigma_2}\right)^{2}\right]. \tag{A.55}$$

So when $\sqrt{1-A}\sigma_2 = \sigma_1$, which holds in the current parameter choice, the perturbation represented by the second term is equivalent to the one represented by the first. Therefore, the second term itself can also collapse to form a PBH after horizon crossing without the presence of the first term. Physically, what is expected to happen from this initial set up is that the central region, represented by the first term, collapses to form a PBH as it enters the horizon and then the larger-scale perturbation represented by the second term collapses to form a larger PBH after this scale crosses the horizon, involving the central smaller PBH already formed earlier.

We confirm this prediction by a numerical computation with the aforementioned initial curvature profile provided as the initial condition; results are shown in Fig.A.7 and A.8. First, a PBH with mass around $1.5M_{\rm H}(t_{\rm H})$, where $t_{\rm H}$ is the horizon-crossing time defined by the first term of (A.54), is formed, and then another larger PBH $\sim 100M_{\rm H}(t_{\rm H})$ is formed. Note that the mass of the smaller PBH is somewhat larger than $M_{\rm H}(t_{\rm H})$, the mass of the PBH in the previous case with $(A, B, \sigma_1, n) = (1, 0, 1.45, 1)$, even though the first term is equivalent to this case. This is due to the existence of the second term describing the larger scale perturbation, which makes the average density around the central region larger at the time of the formation of the smaller PBH. On the other hand, the mass of the larger PBH is almost 100 times larger than the previous case with $(A, B, \sigma_1, n) =$

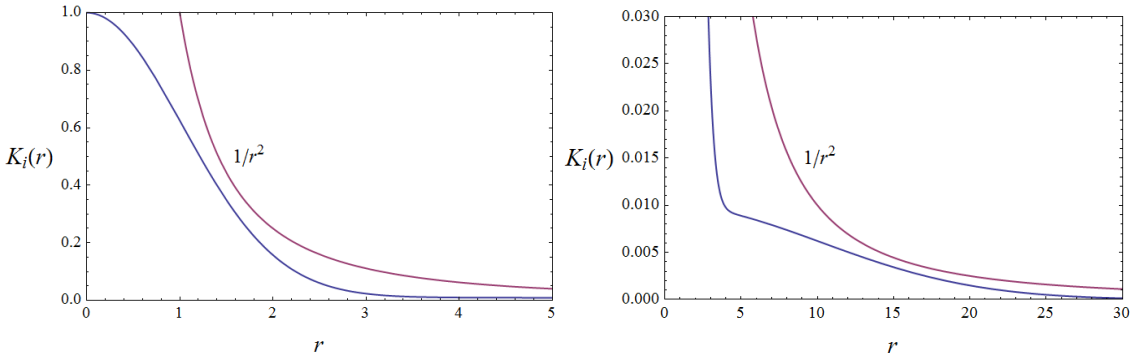


Figure A.6: The initial curvature profile eq.(A.54) with $(A, B, \sigma_1, \sigma_2, n) = (0.99, 0, 1.45, 10\sigma_1, 1)$. The left panel shows the central perturbed region represented by the first term of eq.(A.54), which is superposed on the perturbed region shown in the right panel and represented by the second term.

$(1, 0, 1.45, 1)$, which can be understood as follows. First of all, in this simulation of double formation, the radius of the overdense region $r_{\rm i}$ is defined by the first term of (A.54). So let us denote this radius by $r_{\rm i,1}$ to be contrasted with $r_{\rm i,2}$, the radius of the overdense region defined by the second term. Since $r_{\rm i,1} \propto \sigma_1$ and $r_{\rm i,2} \propto \sigma_2$, we find $r_{\rm i,2} = 10 r_{\rm i,1}$. Then, denoting the horizon crossing time defined by the first term as $t(\epsilon(r_{\rm i,1}) = 1)$, we have $t(\epsilon(r_{\rm i,2}) = 1) = 100 t(\epsilon(r_{\rm i,1}) = 1)$ from eq.(A.12). Since the Hubble radius and the horizon mass are proportional to $t$, we find $M_{\rm H}(t(\epsilon(r_{\rm i,2}) = 1)) = 100 M_{\rm H}(t(\epsilon(r_{\rm i,1}) = 1))$ as well as $R_{\rm H}(t(\epsilon(r_{\rm i,2}) = 1)) = 100 R_{\rm H}(t(\epsilon(r_{\rm i,1}) = 1))$.

## A.6 The effects of high-frequency modes

In numerical simulations of the formation of PBHs, the presence of high-frequency modes (hereafter HF modes), whose wavelength is much shorter than the perturbed region under consideration, are not taken into account [81,92,244,246,247]. HF modes, however, should exist since in principle the power spectrum of primordial curvature perturbations has an extended profile and thus affect the formation of PBHs to some extent. In this section, the effects of HF modes are discussed.

To this end, let us introduce the following initial curvature profile:

$$K_{\rm i}(r) = \exp\left[-\left(\frac{r}{\sigma_1}\right)^2\right]\left[1 + A\cos\left(\frac{r}{B\sigma_1}\right)\right]. \tag{A.56}$$

When $B < 1$, this function represents situations where a HF mode is superposed upon a perturbation of longer wavelength, as is shown in Fig.A.9.

The time evolution of the energy density perturbation of a typical case is shown in Fig.A.10. The HF mode crosses the horizon first and starts to grow before the main, or long-wavelength perturbation crosses the horizon. At this point, the main perturbation does not seem present as long as we focus on the *density* perturbation, since the density perturbation is suppressed on super-horizon scales in the comoving slicing we employ. After the horizon crossing of the main perturbation, the density perturbation with the

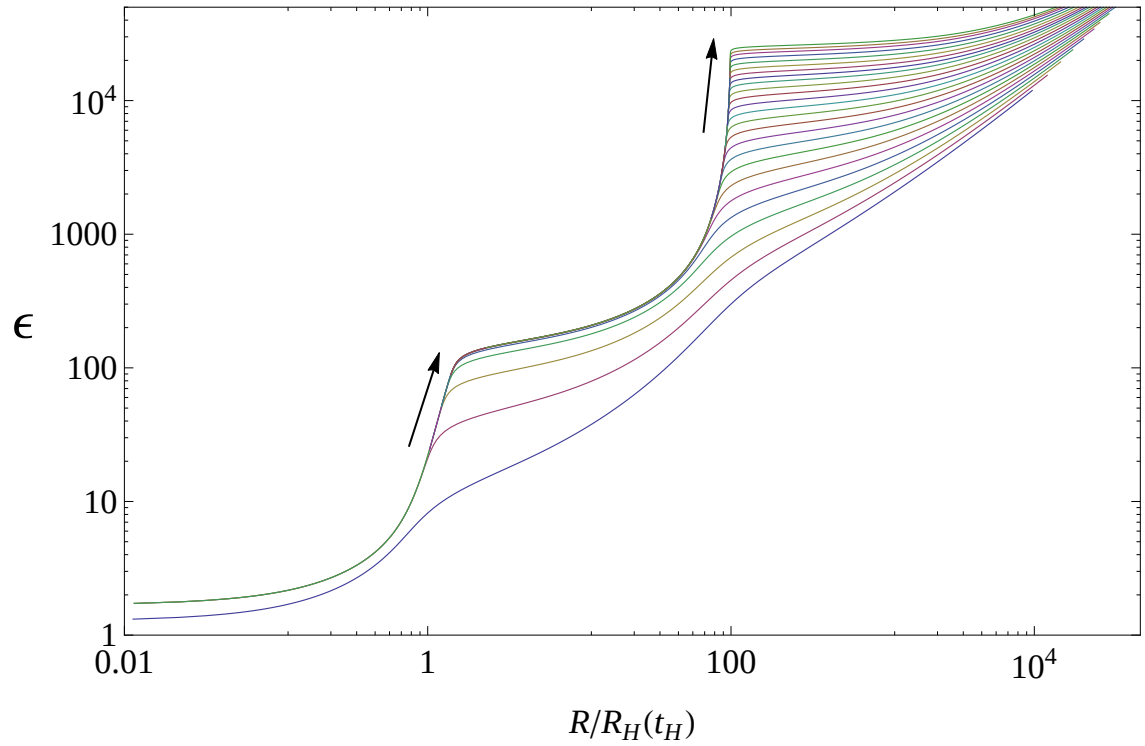


Figure A.7: Null geodesics of photons for the case of a double formation of PBHs where $(A, B, \sigma_1, \sigma_2, n) = (0.99, 0, 1.45, 10\sigma_1, 1)$. Arrows represent the direction of the time evolution. Photons emitted at later times first become almost trapped by the smaller PBH, and narrowly escape to the outer region, where they once more become almost trapped by the larger PBH before they escape to infinity.

corresponding wavelength starts to grow, and the HF mode starts to propagate towards the center due to stronger gravity in the center, resulting from the main perturbation. When a local maximum arrives at the center, it bounces, but soon it pulls back towards center once more and as a whole the energy density in the center seems to increase more rapidly than the case without the HF mode. As a result, the value of the density perturbation at the center fluctuates significantly, as is shown in Fig.5.32[†1].

For $A = 0$ (without the HF mode), the PBH is formed when $1.42 \lesssim \sigma_1$. When $A$

[†1]This makes it difficult to determine (as quickly as possible to reduce computational costs) when the perturbation is destined to die without forming a PBH, the determination which is necessary to investigate the formation condition of PBHs. Without the presence of HF modes, determining when a perturbation is destined to vanish is simple, since in this case the density perturbation at the center monotonically increases when a BH is eventually formed, and once it starts to decrease, the perturbation will definitely die so at this time one can stop numerical integration. In contrast, when a HF mode is present, one cannot conclude the perturbation will decay even if the density perturbation at the center starts to decrease, because it can be due to the presence of the HF mode, as is shown in Fig.5.32. So careful analysis is required to ensure the quasi-global decrease in the density perturbation before stopping numerical integration in cases including HF modes.

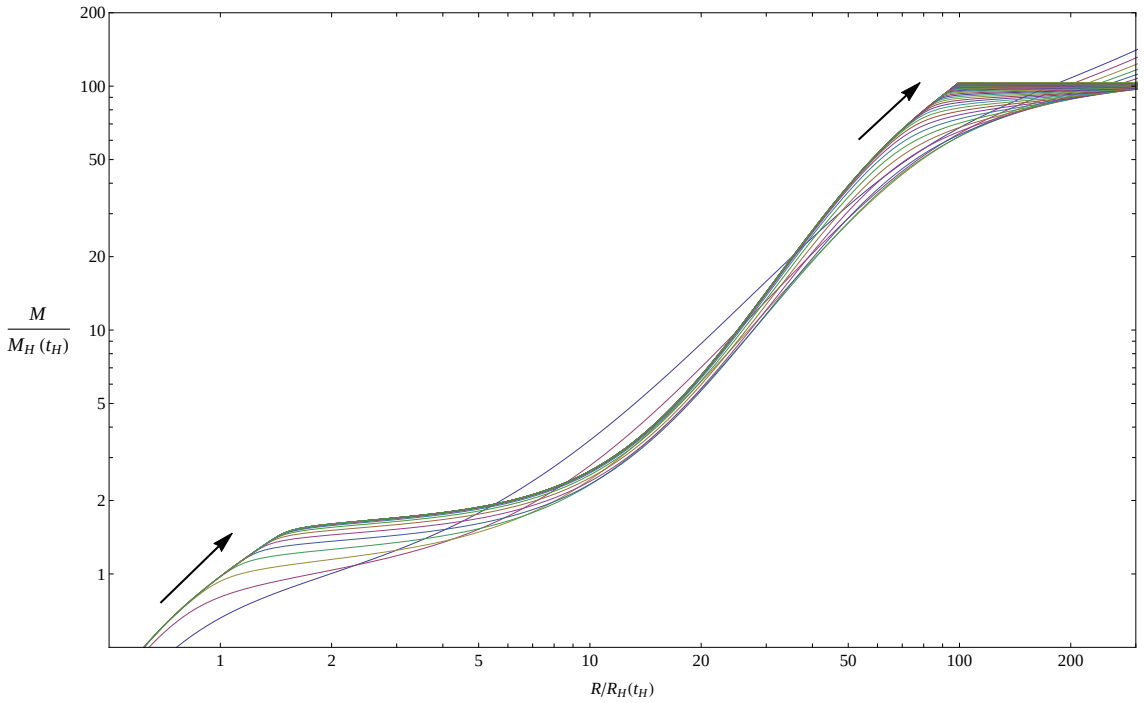


Figure A.8: The time evolution of the mass profile for the case of a double formation of PBHs where $(A, B, \sigma_1, \sigma_2, n) = (0.99, 0, 1.45, 10\sigma_1, 1)$. The arrows represent the direction of the time evolution. The two flat parts measure the mass of the smaller PBH and larger one, respectively

is larger, the threshold value decreases, implying the HF mode somewhat *facilitates* the formation of PBHs, though one may have expected the HF mode to hinder formation.

To understand why HF modes help the formation of PBHs, let us look at Fig.5.32 once more, showing the local maxima start to move towards the center after horizon crossing of the main perturbation. This behavior seems to result from strong gravity in the center due to the main perturbation. This indicates more effective transportation of radiation towards the center, which may explain the reason for the decrease in the threshold value when a HF mode is present.

It also turned out that the threshold is insensitive to the wavelength of the HF mode (confirmed in the range $0.01 < B < 0.2$), and that introducing two HF modes at the same time facilitates PBH formation somewhat more.

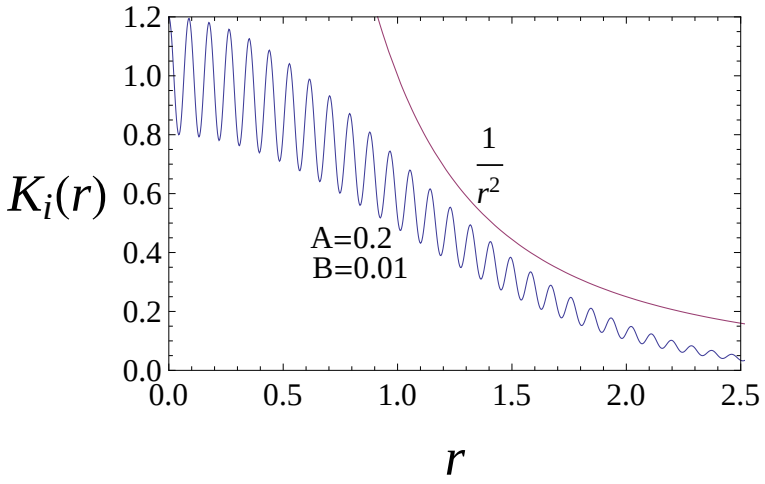


Figure A.9: An example of the initial curvature profile described by eq.(A.56).

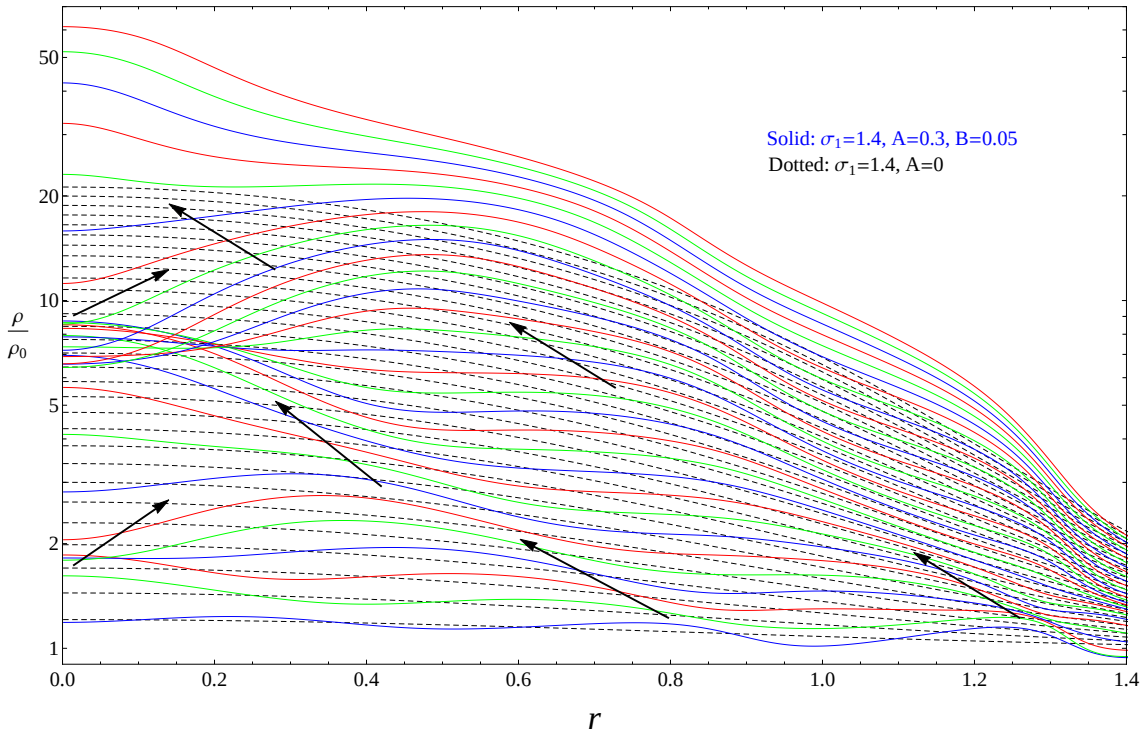


Figure A.10: An example of the time evolution of the density perturbation for a case where a PBH is eventually formed. Each curve corresponds to the density perturbation profile at $\epsilon = 0.1, 0.2, \cdots, 2.9, 3$. For comparison, the density perturbation profile for the same time sequence for a case with the same value of $\sigma_1$ but without the HF mode, in which case a PBH can not be formed, is shown by the dashed lines. The arrows indicate the direction of the fluid motion.

# Appendix B

# Dependence on non-Gaussianity of primordial perturbations of $\mu-$distortion constraints on PBHs

As is discussed in section 3.1, in [39] PBHs as the seeds of SMBHs are shown to be constrained by CMB $\mu-$distortions. That is, if PBHs with $M_{\rm PBH} \gtrsim 10^4 - 10^5 M_\odot$ formed by collapse of radiation perturbations provide the seeds of SMBHs, CMB spectral distortions larger than observational upper bounds obtained by COBE/FIRAS inevitably arise[†1]. However, there primordial perturbations are assumed to be Gaussian, and one would expect constraints obtained in [39] change for non-Gaussian cases. If non-Gaussianity is such that high-$\sigma$ peaks are suppressed, then constraints on PBHs from CMB $\mu-$distortions (and UCMHs, see the footnote †1) are even tighter, since in this case the dispersion of primordial perturbations for a fixed abundance of PBHs is larger than that in a Gaussian case. Conversely, if non-Gaussianity is such that high-$\sigma$ peaks are enhanced, then $\mu-$distortion constraints on PBHs would be relaxed, and if non-Gaussianity is sufficiently large, $\mu-$distortion constraints on PBHs would be completely evaded. This was the essence to avoid CMB distortion constraints to explain most massive SMBHs at high redshifts by PBHs, discussed in Chapter 3.

In this Appendix we show primordial perturbations have to be *tremendously* non-Gaussian, with high-$\sigma$ peaks enhanced considerably in comparison to a Gaussian case, to completely evade constraints on PBHs from CMB distortions, adopting the following class of PDFs:

$$P(\zeta) = \frac{1}{2\sqrt{2}\tilde{\sigma}\Gamma\left(1+1/p\right)} \exp\left[-\left(\frac{|\zeta|}{\sqrt{2}\tilde{\sigma}}\right)^p\right], \tag{B.1}$$

where $\tilde{\sigma}$ and $p$ are positive. That is, here we consider a monotonically decreasing PDF unlike a bimodal one considered in Chapter 3. This satisfies $\int_{-\infty}^{\infty} P(\zeta) d\zeta = 1$ and reduces to a Gaussian PDF when $p = 2$. If $p < 2$ high-$\sigma$ peaks are enhanced compared to the

[†1]Likewise, the formation of PBHs with $M_{\rm PBH} \lesssim 10^5 M_\odot$ as the potential seeds of SMBHs simultaneously leads to an abundant production of dark matter mini-halos (ultracompact mini-halos (UCMHs)) at high redshifts (say, $z \sim 1000$), which may emit standard model particles such as photons too intensely to be consistent with observed flux obtained by experiments like Fermi (see [39]). UCMHs are another probe of primordial power on small scales (see Chapter 2).

case of $p = 2$ and so we restrict our attention to $p < 2$ here. For general $p$, derivatives at $\zeta = 0$ are discontinuous and so this PDF is unphysical, but the purpose of this Appendix is to show that $\zeta$ has to be tremendously non-Gaussian for PBHs as the seed of SMBHs to avoid constraints from CMB $\mu-$distortion and UCMHs, and this toy model is convenient for that purpose. The dispersion is

$$\sigma^2 \equiv \int_{-\infty}^{\infty} \zeta^2 P(\zeta) d\zeta = \frac{2\Gamma(1+3/p)}{3\Gamma(1+1/p)} \tilde{\sigma}^2, \tag{B.2}$$

where $\Gamma(a)$ is a Gamma function. In particular, $\sigma = \tilde{\sigma}$ when $p = 2$, as it should be. The abundance of PBHs is

$$\beta = \int_{\zeta_c}^{\infty} P(\zeta) d\zeta = \frac{\Gamma(1/p, 2^{-p/2}(\zeta_c/\tilde{\sigma})^p)}{2p\Gamma(1+1/p)}, \tag{B.3}$$

where $\Gamma(a, z)$ is an incomplete Gamma function. This can be solved for $\tilde{\sigma}$ as

$$\tilde{\sigma} = \frac{2^{-1/2}\zeta_c}{Q^{-1}(1/p, 2\beta)^{1/p}}. \tag{B.4}$$

where $Q^{-1}(a, z)$ is the inverse of the regularized incomplete gamma function $Q(a, z) \equiv \Gamma(a, z)/\Gamma(a)$, namely, $z = Q^{-1}(a, s)$ if $s = Q(a, z)$. The PDF for different values of $p$ for the same $\beta = 4 \times 10^{-14}$ (see eq.(3.9)) and with $\zeta_c = 1$ is shown in Fig. B.1. Note that all the curves in this figure cross at $\zeta \sim 1$, which is expected since the integral above $\zeta_c \sim 1$ is fixed and the dominant contribution to the integral comes from $\zeta \sim 1$. In addition, the plot of $\sigma$ as a function of $p$, with $\beta$ fixed to the above value, is shown in Fig. B.2. If $p$ is smaller, the tail of PDF or the probability of PBH formation is enhanced for fixed $\sigma$, and so the value of $\sigma$, required to explain SMBHs at high redshifts by PBHs, is smaller, and if $\sigma$ is sufficiently small constraints from CMB $\mu-$distortion and UCMHs can be avoided. Let us consider constraints on PBHs obtained from CMB $\mu-$distortion following [39]. If we assume the following delta-function power spectrum (, which is conservative, see the footnote †3 of Chapter 3) leads to a sufficient probability of PBH formation,

$$\mathcal{P}_\zeta = \sigma^2 k \delta(k - k_*), \tag{B.5}$$

$\mu-$distortion generated from this spike is [121]

$$\mu \simeq 2.2\sigma^2 \left[ \exp\left( -\frac{\hat{k}_*}{5400} \right) - \exp\left( -\left[ \frac{\hat{k}_*}{31.6} \right]^2 \right) \right], \tag{B.6}$$

where $k_* = \hat{k}_* \mathrm{Mpc}^{-1}$. We adopt $\mu_{\rm upper} = 9 \times 10^{-5}$ as a $2\sigma$ upper limit obtained by COBE/FIRAS [114]. If $\mu_{\rm upper} \lesssim 2.2\sigma^2$, noting the inside of the square bracket is less than unity, there exists a range of $k_*$ excluded by CMB $\mu-$distortion. This condition yields $6.4 \times 10^{-3} \lesssim \sigma$ or $0.43 \lesssim p$ fixing $\beta$ as above, and if this is satisfied approximately a spike in the following range is excluded;

$$31.6\sqrt{-\log\left(1 - \frac{\mu_{\rm upper}}{2.2\sigma^2}\right)} \lesssim \hat{k}_* \lesssim -5400 \log\left(\frac{\mu_{\rm upper}}{2.2\sigma^2}\right). \tag{B.7}$$

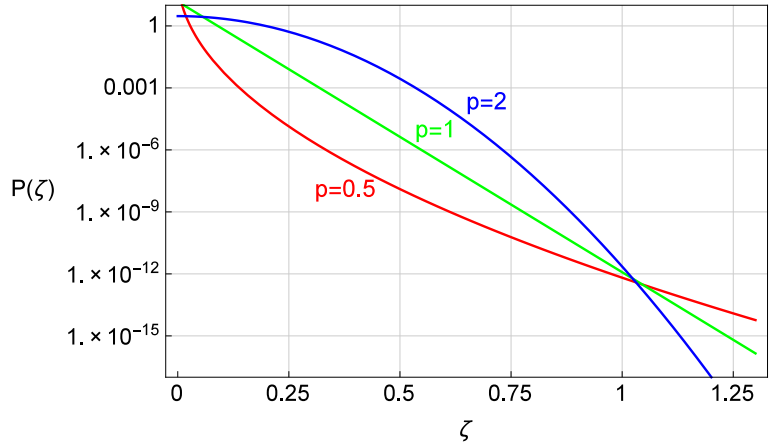


Figure B.1: The PDF of the curvature perturbation $\zeta$ for the same $\beta$ with different values of $p$ of eq.(B.1).

Noting the following relationship between $k_*$ and the typical mass of PBHs evaluated by the horizon mass when the modes with $k = k_*$ cross the horizon,

$$M_{\rm PBH} = 2.2 \times 10^{13} \left( \frac{k_*}{1{\rm Mpc}^{-1}} \right)^{-2}, \tag{B.8}$$

the above range of $\hat{k}_*$ is translated into the following range of mass of PBHs, excluded by CMB $\mu-$distortion;

$$8 \times 10^5 M_\odot \left( \log \left( \frac{\mu_{\rm upper}}{2.2\sigma^2} \right) \right)^{-2} \lesssim M_{\rm PBH} \lesssim 2 \times 10^{10} \left( -\log \left( 1 - \frac{\mu_{\rm upper}}{2.2\sigma^2} \right) \right)^{-1}. \tag{B.9}$$

The lower and upper bound here for each $p$ for the same fixed $\beta$ above is shown in Fig. B.3. Noting the logarithmic dependence of this mass range, roughly PBHs in $10^6 M_\odot \lesssim M_{\rm PBH} \lesssim 10^{10} M_{\rm PBH}$, probably the most important range for PBHs as a candidate for the seeds of SMBHs, are excluded by CMB $\mu-$distortion(, and larger PBHs are excluded by CMB $y-$distortions,) *unless* primordial perturbations are tremendously non-Gaussian ($p \lesssim 0.43$ in the toy model analyzed here), with high-$\sigma$ peaks enhanced considerably in comparison to a Gaussian case. Smaller PBHs can be potentially constrained by annihilation of dark matter inside UCMHs [39], and these potential constraints are also applicable unless primordial perturbations are tremendously non-Gaussian. If such a highly non-Gaussian and monotonically decreasing PDF for $0 \lesssim \zeta$ can be indeed realized in some model of inflation, such a model can also explain SMBHs by PBHs, evading constraints from CMB distortions or UCMHs. Be reminded that in Chapter 3 we have constructed models leading to a bimodal PDF (see Fig. 3.1) to explain SMBHs by PBHs.

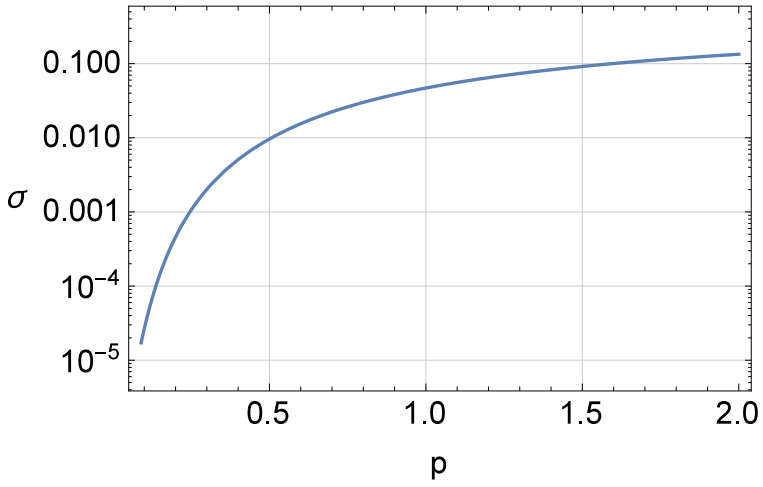


Figure B.2: The root mean square $\sigma$ of $\zeta$ for each $p$, required to produce a desirable amount of PBHs to explain SMBHs at high redshifts.

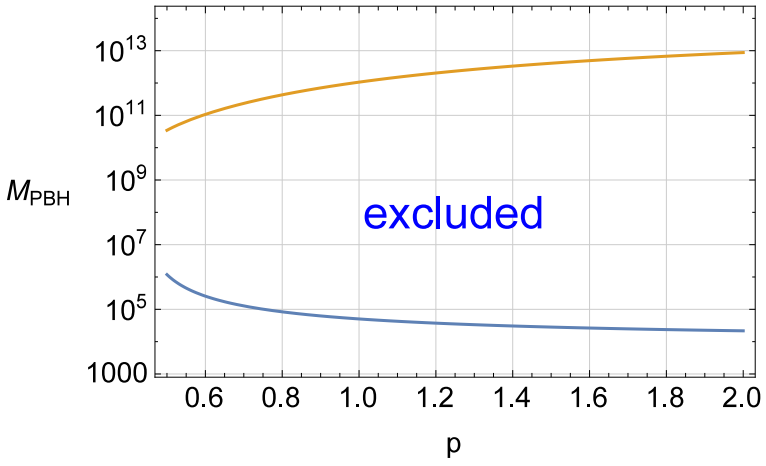


Figure B.3: The lower and upper bound of eq.(B.9) for each $p$. The region between the curves corresponds to the mass of PBHs excluded by CMB $\mu-$distortion.

# Appendix C

# Brief review of $\delta$N formalism

Let us briefly review $\delta N$ formalism following [51], where the following form of the metric is adopted:

$$ds^2 = -\mathcal{N}^2 dt^2 + \gamma_{ij}(dx^i + \beta^i dt)(dx^j + \beta^j dt). \tag{C.1}$$

The 3-metric $\gamma_{ij}$ is decomposed as $\gamma_{ij} \equiv e^{2\alpha}\tilde{\gamma}_{ij}$, where $\det[\tilde{\gamma}_{ij}] = 1$. Here, $\tilde{a} \equiv e^{\alpha}$ can be regarded as the locally-defined scale factor. We further decompose $e^{\alpha} = a(t)e^{\psi(t,x^i)}$, where $a(t)$ represents the homogeneous, global scale factor and $\psi(t, x^i)$ represents the inhomogeneity of the scale factor, or of the expansion of the universe.

In the gradient expansion approach, a fictitious parameter $\epsilon$ is put in front of the spatial gradients, and the equations are expanded in powers of $\epsilon$, and finally $\epsilon$ is set to unity. The parameter $\epsilon$ is identified as $\epsilon = k/aH$. In the limit $\epsilon \to 0$, the region with comoving length significantly smaller than $\sim k^{-1}$ but larger than the Hubble radius is assumed to be regarded as locally homogeneous and isotropic (FLRW universe).

In [51] the spatial coordinates which comove with the fluid are used, namely, the threads $x^i$ =const. coincide with the integral curves of the fluid 4-velocity $u^\mu$, or the comoving world lines, and so $u^i = 0$. Note that the gauge is fully specified by the choice of the slicing on top of the threading. In the uniform-density slicing, $\psi$ is denoted by $-\zeta$. They also considered the uniform Hubble slicing, and the comoving slicing, which is orthogonal to the comoving world lines. The specifications of the comoving threading and comoving slicing fully detemine the gauge, and this gauge is called comoving gauge. They show that these three slicings coincide with each other to $\mathcal{O}(\epsilon)$, from the conservation of the energy-momentum tensor.

The unit time-like vector normal to $t$ =const. hypersurfaces is denoted by $n^\mu$, and then $\tilde{H} = \nabla_\mu n^\mu/3$ can be interpreted as the local Hubble parameter:

$$\tilde{H} = \frac{1}{\mathcal{N}}\left(\frac{\dot{a}}{a} + \dot{\psi}\right) + \mathcal{O}(\epsilon^2), \tag{C.2}$$

with which the local Friedmann equation is recovered from the Einstein equations. Let us define the number of e-folds of expansion along a comoving world line:

$$N(t_2, t_1; x^i) = \int_{t_1}^{t_2} \tilde{H}\mathcal{N} dt. \tag{C.3}$$

Then,

$$\psi(t_2, x^i) - \psi(t_1, x^i) = N(t_2, t_1; x^i) - N_0(t_2, t_1), \quad N_0(t_2, t_1) \equiv \log\left[\frac{a(t_2)}{a(t_1)}\right]. \tag{C.4}$$

That is, the time evolution of $\psi$ is given by the difference of the number of e-folds of expansion at that location from the background value. Let $A$ denote the slicing which starts on a flat slice at $t_1$ and ends on a uniform-density slice at $t_2$, then we find

$$\psi_A(t_2, x^i) = N_A(t_2, t_1; x^i) - N_0(t_2, t_1), \tag{C.5}$$

which is the difference in the e-folds from $t_1$ to $t_2$ between the uniform-density slicing and flat slicing. In the case of $P = P(\rho)$, they find

$$\psi(t_2, x^i) - \psi(t_1, x^i) = -\log\left[\frac{a(t_2)}{a(t_1)}\right] - \frac{1}{3}\int_{\rho(t_1,x^i)}^{\rho(t_2,x^i)} \frac{d\rho}{\rho + P}, \tag{C.6}$$

which leads to a conserved quantity, independent of the slicing:

$$-\zeta = \psi(t, x^i) + \frac{1}{3}\int_{\rho(t)}^{\rho(t,x^i)} \frac{d\rho}{\rho + P}. \tag{C.7}$$

In the limit of the linear theory, this reduces to the conserved curvature perturbation in the three slicings mentioned above:

$$-\zeta(x^i) = \mathcal{R}_c(x^i) = \psi(t, x^i) + \frac{\delta\rho(t, x^i)}{3(\rho + P)}. \tag{C.8}$$

They note that these results also apply to arbitrary threading.

# Appendix D

# Einstein equations for induced scalar perturbations originating from second-order tensor perturbations

In this appendix we derive our fundamental equations for scalar perturbations induced by second-order tensor perturbations. We have also checked the expressions below by a package for Mathematica, xPand [248].

## D.1 Scalar perturbation

We use the formulation of [231], in which the metric was decomposed as[†1]

$$g_{\mu\nu} = \bar{g}_{\mu\nu} + h_{\mu\nu}, \tag{D.1}$$

$$\bar{g}_{00} = -1, \quad \bar{g}_{i0} = \bar{g}_{0i} = 0, \quad \bar{g}_{ij} = a^2\delta_{ij}. \tag{D.2}$$

The components of the perturbed Ricci tensor are expressed in terms of $h_{\mu\nu}$ as [231][†2]:

$$\begin{aligned}\delta R_{jk} =& -\frac{1}{2}h_{00,jk} - (2\dot{a}^2 + a\ddot{a})h_{00}\delta_{jk} - \frac{1}{2}a\dot{a}\dot{h}_{00}\delta_{jk} \\ &+ \frac{1}{2a^2}(\Delta h_{jk} - h_{ik,ij} - h_{ij,ik} + h_{ii,jk}) \\ &- \frac{1}{2}\ddot{h}_{jk} + \frac{\dot{a}}{2a}(\dot{h}_{jk} - \dot{h}_{ii}\delta_{jk}) + \frac{\dot{a}^2}{a^2}(-2h_{jk} + h_{ii}\delta_{jk}) + \frac{\dot{a}}{a}h_{i0,i}\delta_{jk} \\ &+ \frac{1}{2}(\dot{h}_{k0,j} + \dot{h}_{j0,k}) + \frac{\dot{a}}{2a}(h_{k0,j} + h_{j0,k}),\end{aligned} \tag{D.5}$$

[†1] $h_{\mu\nu}$ here is not to be confused with tensor perturbations $h_{ij}$ in (5.9) and (D.18).

[†2] In [231] the Ricci tensor is defined by

$$R_{\mu\nu} \equiv \Gamma^{\lambda}_{\mu\lambda,\nu} - \Gamma^{\lambda}_{\mu\nu,\lambda} + \Gamma^{\kappa}_{\mu\lambda}\Gamma^{\lambda}_{\nu\kappa} - \Gamma^{\kappa}_{\mu\nu}\Gamma^{\lambda}_{\lambda\kappa}. \tag{D.3}$$

With this definition, the Einstein equations are written as

$$R_{\mu\nu} - \frac{1}{2}g_{\mu\nu}R = -8\pi G T_{\mu\nu}. \tag{D.4}$$

If we adopt another definition of the Ricci tensor, which is minus that of (D.3), then the sign of the right hand side of the Einstein equations should be flipped. We adopt the former definition in this section following [231], but in the next section we adopt the latter definition.

$$\delta R_{0j} = \delta R_{j0} = \frac{\dot{a}}{a} h_{00,j} + \frac{1}{2a^2}(\Delta h_{j0} - h_{i0,ji}) - \left(\frac{\ddot{a}}{a} + \frac{2\dot{a}^2}{a^2}\right) h_{j0} + \frac{1}{2}\frac{\partial}{\partial t}\left[\frac{1}{a^2}(h_{kk,j} - h_{kj,k})\right], \tag{D.6}$$

$$\delta R_{00} = \frac{1}{2a^2}\Delta h_{00} + \frac{3\dot{a}}{2a}\dot{h}_{00} - \frac{1}{a^2}\dot{h}_{i0,i} + \frac{1}{2a^2}\left[\ddot{h}_{ii} - \frac{2\dot{a}}{a}\dot{h}_{ii} + 2\left(\frac{\dot{a}^2}{a^2} - \frac{\ddot{a}}{a}\right) h_{ii}\right]. \tag{D.7}$$

The components of the Ricci tensor with mixed indices are expressed in terms of those with doubly covariant indices as follows:

$$\delta R^0_0 = -3\frac{\ddot{a}}{a} h_{00} - \delta R_{00}, \tag{D.8}$$

$$\delta R^0_i = -\delta R_{0i} - a^{-2}(2\dot{a}^2 + a\ddot{a}) h_{i0}, \tag{D.9}$$

$$\delta R^i_j = a^{-2}\left(2H^2 + \frac{\ddot{a}}{a}\right) h_{ij} + \frac{1}{a^2}\delta R_{ij}. \tag{D.10}$$

Using these, the Ricci scalar can be calculated as

$$a^2\delta R = -3a\dot{a}\dot{h}_{00} - 6(\dot{a}^2 + a\ddot{a}) h_{00} - \Delta h_{00} + 2\dot{h}_{i0,i} + 4H h_{i0,i} - \ddot{h}_{ij} + \frac{2}{3a^2}\Delta h_{ii} + 2\left(H^2 + \frac{\ddot{a}}{a}\right) h_{ii}. \tag{D.11}$$

In our notation of (5.9),

$$h_{00} = -2\Phi\ , \quad h_{i0} = aB_{,i}\ , \quad h_{ii} = -6a^2\Psi\ . \tag{D.12}$$

The time-time component of the Einstein tensor becomes

$$\frac{a^2}{2} G^0_0 = \Delta\Psi - 3\mathcal{H}(\Psi' + \mathcal{H}^2\Phi) - \mathcal{H}\Delta B = \frac{a^2}{2}[-8\pi G(-\delta\rho)], \tag{D.13}$$

which recovers the parts of (5.14) involving scalar perturbations. The time-space component is

$$G^0_i = R^0_i = -\delta R_{0i} - a^{-2}(2\dot{a}^2 + a\ddot{a}) h_{i0} = 2\dot{\Psi}_{,i} + 2H\Phi_{,i}. \tag{D.14}$$

So $aG^0_i/2 = 0$ partially recovers (5.15). The space-space components are

$$\delta G^i_j = a^{-2}\left(2H^2 + \frac{\ddot{a}}{a}\right) h_{ij} + \frac{1}{a^2}\delta R_{ij} - \frac{1}{2}\delta R\delta_{ij}, \tag{D.15}$$

and this is written in the form $\delta G^i_j = G_1\delta_{ij} + G_{2,ij}$, where

$$-\frac{a^2}{2} G_1 = \Psi'' + \mathcal{H}(2\Psi + \Phi)' + (2\mathcal{H}' + \mathcal{H}^2)\Phi + \frac{1}{2}\Delta(\Phi - \Psi + B' + 2\mathcal{H}B), \tag{D.16}$$

$$a^2 G_2 = \Phi - \Psi + B' + 2\mathcal{H}B. \tag{D.17}$$

Then, $-a^2 G_1/2 = -a^2(-8\pi G\delta p)/2$ partially recovers (5.16), and $a^2 G_{2,ij} = 0$ partially recovers (5.17). (5.28) and (5.29) without the source term can also be derived from (5.1.49) and (5.1.48) of [231][†3].

[†3]One can also confirm dropping the source terms originating from second-order tensor perturbations, eqs. (5.14)-(5.17), (5.28) and (5.29) reduce to eqs. (A.98)-(A.103) of [249].

## D.2 Tensor perturbation

Let us consider the following metric

$$ds^2 = a^2(\eta)[-d\eta^2 + a^2(\delta_{ij} + h_{ij})dx^i dx^j]. \tag{D.18}$$

The definition of $h_{ij}$ here is different from that in (5.9) by the factor two for simplicity. We decompose the metric (and other tensors below) as $g_{ij} = \bar{g}_{ij} + \delta g_{ij} + \delta^2 g_{ij}$, with $\bar{g}_{ij} = a^2\delta_{ij}, \delta g_{ij} = a^2 h_{ij}, \delta^2 g_{ij} = 0$. Then, $\bar{g}^{ij} = a^{-2}\delta_{ij}, \delta g_{ij} = -a^2 h_{ij}, \delta^2 g^{ij} = h^{ik}h^j_k$. The indices of $h_{ij}$ are raised and lowered by $\delta_{ij}$. The non-vanishing components of the Christoffel symbol are

$$\bar{\Gamma}^0_{00} = \mathcal{H}, \tag{D.19}$$

$$\bar{\Gamma}^0_{ij} = \mathcal{H}\delta_{ij}, \tag{D.20}$$

$$\delta\Gamma^0_{ij} = \frac{1}{2}(h'_{ij} + 2\mathcal{H}h_{ij}), \tag{D.21}$$

$$\bar{\Gamma}^i_{j0} = \mathcal{H}\delta_{ij}, \tag{D.22}$$

$$\delta\Gamma^i_{j0} = \frac{1}{2}h^{i'}_j, \tag{D.23}$$

$$\delta^2\Gamma^i_{j0} = -\frac{1}{2}h^{ik}h'_{kj}, \tag{D.24}$$

$$\delta\Gamma^i_{jk} = \frac{1}{2}(h_{ij,k} + h_{ik,j} - h_{jk,i}), \tag{D.25}$$

$$\delta^2\Gamma^i_{jk} = \frac{1}{2}h^{il}(h_{lj,k} + h_{lk,j} - h_{jk,l}). \tag{D.26}$$

The components of the Ricci tensor are

$$\delta^2 R_{00} = \frac{1}{2}h^{ij}h''_{ij} + \frac{1}{4}h^{ij'}h'_{ij} + \frac{1}{2}\mathcal{H}h^{ij}h'_{ij}, \tag{D.27}$$

$$\delta^2 R_{i0} = \frac{1}{4}h^{jk'}h_{jk,i} + \frac{1}{2}h^{jk}h'_{jk,i} - \frac{1}{2}h^{jk}h'_{ij,k}, \tag{D.28}$$

$$\bar{R}_{ij} = (\mathcal{H}' + 2\mathcal{H}^2)\delta_{ij}, \tag{D.29}$$

$$\delta R_{ij} = \frac{1}{2}h''_{ij} + \mathcal{H}h'_{ij} + (\mathcal{H}' + 2\mathcal{H}^2)h_{ij} - \frac{1}{2}\Delta h_{ij}, \tag{D.30}$$

$$\begin{aligned}\delta^2 R_{ij} = -\frac{\mathcal{H}}{2}h^{kl}h'_{kl}\delta_{ij} - \frac{1}{2}h^{k'}_i h'_{kj} + \frac{1}{2}h^{kl}(h_{ij,kl} - h_{ik,jl} - h_{jk,il}) + \frac{1}{2}h^{kl}h_{kl,ij} \\ + \frac{1}{4}h^{kl}_{\ ,i}h_{kl,j} + \frac{1}{2}h^{k,l}_i h_{jk,l} - \frac{1}{2}h^{k,l}_i h_{jl,k}.\end{aligned} \tag{D.31}$$

The components of the Ricci tensor with mixed indices are given by

$$\delta^2 R^0_0 = -a^{-2}\delta^2 R_{00}, \tag{D.32}$$

$$\delta^2 R^0_i = -a^{-2}\delta^2 R_{0i}, \tag{D.33}$$

$$\delta^2 R^i_j = \delta^2 g^{ik}\bar{R}_{kj} + \delta g^{ik}\delta R_{kj} + a^{-2}\delta^2 R_{ij}. \tag{D.34}$$

The Ricci scalar can be written as

$$\delta^2 R = -a^{-2}\delta^2 R_{00} + a^{-2}\delta^2 R_{ii} + \delta g^{ij}\delta R_{ij} + \delta^2 g^{ij}\bar{R}_{ij}, \tag{D.35}$$

which leads to

$$a^2\delta^2 R = -h^{ij}h''_{ij} - \frac{3}{4}h^{ij'}h'_{ij} - 3\mathcal{H}h^{ij}h'_{ij} + h^{ij}\Delta h_{ij} + \frac{3}{4}h^{ij,k}h_{ij,k} - \frac{1}{2}h^{ij,k}h_{ik,j}. \tag{D.36}$$

The components of the Einstein tensor are (hereafter we replace $h_{ij} \to 2h_{ij}$)

$$-\frac{a^2}{2}\delta^2 G^0_0 = S_1, \tag{D.37}$$

$$\delta^2 G^i_0 = -\delta^2 G^0_i = a^{-2}\delta^2 R_{i0} = \frac{2S_i}{a^2}, \tag{D.38}$$

$$a^2\delta^2 G^i_j = a^2(\delta^2 g^{ik}\bar{R}_{kj} + \delta g^{ik}\delta R_{kj} + a^{-2}\delta^2 R_{ij}) = 2S_3\delta_{ij} + 2S_{ij}. \tag{D.39}$$

Eqs. (D.13) and (D.37) recover (5.14) (see the footnote †2 in the previous section). Also, Eqs. (D.14) and (D.38) recover (5.15)[†4]. Let us decompose $S_{ij}$ as $S_{ij} = S_4\delta_{ij} + S_{5,ij} + \cdots$, where $\cdots$ is to contain vector and tensor parts, which are irrelevant here. From this, we find $\Delta S^i_i = 3\Delta S_4 + \Delta^2 S_5$ and $S^{ij}{}_{,ij} = \Delta S_4 + \Delta^2 S_5$, which lead to (5.22) and (5.23). Then we find (5.16) and (5.17) from (D.16), (D.17) and (D.39).

The second-order parts of the divergence of the energy momentum tensor are

$$\delta^2 T^\mu_{\nu;\mu} = \delta^2\Gamma^\mu_{\mu\lambda}\bar{T}^\lambda_\nu - \delta^2\Gamma^\lambda_{\mu\nu}\bar{T}^\mu_\lambda, \tag{D.40}$$

which is non-zero when $\nu = 0$:

$$\delta^2 T^\mu_{0;\mu} = 2(\rho + p)h^{ij}h'_{ij}. \tag{D.41}$$

The negative of this gives the source term of (5.28).

[†4]Note that the indices "0" indicate $t$ in the previous subsection, while those indicate the conformal time $\eta$ in this subsection, and they are related by $G^t_i = aG^\eta_i$.

# Appendix E

# Derivation of the source term for the curvature perturbation in the Fourier space

In this Appendix we derive (5.55) and (5.56). First, note that the Fourier components of $h^{ij}h_{ij}$ become

$$(h^{ij}h_{ij})(\eta,\boldsymbol{k}) = \int \frac{d^3\boldsymbol{k}'}{(2\pi)^{3/2}} \sum_{rs} h^r(\boldsymbol{k}')h^s(\boldsymbol{k}-\boldsymbol{k}')D(\eta,k')E^{ij}_{rs\,ij}(\boldsymbol{k},\boldsymbol{k}')D(\eta,|\boldsymbol{k}-\boldsymbol{k}'|). \quad \text{(E.1)}$$

Similarly, the source can be written in the following form:

$$S(\eta,\boldsymbol{k}) = \int \frac{d^3\boldsymbol{k}'}{(2\pi)^{3/2}} \sum_{rs} h^r(\boldsymbol{k}')h^s(\boldsymbol{k}-\boldsymbol{k}')D(\eta,k')(\cdots)D(\eta,|\boldsymbol{k}-\boldsymbol{k}'|). \quad \text{(E.2)}$$

In the following, let us consider the contribution of each term to $(\cdots)$ in the above expression. The contribution of the term $\partial_j h_{ik}\partial^k h^{ij} = \partial_j\partial^k(h_{ik}h^{ij})$ in (E.5) to $(\cdots)$, indicated after the arrow in the equation below (the arrows elsewhere should be understood similarly), is

$$\partial_j h_{ik}\partial^k h^{ij} = \partial_j\partial^k(h_{ik}h^{ij}) \quad \to \quad -k^2 E_1^{rs}. \quad \text{(E.3)}$$

Similarly,

$$\partial_k h_{ij}\partial^k h^{ij} = \frac{1}{2}\partial_k\partial^k(h_{ij}h^{ij}) - (\Delta h_{ij})h^{ij} \quad \to \quad -\frac{1}{2}k^2 E_2^{rs} + k'^2 E_2^{rs}. \quad \text{(E.4)}$$

So the contribution of $S_1$ is

$$S_1 \quad \to \quad \left(-\frac{1}{4}\overleftarrow{\partial_\eta}\partial_\eta + \partial_\eta^2 - \frac{3}{8}k^2 + \frac{3}{4}k'^2\right) E_2^{rs} + \frac{k^2}{2}E_1^{rs}, \quad \text{(E.5)}$$

where $\overleftarrow{\partial_\eta}$ is supposed to differentiate *only* $D(\eta,k')$ of eq.(E.2) in the left. Likewise, the contribution of $S_3$ is

$$S_3 \quad \to \quad \left(\frac{3}{4}\overleftarrow{\partial_\eta}\partial_\eta + \frac{3}{8}k^2 - \frac{3}{4}k'^2\right) E_2^{rs} - \frac{k^2}{2}E_1^{rs}. \quad \text{(E.6)}$$

To obtain the contribution of $\hat{k}^i\hat{k}^j S_{ij}$, let us rewrite $S_{ij}$ as follows:

$$S_{ij} = -h_i{}^{k'}h'_{jk} + \partial_k\partial_l(h^{kl}h_{ij}) - \partial_l(h^{kl}\partial_i h_{jk}) - (i \leftrightarrow j) - \partial_k\partial^l(h_{jl}h_i{}^k) \\ +\partial_l h_{jk}\partial^l h_i{}^k + \frac{1}{2}\partial_i\partial_j(h^{kl}h_{kl}) - \frac{1}{2}\partial_i h^{kl}\partial_j h_{kl}. \tag{E.7}$$

Then, the contribution is

$$\begin{aligned} S_{ij}\hat{k}^i\hat{k}^j \quad \to \quad & -\overleftarrow{\partial_\eta}\partial_\eta E_i{}^k{}_{jk}\hat{k}^i\hat{k}^j - k_k k_l E^{kl}{}_{ij}\hat{k}^i\hat{k}^j + 2k_l(k_i - k'_i)E^{kl}{}_{jk}\hat{k}^i\hat{k}^j \\ & +k_k k^l E_{jli}{}^k\hat{k}^i\hat{k}^j - k'_l(k^l - k'^l)E_{jki}{}^k\hat{k}^i\hat{k}^j - \frac{1}{2}k_i k_j\hat{k}^i\hat{k}^j E^{kl}{}_{kl} \\ & +\frac{1}{2}k'_i(k_j - k'_j)E^{kl}{}_{kl}\hat{k}^i\hat{k}^j \\ = {} & (-\overleftarrow{\partial_\eta}\partial_\eta + 2k^2 - 3kk'\mu + k'^2)E_1^{rs} + \frac{1}{2}(k'\mu(k - k'\mu) - k^2)E_2^{rs}. \end{aligned} \tag{E.8}$$

The collection of all the contributions yields

$$\begin{aligned} S \quad \to \quad & \left\{\overleftarrow{\partial_\eta}\partial_\eta - \frac{1}{2}(3 - c_{\rm s}^2)k^2 + 3kk'\mu - k'^2\right\}E_1^{rs} + \\ & \left\{-\frac{1}{4}(3 + c_{\rm s}^2)\overleftarrow{\partial_\eta}\partial_\eta + c_{\rm s}^2\partial_\eta^2 + 2c_{\rm s}^2\mathcal{H}\partial_\eta + \frac{1}{8}(1 - 3c_{\rm s}^2)k^2 - \frac{1}{2}k'\mu(k - k'\mu) + \frac{3}{4}(1 + c_{\rm s}^2)k'^2\right\}E_2^{rs}, \end{aligned} \tag{E.9}$$

from which (5.55) and (5.56) can be read off.

# Appendix F

# Numerical calculation of the PDF of the induced density perturbations

In this Appendix, the numerical calculation of PDF is discussed. Recall that $\mathcal{P}_h(k)$ is assumed to be delta-function (see (5.59)) and is approximated by the following top-hat in the simulation:

$$\mathcal{P}_h(k) = \mathcal{A}^2\epsilon^{-1}\left(k_p\left(1-\frac{\epsilon}{2}\right) < k < k_p\left(1+\frac{\epsilon}{2}\right)\right), \quad 0(\text{otherwise}). \tag{F.1}$$

In this Appendix, we set $\mathcal{A} = 1$.

Let us decompose the Fourier components of $h^r(\boldsymbol{k})$ as follows:

$$h^r(\boldsymbol{k}) = a^r(\boldsymbol{k}) + ib^r(\boldsymbol{k}), \tag{F.2}$$

where $a^r$ and $b^r$ are real Gaussian random variables satisfying

$$a^+(-\boldsymbol{k}) = a^+(\boldsymbol{k}), \quad b^+(-\boldsymbol{k}) = -b^+(\boldsymbol{k}), \quad a^\times(-\boldsymbol{k}) = -a^\times(\boldsymbol{k}), \quad b^\times(-\boldsymbol{k}) = b^\times(\boldsymbol{k}) \tag{F.3}$$

to ensure the reality of $h_{ij}(\eta, \boldsymbol{x})$ (note that $e^\times_{ij}(-\boldsymbol{k}) = -e^\times_{ij}(\boldsymbol{k})$ as well as $e^+_{ij}(-\boldsymbol{k}) = e^+_{ij}(\boldsymbol{k})$ following the definitions of polarization tensors we adopt). In Monte Carlo simulations, we consider a spherical shell in the Fourier space whose radius is $k_p$ and whose width is $\epsilon k_p$. Let us call the grid points in this sphere by $\boldsymbol{k}_i$, where $i$ is a natural number. Each grid point in this sphere is associated with two complex numbers $h^r(\boldsymbol{k}_i) = a^r(\boldsymbol{k}_i) + ib^r(\boldsymbol{k}_i), (r = +, \times)$ (satisfying $h^+(-\boldsymbol{k}_i) = h^+(\boldsymbol{k}_i)^*, h^\times(-\boldsymbol{k}_i) = -h^\times(\boldsymbol{k}_i)^*$), where the dispersion of both $a^r$ and $b^r$ is given by

$$\sigma^2 = \frac{\pi^2}{k_p^3} dk^{-3}\epsilon^{-1}, \tag{F.4}$$

with $dk$ denoting the interval between two neighboring grid points in the Fourier space. Then, $\delta_r(\eta, \boldsymbol{x} = 0, R)$ for a specific realization of $\{h^r(\boldsymbol{k}_i)\}$ is calculated by

$$\delta_r(\eta, \boldsymbol{x} = 0, R) = \frac{1+c_{\rm s}^2}{c_{\rm s}^2\mathcal{H}}\frac{dk^6}{(2\pi)^3}\left\{\sum_{r,s}\sum_{\boldsymbol{k}_i,\boldsymbol{k}_j\in S} W(|\boldsymbol{k}_i+\boldsymbol{k}_j|R)h^r(\boldsymbol{k}_i)h^s(\boldsymbol{k}_j)F_{rs}(\eta, \boldsymbol{k}_i+\boldsymbol{k}_j, \boldsymbol{k}_i)\right\}, \tag{F.5}$$

where $S$ denotes the set comprised of the grid points inside the spherical shell. As mentioned in the main text, we set $\eta = R = (0.7k_p)^{-1}$. Note that in simulations eqs.

(5.48)-(5.51) can not be used to consistently associate each $\boldsymbol{k}$ mode with + and × polarization states. Instead, one may use the following expressions to calculate $E_1^{rs}$ and $E_2^{rs}$ for each $\boldsymbol{k}_i$[†1]:

$$e_{ij}^{+}(\hat{k}) = \begin{pmatrix} 1 & 0 & 0 \\ 0 & -1 & 0 \\ 0 & 0 & 0 \end{pmatrix} (|\hat{k}_3| = 1), \quad \begin{pmatrix} \frac{\hat{k}_3^2 - \hat{k}_3^4 - \hat{k}_2^2(1+\hat{k}_3^2)}{-1+\hat{k}_3^2} & \frac{\hat{k}_1\hat{k}_2(1+\hat{k}_3^2)}{-1+\hat{k}_3^2} & \hat{k}_1\hat{k}_3 \\ \frac{\hat{k}_1\hat{k}_2(1+\hat{k}_3^2)}{-1+\hat{k}_3^2} & \frac{-1+\hat{k}_3^2+\hat{k}_2^2(1+\hat{k}_3^2)}{-1+\hat{k}_3^2} & \hat{k}_2\hat{k}_3 \\ \hat{k}_1\hat{k}_3 & \hat{k}_2\hat{k}_3 & -1+\hat{k}_3^2 \end{pmatrix} (|\hat{k}_3| \neq 1), \tag{F.6}$$

$$e_{ij}^{\times}(\hat{k}) = \pm \begin{pmatrix} 0 & 1 & 0 \\ 1 & 0 & 0 \\ 0 & 0 & 0 \end{pmatrix} (\hat{k}_3 = \pm 1), \quad \begin{pmatrix} -\frac{2\hat{k}_1\hat{k}_2\hat{k}_3}{-1+\hat{k}_3^2} & -\frac{\hat{k}_3(-1+2\hat{k}_2^2+\hat{k}_3^2)}{-1+\hat{k}_3^2} & -\hat{k}_2 \\ -\frac{\hat{k}_3(-1+2\hat{k}_2^2+\hat{k}_3^2)}{-1+\hat{k}_3^2} & \frac{2\hat{k}_1\hat{k}_2\hat{k}_3}{-1+\hat{k}_3^2} & \hat{k}_1 \\ -\hat{k}_2 & \hat{k}_1 & 0 \end{pmatrix} (|\hat{k}_3| \neq 1). \tag{F.7}$$

Let us denote by $S/2$ the set of the grid points inside the upper half of the spherical shell $S$. More precisely, the set $S/2$ is made up of the gridpoints $\{\boldsymbol{k}_i\}$ in the spherical shell $S$ with $(\boldsymbol{k}_i)_z > 0$, those with $(\boldsymbol{k}_i)_z = 0$ and $(\boldsymbol{k}_i)_y > 0$, and also those with $(\boldsymbol{k}_i)_z = (\boldsymbol{k}_i)_y = 0$ and $(\boldsymbol{k}_i)_z > 0$. Then, the inside of the brace of (F.5) can be rewritten as

$$\begin{aligned}
&\sum_{r,s} \sum_{\boldsymbol{k}_i, \boldsymbol{k}_j \in S/2} [W(|\boldsymbol{k}_i + \boldsymbol{k}_j|) \{h^r(\boldsymbol{k}_i) h^s(\boldsymbol{k}_j) F_{rs}(\eta, \boldsymbol{k}_i + \boldsymbol{k}_j, \boldsymbol{k}_i) + h^r(-\boldsymbol{k}_i) h^s(-\boldsymbol{k}_j) F_{rs}(\eta, -\boldsymbol{k}_i - \boldsymbol{k}_j, -\boldsymbol{k}_i)\} \\
&\quad + W(|\boldsymbol{k}_i - \boldsymbol{k}_j|) \{h^r(-\boldsymbol{k}_i) h^s(\boldsymbol{k}_j) F_{rs}(\eta, -\boldsymbol{k}_i + \boldsymbol{k}_j, -\boldsymbol{k}_i) + h^r(\boldsymbol{k}_i) h^s(-\boldsymbol{k}_j) F_{rs}(\eta, \boldsymbol{k}_i - \boldsymbol{k}_j, \boldsymbol{k}_i)\}] \\
&= \sum_{r,s} \sum_{\boldsymbol{k}_i, \boldsymbol{k}_j \in S/2} [W(|\boldsymbol{k}_i + \boldsymbol{k}_j|) \{h^r(\boldsymbol{k}_i) h^s(\boldsymbol{k}_j) + h^r(\boldsymbol{k}_i)^* h^s(\boldsymbol{k}_j)^*\} F_{rs}(\eta, \boldsymbol{k}_i + \boldsymbol{k}_j, \boldsymbol{k}_i) \\
&\quad + W(|\boldsymbol{k}_i - \boldsymbol{k}_j|) \epsilon_s \{h^r(\boldsymbol{k}_i)^* h^s(\boldsymbol{k}_j) + h^r(\boldsymbol{k}_i) h^s(\boldsymbol{k}_j)^*\} F_{rs}(\eta, \boldsymbol{k}_i - \boldsymbol{k}_j, \boldsymbol{k}_i)] \\
&= \sum_{r,s} \sum_{\boldsymbol{k}_i, \boldsymbol{k}_j \in S/2} [2W(|\boldsymbol{k}_i + \boldsymbol{k}_j|) \{a^r(\boldsymbol{k}_i) a^s(\boldsymbol{k}_j) - b^r(\boldsymbol{k}_i) b^s(\boldsymbol{k}_j)\} F_{rs}(\eta, \boldsymbol{k}_i + \boldsymbol{k}_j, \boldsymbol{k}_i) \\
&\quad + 2\epsilon_s W(|\boldsymbol{k}_i - \boldsymbol{k}_j|) \{a^r(\boldsymbol{k}_i) a^s(\boldsymbol{k}_j) + b^r(\boldsymbol{k}_i) b^s(\boldsymbol{k}_j)\} F_{rs}(\eta, \boldsymbol{k}_i - \boldsymbol{k}_j, \boldsymbol{k}_i)], \qquad \text{(F.8)}
\end{aligned}$$

where we have used $h^r(-\boldsymbol{k}_i) = \epsilon_r h^r(\boldsymbol{k}_i)^*$ ($\epsilon_+ = 1$, $\epsilon_\times = -1$) and $F_{rs}(\eta, -\boldsymbol{k}, -\boldsymbol{k}') = \epsilon_r \epsilon_s F_{rs}(\eta, \boldsymbol{k}, \boldsymbol{k}')$. Note that this has explicitly proven that $\delta_r$ is real, as it should. Let us label the grid points in $S/2$ by $1, 2, \cdots, N$, then introducing

$$\boldsymbol{a}^t = \sigma^{-1}(a^+(\boldsymbol{k}_1), a^+(\boldsymbol{k}_2), \cdots, a^+(\boldsymbol{k}_N), a^\times(\boldsymbol{k}_1), a^\times(\boldsymbol{k}_2), \cdots, a^\times(\boldsymbol{k}_N)), \tag{F.9}$$

$$\boldsymbol{b}^t = \sigma^{-1}(b^+(\boldsymbol{k}_1), b^+(\boldsymbol{k}_2), \cdots, b^+(\boldsymbol{k}_N), b^\times(\boldsymbol{k}_1), b^\times(\boldsymbol{k}_2), \cdots, b^\times(\boldsymbol{k}_N)), \tag{F.10}$$

and using (F.8) we can rewrite (F.5) as

$$\delta_r(\eta, \boldsymbol{x} = \boldsymbol{0}, R) = \frac{1 + c_s^2}{c_s^2 \mathcal{H}} \frac{dk^3}{8\pi\epsilon k_p^3} \left\{ \boldsymbol{a}^t \boldsymbol{M}^a \boldsymbol{a} + \boldsymbol{b}^t \boldsymbol{M}^b \boldsymbol{b} \right\}, \tag{F.11}$$

[†1]When one is interested in the power spectrum, one can use (5.48)-(5.51) due to isotropy, but in simulations the cross term of (F.5) is non-zero and so its contribution has to be taken into account.

where

$$\boldsymbol{M}^a \equiv \begin{pmatrix} \boldsymbol{M}^a_{++} & \boldsymbol{M}^a_{+\times} \\ \boldsymbol{M}^a_{\times+} & \boldsymbol{M}^a_{\times\times} \end{pmatrix}, \quad \boldsymbol{M}^b \equiv \begin{pmatrix} \boldsymbol{M}^b_{++} & \boldsymbol{M}^b_{+\times} \\ \boldsymbol{M}^b_{\times+} & \boldsymbol{M}^b_{\times\times} \end{pmatrix}, \tag{F.12}$$

$$(\boldsymbol{M}^a_{rs})_{ij} = (\boldsymbol{M}^1_{rs})_{ij} + (\boldsymbol{M}^2_{rs})_{ij}, \tag{F.13}$$

$$(\boldsymbol{M}^b_{rs})_{ij} = -(\boldsymbol{M}^1_{rs})_{ij} + (\boldsymbol{M}^2_{rs})_{ij}, \tag{F.14}$$

$$(\boldsymbol{M}^1_{rs})_{ij} = 2W(|\boldsymbol{k}_i + \boldsymbol{k}_j|)F_{rs}(\eta, \boldsymbol{k}_i + \boldsymbol{k}_j, \boldsymbol{k}_i), \tag{F.15}$$

$$(\boldsymbol{M}^2_{rs})_{ij} = 2\epsilon_s W(|\boldsymbol{k}_i - \boldsymbol{k}_j|)F_{rs}(\eta, \boldsymbol{k}_i - \boldsymbol{k}_j, \boldsymbol{k}_i). \tag{F.16}$$

Noting $F_{rs}(\eta, \boldsymbol{k}_i + \boldsymbol{k}_j, \boldsymbol{k}_i) = F_{sr}(\eta, \boldsymbol{k}_j + \boldsymbol{k}_i, \boldsymbol{k}_j)$ and $\epsilon_s F_{rs}(\eta, \boldsymbol{k}_i - \boldsymbol{k}_j, \boldsymbol{k}_i) = \epsilon_r F_{sr}(\eta, \boldsymbol{k}_j - \boldsymbol{k}_i, \boldsymbol{k}_j)$, one can confirm $\boldsymbol{M}^a$ and $\boldsymbol{M}^b$ are symmetric matrices. So by diagonalizing $\boldsymbol{M}^a$ and $\boldsymbol{M}^b$ one can further rewrite (F.11) as

$$\delta_r = a_0 \sum_{i=1}^{2N} a_i x_i^2, \tag{F.17}$$

where $x_1, x_2, \cdots$ are independent Gaussian random variables whose dispersion is unity and

$$0 < a_0, \quad 1 = |a_1| > |a_2| > \cdots > |a_{2N}|. \tag{F.18}$$

The average and dispersion of $\delta_r$ can be written as follows:

$$\langle \delta_r \rangle = a_0 \sum_{i=1}^{2N} a_i, \tag{F.19}$$

$$\sigma^2 = \langle \delta_r^2 \rangle - \langle \delta_r \rangle^2 = a_0^2 \left( \sum_{i=1}^{2N} a_i^2 \langle x_i^4 \rangle + \sum_{i \neq j} a_i a_j - \sum_{i=1}^{2N} a_i^2 - \sum_{i \neq j} a_i a_j \right) = 2a_0^2 \sum_{i=1}^{2N} a_i^2. \tag{F.20}$$

These quantities can also be calculated from eqs.(5.69) and (5.70). For $\eta = (0.7k_p)^{-1}$, $\langle \delta_r \rangle \simeq -0.69$ and $\sigma \simeq 1.03$, and these values have also been obtained in the numerical computations (see (F.22) below), which serves as a crosscheck. We chose $\epsilon = 0.05$ and $dk = \epsilon k_p$. In this case, $N$ turns out to be 2517, but interestingly approximately 98% of $\delta_r$ is determined by only the first 24 terms with most of the rest of the terms being vanishingly small, namely,

$$\frac{\sum_{i=1}^{24} |a_i|}{\sum_{i=1}^{2N} |a_i|} \simeq 0.98. \tag{F.21}$$

Therefore, in analyzing the PDF of $\delta_r$ one can just focus only on a limited number of terms, safely neglecting most of the terms, which greatly simplifies the analysis. We found

$$\begin{aligned} &\langle \delta_r \rangle \simeq -0.69,\ \sigma \simeq 1.0,\ a_0 \simeq 0.30,\ a_{1-5} \simeq -1.0, \\ &a_{6-10} \simeq 0.46,\ a_{11-17} \simeq 0.11,\ a_{18-24} \simeq -0.078. \end{aligned} \tag{F.22}$$

We have also approximately reproduced (F.21) and (F.22) for the cases $\epsilon = 0.1$,$dk = \epsilon k_p$ as well as $\epsilon = 0.1$,$dk = 2\epsilon k_p/3$. This indicates that the above choices of $\epsilon = 0.05$ and $dk = \epsilon k_p$ are sufficiently small to obtain reliable results.

In the following let us discuss the PDF of $\delta_r$ using the coefficients shown in (F.22). First one can resort to a brute-force method of a Monte Carlo simulation to obtain the PDF of $\delta_r$, by simply generating 24 random Gaussian variables with dispersion unity, $x_1, x_2, \cdots, x_{24}$, and summing up the square of them with the coefficients shown in (F.22). We have generated $\{x_i\}$ $10^6$ times to infer the PDF of $\delta_r$, with the result shown in Fig.5.3. In this Appendix $\mathcal{A}$ is set to unity, and so what is shown there is the PDF of $\tilde{\delta_r} \equiv (\delta_r - \langle\delta_r\rangle)/\mathcal{A}^2$.

We adopt Clopper-Pearson interval [250] to obtain 95% confidence interval $p_{\rm L} < p < p_{\rm U}$ of the probability $p$ of $\delta_r$ being realized in some interval $(\delta_r \pm d\delta_r)$, when $\delta_r$ in that range is realized $k$ times in $N$ realizations. First note that the number of an event with probability $p$ realized in $N$ trials follows a Binomial distribution: $P(k;p) = {}_N C_k p^k (1-p)^{N-k}$. Let us introduce $\alpha = 1 - C, C = 0.95$. From the meaning of the confidence interval, the probability of the event begin realized less than $k$ times when $p = p_{\rm U}$ is $\alpha/2$ :

$$\sum_{i=0}^{k} P(i;p_{\rm U}) = I(1-p_{\rm U}, N-k, 1+k) = 1 - I(p_{\rm U}, 1+k, N-k) = \frac{\alpha}{2}, \tag{F.23}$$

where $I(x,a,b)$ is the regularized beta function and the relation $I(x,a,b) = I(1-x,b,a)$ has been used. From this, $p_{\rm U}$ can be expressed by the inverse $I^{-1}$ of the regularized beta function as

$$p_{\rm U} = I^{-1}\left(1 - \frac{\alpha}{2}, 1+k, N-k\right). \tag{F.24}$$

Similarly, the probability of the event being realized more than $k$ times when $p = p_{\rm L}$ is $\alpha/2$:

$$\sum_{i=k}^{N} P(i;p_{\rm L}) = 1 - I(1-p_{\rm L}, N-k+1, k) = I(p_{\rm L}, k, N-k+1) = \frac{\alpha}{2}, \tag{F.25}$$

which leads to

$$p_{\rm L} = I^{-1}\left(\frac{\alpha}{2}, k, N-k+1\right). \tag{F.26}$$

The error bars in Fig.5.3 are obtained from (F.24) and (F.26).

Next let us discuss the approximate form of the PDF. Noting the first ten terms of (F.17) give dominant contributions, let us first consider the PDF of the form $Z = -X + cY$, where $X$ and $Y$ are both random variables following chi-squared distribution with $n$ degrees of freedom and $c$ is a positive constant. The PDF of both X and Y is given by

$$P_1(n;X) = \frac{(1/2)^{n/2}}{\Gamma(n/2)} X^{n/2-1} e^{-X/2}. \tag{F.27}$$

Then the PDF of $Z$ is calculated as follows:

$$\begin{aligned} P_2(n,c;Z) &= N \int_0^\infty dX \int_0^\infty dY \delta(Z + X - cY) P_1(X) P_1(Y) \\ &= \frac{N(1/2)^n}{\Gamma(n/2)^2} e^{-\frac{Z}{2c}} \left(\frac{1}{c}\right)^{\frac{n}{2}-1} \int_{\max\{0,-Z\}}^\infty dX X^{\frac{n}{2}-1} e^{-\frac{X}{2}} (Z+X)^{\frac{n}{2}-1} e^{-\frac{X}{2c}} \\ &= \frac{N}{\sqrt{2\pi 2^n}\Gamma(n/2)} c^{1-n/2} \exp\left(-\frac{1-c}{4c} Z\right) \left(\frac{c|Z|}{1+c}\right)^{(n-1)/2} K_{(n-1)/2}\left(\frac{1+c}{4c}|Z|\right), \end{aligned} \tag{F.28}$$

where $K_m(x)$ is the modified Bessel function of second kind and $N$ is a normalization factor. In considering the PDF of $\delta_r$, one may simply replace the terms $11 \leq i$ in (F.17) by their expectation values $E \equiv 7a_{11} + 7a_{18}$, noting the relative unimportance of these terms, and then the PDF of $\delta_r$ is finally given by

$$P\left(\tilde{\delta}_r\right) = P_2\left(5, a_6; \frac{\tilde{\delta}_r + \langle\delta_r\rangle/\mathcal{A}^2}{a_0} - E\right). \tag{F.29}$$

Interestingly, this approximates the PDF inferred from the Monte Carlo simulation mentioned above overall fairly well, as is shown in Fig.5.3. In more detail, this formula slightly deviates from the simulated points around $\tilde{\delta}_r \sim 0$, presumably because the terms $11 \leq i$, simply replaced by their expectation values to obtain the above approximate formula, are relatively important in this region. On the other hand, the approximate formula is better for $|\tilde{\delta}_r| \gtrsim 2$, which is probably because the probability of these relatively rare events is mostly determined by the first ten terms, with the rest of the terms lying around their expectation values. Since the probability of PBH formation has to be extremely rare, what matters is the integration of the positive tail part of the PDF, for which we use this approximate formula. Then we obtain PBH abundance for given power spectrum of primordial tensor perturbations and place upper bounds on tensor perturbations from the absence of PBHs.

# Bibliography


[1] A. A. Starobinsky, Phys. Lett. **B117**, 175 (1982).

[2] A. H. Guth and S. Y. Pi, Phys. Rev. Lett. **49**, 1110 (1982).

[3] A. D. Linde, Phys. Lett. **B116**, 335 (1982).

[4] S. W. Hawking, Phys. Lett. **B115**, 295 (1982).

[5] G. F. Smoot *et al.*, Astrophys. J. **396**, L1 (1992).

[6] WMAP, D. N. Spergel *et al.*, Astrophys. J. Suppl. **148**, 175 (2003), astro-ph/0302209.

[7] Planck, P. A. R. Ade *et al.*, Astron. Astrophys. **571**, A1 (2014), 1303.5062.

[8] Planck, P. A. R. Ade *et al.*, (2015), 1502.01589.

[9] S. W. Hawking and I. G. Moss, Nucl. Phys. **B224**, 180 (1983).

[10] A. D. Linde, Phys. Lett. **B129**, 177 (1983).

[11] J. M. Bardeen, P. J. Steinhardt, and M. S. Turner, Phys. Rev. **D28**, 679 (1983).

[12] B. Carr, K. Kohri, Y. Sendouda, and J. Yokoyama, Phys.Rev. **D81**, 104019 (2010), 0912.5297.

[13] Y. B. Zel'dovich and I. D. Novikov, sovast **10**, 602 (1967).

[14] S. Hawking, Mon.Not.Roy.Astron.Soc. **152**, 75 (1971).

[15] B. J. Carr and S. Hawking, Mon.Not.Roy.Astron.Soc. **168**, 399 (1974).

[16] E. Bugaev and P. Klimai, Phys.Rev. **D79**, 103511 (2009), 0812.4247.

[17] A. S. Josan, A. M. Green, and K. A. Malik, Phys.Rev. **D79**, 103520 (2009), 0903.3184.

[18] J. Silk, Astrophys. J. **151**, 459 (1968).

[19] H. Satō, Progress of Theoretical Physics **45**, 370 (1971).

[20] R. Sunyaev and Y. Zel'dovich, Astrophys.Space Sci. **7**, 20 (1970).

[21] J. Chluba, J. Hamann, and S. P. Patil, Int. J. Mod. Phys. **D24**, 1530023 (2015), 1505.01834.

[22] M. Ricotti and A. Gould, Astrophys. J. **707**, 979 (2009), 0908.0735.

[23] T. Bringmann, P. Scott, and Y. Akrami, Phys.Rev. **D85**, 125027 (2012), 1110.2484.

[24] SDSS, X. Fan *et al.*, Astron.J. **125**, 1649 (2003), astro-ph/0301135.

[25] C. J. Willott, R. J. McLure, and M. J. Jarvis, Astrophys.J. **587**, L15 (2003), astro-ph/0303062.

[26] J. D. Kurk *et al.*, Astrophys.J. **669**, 32 (2007), 0707.1662.

[27] L. Jiang *et al.*, Astron.J. **134**, 1150 (2007), 0707.1663.

[28] C. J. Willott *et al.*, Astron.J. **134**, 2435 (2007), 0706.0914.

[29] L.-H. Jiang *et al.*, Astron.J. **135**, 1057 (2008), 0708.2578.

[30] L. Jiang *et al.*, Astron.J. **138**, 305 (2009), 0905.4126.

[31] C. J. Willott *et al.*, Astron.J. **139**, 906 (2010), 0912.0281.

[32] C. J. Willott *et al.*, Astron.J. **140**, 546 (2010), 1006.1342.

[33] G. De Rosa *et al.*, Astrophys.J. **739**, 56 (2011), 1106.5501.

[34] D. J. Mortlock *et al.*, Nature **474**, 616 (2011), 1106.6088.

[35] G. De Rosa *et al.*, Astrophys.J. **790**, 145 (2014), 1311.3260.

[36] E. Banados *et al.*, Astron.J. **148**, 14 (2014), 1405.3986.

[37] X.-B. W. et al., Nature **518**, 512 (2015).

[38] M. Kawasaki, A. Kusenko, and T. T. Yanagida, Phys.Lett. **B711**, 1 (2012), 1202.3848.

[39] K. Kohri, T. Nakama, and T. Suyama, Phys.Rev. **D90**, 083514 (2014), 1405.5999.

[40] T. Nakama, T. Suyama, and J. Yokoyama, in prep. (2016).

[41] G. Steigman and K. M. Nollett, (2014), 1401.5488.

[42] Planck Collaboration, P. Ade *et al.*, Astron.Astrophys. **571**, A16 (2014), 1303.5076.

[43] T. Nakama, T. Suyama, and J. Yokoyama, Phys.Rev.Lett. **113**, 061302 (2014), 1403.5407.

[44] T. Nakama and T. Suyama, Phys. Rev. **D92**, 121304 (2015), 1506.05228.

[45] T. Nakama and T. Suyama, in prep. (2016).

[46] A. A. Starobinsky, JETP Lett. **30**, 682 (1979).

[47] A. A. Starobinsky, Phys.Lett. **B91**, 99 (1980).

[48] K. Sato, mnras **195**, 467 (1981).

[49] A. H. Guth, Phys. Rev. D **23**, 347 (1981).

[50] J. Martin, Lect. Notes Phys. **738**, 193 (2008), 0704.3540.

[51] D. H. Lyth, K. A. Malik, and M. Sasaki, JCAP **0505**, 004 (2005), astro-ph/0411220.

[52] D. Lyth, K. A. Malik, M. Sasaki, and I. Zaballa, JCAP **0601**, 011 (2006), astro-ph/0510647.

[53] K. Jedamzik, M. Lemoine, and J. Martin, JCAP **1009**, 034 (2010), 1002.3039.

[54] E. R. Harrison, Phys. Rev. D **1**, 2726 (1970).

[55] P. J. E. Peebles and J. T. Yu, Astrophys. J. **162**, 815 (1970).

[56] Ya. B. Zel'dovich, Mon. Not. Roy. Astron. Soc. **160**, 1P (1972).

[57] P. Ivanov, P. Naselsky, and I. Novikov, Phys. Rev. D **50**, 7173 (1994).

[58] J. Yokoyama, Phys.Rev. **D58**, 083510 (1998), astro-ph/9802357.

[59] R. Saito, J. Yokoyama, and R. Nagata, JCAP **0806**, 024 (2008), 0804.3470.

[60] S. R. Coleman and E. J. Weinberg, Phys. Rev. **D7**, 1888 (1973).

[61] J. Garcia-Bellido, A. D. Linde, and D. Wands, Phys.Rev. **D54**, 6040 (1996), astro-ph/9605094.

[62] J. Yokoyama, Astron.Astrophys. **318**, 673 (1997), astro-ph/9509027.

[63] M. Kawasaki, N. Sugiyama, and T. Yanagida, Phys.Rev. **D57**, 6050 (1998), hep-ph/9710259.

[64] M. Kawasaki and T. Yanagida, Phys.Rev. **D59**, 043512 (1999), hep-ph/9807544.

[65] J. Yokoyama, Phys.Rept. **307**, 133 (1998).

[66] A. Taruya, Phys.Rev. **D59**, 103505 (1999), hep-ph/9812342.

[67] T. Kanazawa, M. Kawasaki, and T. Yanagida, Phys.Lett. **B482**, 174 (2000), hep-ph/0002236.

[68] T. Kawaguchi, M. Kawasaki, T. Takayama, M. Yamaguchi, and J. Yokoyama, Mon.Not.Roy.Astron.Soc. **388**, 1426 (2008), 0711.3886.

[69] L. Alabidi and K. Kohri, Phys.Rev. **D80**, 063511 (2009), 0906.1398.

[70] P. H. Frampton, M. Kawasaki, F. Takahashi, and T. T. Yanagida, JCAP **1004**, 023 (2010), 1001.2308.

[71] T. Suyama and J. Yokoyama, Phys.Rev. **D84**, 083511 (2011), 1106.5983.

[72] K. Kohri, C.-M. Lin, and T. Matsuda, Phys.Rev. **D87**, 103527 (2013), 1211.2371.

[73] M. Kawasaki, N. Kitajima, and T. T. Yanagida, Phys.Rev. **D87**, 063519 (2013), 1207.2550.

[74] T. Suyama, Y.-P. Wu, and J. Yokoyama, Phys.Rev. **D90**, 043514 (2014), 1406.0249.

[75] A. M. Green, Fundam. Theor. Phys. **178**, 129 (2015), 1403.1198.

[76] B. J. Carr, (2005), astro-ph/0511743.

[77] B. J. Carr, Astrophys.J. **201**, 1 (1975).

[78] J. M. Bardeen, J. Bond, N. Kaiser, and A. Szalay, Astrophys.J. **304**, 15 (1986).

[79] R. J. Adler, Chichester ; New York : Wiley,c1981. (1981).

[80] T. Harada, C.-M. Yoo, and K. Kohri, Phys.Rev. **D88**, 084051 (2013), 1309.4201.

[81] A. G. Polnarev and I. Musco, Class.Quant.Grav. **24**, 1405 (2007), gr-qc/0605122.

[82] T. Nakama, T. Harada, A. Polnarev, and J. Yokoyama, JCAP **1401**, 037 (2014), 1310.3007.

[83] T. Nakama, JCAP **1410**, 040 (2014), 1408.0955.

[84] D. K. Nadezhin, I. D. Novikov, and A. G. Polnarev, Sov. Astron. **22**, 129 (1978).

[85] C. W. Misner and D. H. Sharp, Phys. Rev. **136**, B571 (1964).

[86] J. C. Niemeyer and K. Jedamzik, Phys.Rev. **D59**, 124013 (1999), astro-ph/9901292.

[87] W. C. Hernandez and C. W. Misner, Astrophys. J. **143**, 452 (1966).

[88] T. W. Baumgarte, S. L. Shapiro, and S. A. Teukolsky, Astrophys. J. **443**, 717 (1995).

[89] J. C. Niemeyer and K. Jedamzik, Phys. Rev. Lett. **80**, 5481 (1998), astro-ph/9709072.

[90] J. Yokoyama, Phys. Rev. **D58**, 107502 (1998), gr-qc/9804041.

[91] I. Musco and J. C. Miller, Class. Quant. Grav. **30**, 145009 (2013), 1201.2379.

[92] M. Shibata and M. Sasaki, Phys.Rev. **D60**, 084002 (1999), gr-qc/9905064.

[93] I. Hawke and J. Stewart, Class.Quant.Grav. **19**, 3687 (2002).

[94] I. Musco, J. C. Miller, and L. Rezzolla, Class. Quant. Grav. **22**, 1405 (2005), gr-qc/0412063.

[95] I. Musco, J. C. Miller, and A. G. Polnarev, Class. Quant. Grav. **26**, 235001 (2009), 0811.1452.

[96] A. Polnarev, T. Nakama, and J. Yokoyama, JCAP **1209**, 027 (2012), 1204.6601.

[97] T. Harada, C.-M. Yoo, T. Nakama, and Y. Koga, Phys.Rev. **D91**, 084057 (2015), 1503.03934.

[98] S. Young, C. T. Byrnes, and M. Sasaki, JCAP **1407**, 045 (2014), 1405.7023.

[99] W. H. Press and P. Schechter, Astrophys. J. **187**, 425 (1974).

[100] MACHO, EROS, C. Alcock *et al.*, Astrophys. J. **499**, L9 (1998), astro-ph/9803082.

[101] EROS-2, P. Tisserand *et al.*, Astron. Astrophys. **469**, 387 (2007), astro-ph/0607207.

[102] S. Hawking, Nature **248**, 30 (1974).

[103] K. Griest, A. M. Cieplak, and M. J. Lehner, (2013), 1307.5798.

[104] F. Capela, M. Pshirkov, and P. Tinyakov, Phys. Rev. **D87**, 123524 (2013), 1301.4984.

[105] P. Pani and A. Loeb, JCAP **1406**, 026 (2014), 1401.3025.

[106] F. Capela, M. Pshirkov, and P. Tinyakov, Phys. Rev. **D90**, 083507 (2014), 1403.7098.

[107] J. H. MacGibbon, Nature **329**, 308 (1987).

[108] H. V. Peiris and R. Easther, JCAP **0807**, 024 (2008), 0805.2154.

[109] H. Assadullahi and D. Wands, Phys. Rev. **D81**, 023527 (2010), 0907.4073.

[110] R. Saito and J. Yokoyama, Phys.Rev.Lett. **102**, 161101 (2009), 0812.4339, [**107**, 069901(E) (2011).].

[111] R. Saito and J. Yokoyama, Prog.Theor.Phys. **123**, 867 (2010), 0912.5317, [**126**, 351(E) (2011).].

[112] R. Khatri and R. A. Sunyaev, JCAP **1206**, 038 (2012), 1203.2601.

[113] E. Pajer and M. Zaldarriaga, Phys. Rev. Lett. **109**, 021302 (2012), 1201.5375.

[114] D. Fixsen *et al.*, Astrophys.J. **473**, 576 (1996), astro-ph/9605054.

[115] A. Kogut *et al.*, JCAP **1107**, 025 (2011), 1105.2044.

[116] PRISM, P. Andre *et al.*, (2013), 1306.2259.

[117] Ya. B. Zel'dovich and R. A. Sunyaev, Astrophys. Space Sci. **4**, 301 (1969).

[118] J. Chluba, Mon. Not. Roy. Astron. Soc. **436**, 2232 (2013), 1304.6121.

[119] M. Anthonisen, R. Brandenberger, A. Lague, I. A. Morrison, and D. Xia, (2015), 1509.07998.

[120] D. Jeong, J. Pradler, J. Chluba, and M. Kamionkowski, Phys.Rev.Lett. **113**, 061301 (2014), 1403.3697.

[121] J. Chluba, A. L. Erickcek, and I. Ben-Dayan, Astrophys.J. **758**, 76 (2012), 1203.2681.

[122] J. M. Cornell, S. Profumo, and W. Shepherd, Phys. Rev. **D88**, 015027 (2013), 1305.4676.

[123] E. Bertschinger, Astrophys. J. Suppl. **58**, 39 (1985).

[124] S. Profumo, (2013), 1301.0952.

[125] Y. Yang, G. Yang, and H. Zong, Phys. Rev. **D87**, 103525 (2013), 1305.4213.

[126] F. Li, A. L. Erickcek, and N. M. Law, Phys. Rev. **D86**, 043519 (2012), 1202.1284.

[127] L. Lindegren *et al.*, Astron. Astrophys. **538**, A78 (2012), 1112.4139.

[128] H. A. Clark, G. F. Lewis, and P. Scott, (2015), 1509.02938.

[129] H. A. Clark, G. F. Lewis, and P. Scott, (2015), 1509.02941.

[130] I. Shlosman, J.-H. Choi, M. C. Begelman, and K. Nagamine, (2015), 1508.05098.

[131] S. F. Bramberger, R. H. Brandenberger, P. Jreidini, and J. Quintin, JCAP **1506**, 007 (2015), 1503.02317.

[132] Z. Sherkatghanad and R. H. Brandenberger, (2015), 1508.00968.

[133] S. Hirano, N. Zhu, N. Yoshida, D. Spergel, and H. W. Yorke, Astrophys. J. **814**, 18 (2015), 1504.05186.

[134] V. Dokuchaev, Y. Eroshenko, and S. Rubin, (2007), 0709.0070.

[135] M. Volonteri, Astron.Astrophys.Rev. **18**, 279 (2010), 1003.4404.

[136] A. Sesana, Adv.Astron. **2012**, 805402 (2012), 1110.6445.

[137] E. Treister and C. M. Urry, Adv.Astron. **2012**, 516193 (2012), 1112.0320.

[138] Z. Haiman, (2012), 1203.6075.

[139] Y.B.Zel'dovich and I.D.Novikov, Sov.Astron. **10**, 602 (1967).

[140] B. J. Carr, J. Gilbert, and J. E. Lidsey, Phys.Rev. **D50**, 4853 (1994), astro-ph/9405027.

[141] Planck, P. Ade *et al.*, (2015), 1502.01589.

[142] Planck, P. Ade *et al.*, (2015), 1502.01592.

[143] B. J. Carr and J. E. Lidsey, Phys.Rev. **D48**, 543 (1993).

[144] A. A. Starobinsky, JETP Lett. **42**, 152 (1985).

[145] D. Salopek and J. Bond, Phys.Rev. **D42**, 3936 (1990).

[146] M. Sasaki and E. D. Stewart, Prog.Theor.Phys. **95**, 71 (1996), astro-ph/9507001.

[147] M. Sasaki and T. Tanaka, Prog.Theor.Phys. **99**, 763 (1998), gr-qc/9801017.

[148] D. Wands, K. A. Malik, D. H. Lyth, and A. R. Liddle, Phys.Rev. **D62**, 043527 (2000), astro-ph/0003278.

[149] A. A. Starobinsky, Lect.Notes Phys. **246**, 107 (1986).

[150] D. Lyth and A. Liddle, Cambridge University Press (2009).

[151] Planck, P. Ade *et al.*, (2015), 1502.02114.

[152] N. Takeda and Y. Watanabe, Phys.Rev. **D90**, 023519 (2014), 1405.3830.

[153] WMAP Collaboration, G. Hinshaw *et al.*, (2012), 1212.5226.

[154] Planck Collaboration, P. Ade *et al.*, (2013), 1303.5082.

[155] J. Garcia-Bellido, A. Linde, and D. Wands, Phys. Rev. D **54**, 6040 (1996).

[156] H. M. Hodges and G. R. Blumenthal, Phys. Rev. D **42**, 3329 (1990).

[157] J. Yokoyama, Astron. Astrophys. **318:673** (1997).

[158] J. Yokoyama, Phys. Rev. D **58**, 083510 (1998).

[159] J. Yokoyama, Phys. Rep. **307**, 133 (1998).

[160] M. Kawasaki and T. Yanagida, Phys. Rev. D **59**, 043512 (1999).

[161] J. Yokoyama, Prog. Theor. Phys. Suppl. **136**, 338 (1999).

[162] R. Saito, J. Yokoyama, and R. Nagata, J. Cosmol. Astropart. Phys. **2008**, 024 (2008).

[163] A. Taruya, Phys. Rev. D **59**, 103505 (1999).

[164] B. A. Bassett and S. Tsujikawa, Phys. Rev. D **63**, 123503 (2001).

[165] A. M. Green and K. A. Malik, Phys. Rev. D **64**, 021301 (2001).

[166] M. Kawasaki, T. Takayama, M. Yamaguchi, and J. Yokoyama, Mod. Phys. Lett. **A22**, 1911 (2007).

[167] A. S. Josan and A. M. Green, Phys.Rev. **D82**, 083527 (2010), 1006.4970.

[168] P. Scott, T. Bringmann, and Y. Akrami, J.Phys.Conf.Ser. **375**, 032012 (2012), 1205.1432.

[169] J. Barrow and P. Coles, Mon. Not. Roy. Astron. Soc. **248**, 52 (1991).

[170] J. Chluba and R. Sunyaev, (2011), 1109.6552.

[171] J. Chluba, R. Khatri, and R. A. Sunyaev, (2012), 1202.0057.

[172] J. B. Dent, D. A. Easson, and H. Tashiro, Phys.Rev. **D86**, 023514 (2012), 1202.6066.

[173] R. Khatri and R. A. Sunyaev, JCAP **1209**, 016 (2012), 1207.6654.

[174] R. A. Sunyaev and R. Khatri, Int.J.Mod.Phys. **D22**, 1330014 (2013), 1302.6553.

[175] R. Khatri and R. A. Sunyaev, JCAP **1306**, 026 (2013), 1303.7212.

[176] J. Chluba and D. Grin, Mon.Not.Roy.Astron.Soc. **434**, 1619 (2013), 1304.4596.

[177] J. Chluba and D. Jeong, Mon. Not. Roy. Astron. Soc. **438**, 2065 (2014), 1306.5751.

[178] H. Sato, Prog. Theor. Phys. **45**, 370 (1970).

[179] C. Burigana, L. Danese, and G. de Zotti, Astron. Astrophys. **246**, 49 (1991).

[180] W. Hu and J. Silk, Phys.Rev. **D48**, 485 (1993).

[181] V. Simha and G. Steigman, JCAP **0806**, 016 (2008), 0803.3465.

[182] J. Barrow, Nature **267**, 117 (1977).

[183] S. Dodelson, Academic Press (2003).

[184] C.-P. Ma and E. Bertschinger, Astrophys. J. **455**, 7 (1995), astro-ph/9506072.

[185] K. Jedamzik, V. Katalinic, and A. V. Olinto, Phys.Rev. **D57**, 3264 (1998), astro-ph/9606080.

[186] V. Mukhanov, Cambridge University Press (2005).

[187] M. Pettini and R. Cooke, Mon. Not. Roy. Astron. Soc. **425**, 2477 (2012), 1205.3785.

[188] Y. I. Izotov, G. Stasinska, and N. G. Guseva, Astron. Astrophys. **558**, A57 (2013), 1308.2100.

[189] T. Matsubara, University of Tokyo Press (2010).

[190] C. T. Byrnes, E. J. Copeland, and A. M. Green, Phys.Rev. **D86**, 043512 (2012), 1206.4188.

[191] S. Young and C. T. Byrnes, JCAP **1308**, 052 (2013), 1307.4995.

[192] K. Sato, Mon.Not.Roy.Astron.Soc. **195**, 467 (1981).

[193] A. H. Guth, Phys.Rev. **D23**, 347 (1981).

[194] BICEP2 Collaboration, P. Ade *et al.*, Phys.Rev.Lett. **112**, 241101 (2014), 1403.3985.

[195] B. Allen, (1996), gr-qc/9604033.

[196] T. L. Smith, E. Pierpaoli, and M. Kamionkowski, Phys.Rev.Lett. **97**, 021301 (2006), astro-ph/0603144.

[197] Y. Kikuta, K. Kohri, and E. So, (2014), 1405.4166.

[198] A. Ota, T. Takahashi, H. Tashiro, and M. Yamaguchi, (2014), 1406.0451.

[199] J. Chluba, L. Dai, D. Grin, M. Amin, and M. Kamionkowski, Mon.Not.Roy.Astron.Soc. **446**, 2871 (2015), 1407.3653.

[200] G. Mangano *et al.*, Nucl. Phys. **B729**, 221 (2005), hep-ph/0506164.

[201] K. Ichiki, M. Yahiro, T. Kajino, M. Orito, and G. Mathews, Phys.Rev. **D66**, 043521 (2002), astro-ph/0203272.

[202] P. S. Apostolopoulos and N. Tetradis, Phys.Lett. **B633**, 409 (2006), hep-th/0509182.

[203] R. Maartens and K. Koyama, Living Rev.Rel. **13**, 5 (2010), 1004.3962.

[204] Y. B. Zel'dovich and I. D. Novikov, Sov. Astron. **10**, 602 (1967).

[205] S. Matarrese, O. Pantano, and D. Saez, Phys.Rev.Lett. **72**, 320 (1994), astro-ph/9310036.

[206] S. Matarrese, S. Mollerach, and M. Bruni, Phys.Rev. **D58**, 043504 (1998), astro-ph/9707278.

[207] C. Carbone and S. Matarrese, Phys.Rev. **D71**, 043508 (2005), astro-ph/0407611.

[208] K. N. Ananda, C. Clarkson, and D. Wands, Phys.Rev. **D75**, 123518 (2007), gr-qc/0612013.

[209] D. Baumann, P. J. Steinhardt, K. Takahashi, and K. Ichiki, Phys.Rev. **D76**, 084019 (2007), hep-th/0703290.

[210] L. Alabidi, K. Kohri, M. Sasaki, and Y. Sendouda, JCAP **1209**, 017 (2012), 1203.4663.

[211] E. Bugaev and P. Klimai, Phys.Rev. **D83**, 083521 (2011), 1012.4697.

[212] E. Bugaev and P. Klimai, Phys.Rev. **D81**, 023517 (2010), 0908.0664.

[213] D. R. Brill, Annals Phys. **7**, 466 (1959).

[214] K. Eppley, Phys.Rev. **D16**, 1609 (1977).

[215] S. M. Miyama, Prog.Theor.Phys. **65**, 894 (1981).

[216] M. Shibata, K.-i. Nakao, T. Nakamura, and K.-i. Maeda, Phys.Rev. **D50**, 708 (1994).

[217] M. Shibata and T. Nakamura, Phys.Rev. **D52**, 5428 (1995).

[218] P. Anninos, J. Masso, E. Seidel, W.-m. Suen, and M. Tobias, Phys.Rev. **D54**, 6544 (1996), gr-qc/9601026.

[219] M. Shibata, Phys.Rev. **D55**, 7529 (1997).

[220] M. Alcubierre *et al.*, Phys.Rev. **D62**, 044034 (2000), gr-qc/0003071.

[221] H. P. Pfeiffer, L. E. Kidder, M. A. Scheel, and D. Shoemaker, Phys.Rev. **D71**, 024020 (2005), gr-qc/0410016.

[222] L. A. Boyle, P. J. Steinhardt, and N. Turok, Phys. Rev. **D69**, 127302 (2004), hep-th/0307170.

[223] M. Baldi, F. Finelli, and S. Matarrese, Phys. Rev. **D72**, 083504 (2005), astro-ph/0505552.

[224] E. J. Copeland, D. J. Mulryne, N. J. Nunes, and M. Shaeri, Phys. Rev. **D79**, 023508 (2009), 0810.0104.

[225] T. Kobayashi, M. Yamaguchi, and J. Yokoyama, Prog. Theor. Phys. **126**, 511 (2011), 1105.5723.

[226] T. Biswas, T. Koivisto, and A. Mazumdar, JHEP **08**, 116 (2014), 1403.7163.

[227] A. Ashoorioon, K. Dimopoulos, M. M. Sheikh-Jabbari, and G. Shiu, Phys. Lett. **B737**, 98 (2014), 1403.6099.

[228] D. Cannone, G. Tasinato, and D. Wands, JCAP **1501**, 029 (2015), 1409.6568.

[229] L. Graef and R. Brandenberger, JCAP **1510**, 009 (2015), 1506.00896.

[230] Y. Wang and W. Xue, JCAP **1410**, 075 (2014), 1403.5817.

[231] S. Weinberg, Oxford University Press (2008).

[232] M. Maggiore, Oxford University Press (2008).

[233] M. Maggiore, Phys.Rept. **331**, 283 (2000), gr-qc/9909001.

[234] S. Kuroyanagi, T. Takahashi, and S. Yokoyama, (2014), 1407.4785.

[235] I. Sendra and T. L. Smith, Phys. Rev. **D85**, 123002 (2012), 1203.4232.

[236] LIGO Scientific, VIRGO, J. Aasi *et al.*, Phys.Rev.Lett. **113**, 231101 (2014), 1406.4556.

[237] A. Nishizawa and N. Seto, Phys.Rev. **D91**, 122001 (2015), 1503.00354.

[238] A. D. Dolgov and D. Ejlli, Phys. Rev. **D84**, 024028 (2011), 1105.2303.

[239] T. Nakama and T. Suyama, in prep. (2016).

[240] M. M. May and R. H. White, Academic Press, New York and London (1967).

[241] I. Musco and J. C. Miller, arXiv:1201.2379 [gr-qc] (2012).

[242] W. C. Hernandez, Jr. and C. W. Misner, Astrophys. J. **143**, 452 (1966).

[243] J. C. Miller and S. Motta, Class. Quant. Grav. **6**, 185 (1989).

[244] J. C. Niemeyer and K. Jedamzik, Phys. Rev. D **59**, 124013 (1999).

[245] I. Musco, J. C. Miller, and L. Rezzolla, Class. Quant. Grav. **22**, 1405 (2005).

[246] D. K. Nadezhin, I. D. Novikov, and A. G. Polnarev, NASA STI/Recon Technical Report N **80**, 10983 (1979).

[247] T. Nakama, T. Harada, A. Polnarev, and J. Yokoyama, JCAP **2014**, 037 (2014).

[248] C. Pitrou, X. Roy, and O. Umeh, Class.Quant.Grav. **30**, 165002 (2013), 1302.6174.

[249] D. Baumann, (2011), 0907.5424.

[250] C. Clopper and E. S. Pearson, Biometrika **26**, 404 (1934).